GOLD MINERALISATION IN THE KIRK RANGE AREA, SOUTHERN MALAWI

by

Joshua Joseph Chisambi

Dissertation presented for the degree of Doctor
of Earth Sciences in the Faculty of
Science at Stellenbosch University

Supervisor: Dr Bjorn von der Heyden

Department of Earth Sciences, Stellenbosch University

December 2020

Declaration

By submitting this thesis/dissertation electronically, I declare that the entirety of the work contained therein is my own, original work, that I am the sole author thereof (save to the extent explicitly otherwise stated), that reproduction and publication thereof by Stellenbosch University will not infringe any third party rights and that I have not previously in its entirety or in part submitted it for obtaining any qualification.

Signed:
Joshua Joseph Chisambi
20 July 2020.

Abstract

This study aims at understanding the characteristics and controls of gold mineralisation in the Kirk Range area, southern Malawi. Malawi's mineral inventory is not known, particularly this is attributed to a general low resolution in the knowledge of Malawi's geology, coupled with historical under-exploration for this important economic commodity. Regional scale interpretations are afforded by in-depth investigation of airborne geophysical data, which are then supported by ground geological mapping and by microscopic observations using optical and electron microscopy, and X-ray computed tomography (XCT). We further used petrography and mineral chemistry, zircon geochronology, PT estimates, fluid inclusion microthermometry and stable isotope studies. Gold is mainly hosted in biotite schists and is structurally controlled by the NE-SW trending ductile shear zones where it occurs as flakes ranging in size between 0.24 and 4 mm. The gold mineralisation is associated with smoky quartz carbonate veins. It is associated with a pyrite-chalcopyrite-sphalerite generation of sulphide, and to a lesser extent, with sericitised biotite schist wall rock. U–Pb ages for gold bearing-schists and proximal gneisses document two distinct events: an Irumide-age period of metamorphism and a Pan African period of metamorphism. The gneisses experienced both the Irumide and Pan African events while the biotite schist experienced only the Pan African deformation. Irumide metamorphism occurred at around 1066-991 Ma and Pan African metamorphism overprinted the Irumide and occurred at around 700-485 Ma. Based on a loose PT constraint, the rocks experienced peak metamorphic conditions of around 500-600ºC and 10-15 kbars. Mineralization occurred in the early stages of Pan African event before peak metamorphism likely under greenschist facies conditions. Later deformation to amphibolite facies conditions of metamorphism during the prolonged Pan African event led to the transposition of the original mineralization. Gold mineralisation occurred at temperature of

around 222-300°C and pressure of around 2.0–2.8 kbar. Minerals of economic interest were likely deposited by fluid immiscibility and fluid rock interaction.

Acknowledgements

I would like to express my gratitude to my supervisor Dr Bjorn von der Heyden for his guidance support and supervision. I have learnt a lot from you in the past 3 years, you have moulded me to be a scientist. When times were tough you still had faith in me that I can do this. You were available anytime I needed to see you. I really appreciate.

I also thank the University of Malawi, the polytechnic for awarding me a scholarship through the Skills Development Project to undertake this work. Thanks also go to the Geological Survey of Malawi for providing me with some of the samples that were used in this work.

I dedicate this thesis to my late dad who died when I was in grade 3 and never lived to see the man I have become and to my surviving mum (Lucy Chisambi) who tirelessly made sure that I go to school.

Above all I thank GOD for giving me wisdom and intelligence to undertake this work. I owe it to the creator.

Table of contents

List of Figures

Chapter 1: introduction

Chapter 2: Gold exploration in two- and three dimensions: improved and correlative insights from microscopy and X-ray computed tomography

Chapter 3: Primary gold mineralisation in the Lisungwe Valley area, Kirk Range, southern Malawi

Chapter 4: Geochemistry, geochronology and metamorphic history of the Manondo - Choma gold prospect, Kirk Range Southern Malawi

Chapter 5: Conclusions and genetic model for gold mineralisation at Manondo-Choma area

List of Tables

Chapter 2: Gold exploration in two- and three dimensions: improved and correlative insights from microscopy and X-ray computed tomography

Chapter 3: Primary gold mineralisation in the Lisungwe Valley area, Kirk Range, southern Malawi

Chapter 4: Geochemistry, geochronology and metamorphic history of the Manondo - Choma gold prospect, Kirk Range Southern Malawi: Implications for ore genesis

CHAPTER 1

General introduction to the study

1. Introduction

Gold is one of the most coveted metals in the world as it is a source of wealth and economic growth and development. Gold mining is the engine of economic growth and it provides valuable foreign exchange. Recently, there has been growing demand for this important commodity in the developing world (Kumah, 2006). Many countries in Africa are endowed with enormous mineral resources, and for hundreds of years, they have relied hugely on mining for economic growth. Proof within the literature (Amponsah-tawiah, 2011) shows that organized gold mining in Africa dates way back to the Middle Ages; certain countries, such as Republic of Ghana and Mali, were parts of important trans-Saharan gold trading routes. Today, Africa accounts for some 30% of global gold mine output (Kumah, 2006).

Although mineral resources have formed the engine of economic growth and development for most developing countries in Africa, this has not been the case with Malawi, a country in the sub-Saharan Africa. Malawi's economy has for a long time heavily relied on rain fed agriculture (Ministry of Mining, 2013). Agricultural accounts for one third of the GDP and nearly 80 percent of employment. However due to droughts, agriculture has not helped Malawi's economic growth and development. Consequently, the economy has not been doing well. The government is now looking for alternative ways to improve and diversify the ailing economy. According to the Malawi Growth and Development Strategy (2006-2011) (MGDS) the government of Malawi has identified mining as one of the sectors that could potentially generate economic growth for the country. Currently the mining sector in Malawi accounts for only about 1% of the country's GDP (Ministry of Mining, 2013).

Nevertheless, Malawi has abundant mineral resources such as gold, if exploited can sustainably contribute to the growth of the economy. Gold mining in Malawi has a long history that dates back to the 1900s (Carter, 1973). Gold was first discovered in 1908 by the Geological Survey of Malawi and as of today several other gold occurrences have been reported in different places within the country. Although gold occurrences have been known in several places within the country, no major large-scale gold exploitation has been undertaken. Gold is currently being mined by only small-scale artisanal miners along the rivers (Figure 1). These are primarily placer deposits that have not been fully explored. Some of the major gold occurrences include the following:

Lisungwe Valley-Kirk Range

This is one of the well-known gold occurrences in Malawi and has aroused most interest. The Lisungwe Valley (Kirk Range) is located about 55 km west of Blantyre. Gold has been known to occur in the Lisungwe valley since 1908 and was first reported by Andrew and Bailey (reported in Bloomfield & Garson, 1965). Most of the alluvial gold mined by artisanal miners come from this valley. The river valley has great potential for gold mining with Little Chisumbwiti and Chitimbe streams, tributaries to the main Lisungwe river being the most mineralised (Figure 2). This is the study area for this work.

Nathenje Area

The Nathenje area is located in the central Malawi, towards the south of Lilongwe. Gold in this area was first discovered in the 1960s during a geochemical mapping of the country (Thatcher & Walter, 1968). Further studies of the area reveal that most of the gold are found in sulphide rich bands of graphitic garnet-biotite-clinopyroxene gneiss (Thatcher & Walter, 1968).

Unga River (Mangochi- Makanjila area).

Gold was first discovered in the Unga river in the Mangochi- Makanjila area in 1936 during a reconnaissance survey by the geological Survey of Malawi (King & Dawson, 1976). Detailed exploration followed in 1937 and it was discovered that the gold bearing veins were thin and sporadically spread for any meaningful commercial gold mining. No further studies have been done since then, however the locals are still mining placer gold in this river.

Dwangwa River

The Dwangwa River in the northern part of Malawi is another important source of alluvial gold in Malawi. Gold in this area was first reported in 1908 by Andrew and Bailey (Cater & Bennet, 1973). Further exploration was carried out by the British South African Company in 1938 but not many detailed studies were done afterwards. It was reported that gold in this area is derived from quartz stringers in the adjacent country gneisses

Figure 1 *Artisanal miners panning gold in the rivers*

Despite these known gold occurrences, no modern studies have been undertaken regarding understanding the controls of mineralisation. There is a need to further investigate these gold occurences if Malawi is to stimulate its economic growth and development. Neighbouring countries Mozambique, Zambia and Tanzania have abundant mineral resources, yet comparatively little is known about Malawi, despite these countries occuring in the same tectonic zone as Malawi and sharing similarities in their geological histories. This study therefore aims to understand the characteristics and controls of gold mineralisation in the greater Kirk Range area by using the Little Chisumbwiti river valley as a case study. The highest placer gold grades in the Kirk Range are found in the Little Chisumbwiti River valley, a tributary of the main Lisungwe River where gold has previously been mined from the Breeze's and Phalula Mines (British Geological Survey, 2009). Understanding the processes of ore mineralisation could provide clues and directions for future exploration. This is important given Malawi's political viewpoints in which the local government is convinced that if the country's mineral resources are fully explored and exploited, the contribution of mining to the GDP will increase to at least 20 percent within the next 10 years (Ministry of Mining, 2013).

2. Aims and Objectives

The main aim of this study is to develop a genetic model for the gold mineralisation at Manondo-Choma area in the Kirk Range, southern Malawi.

2.1 Objectives

The primary objectives of this research are as follows

- To conduct detailed geological mapping in the area in order to understand structures and host rocks controlling primary gold mineralisation.
- To characterize the ore paragenesis.

- To understand the chemistry and the origin of the fluids responsible for gold mineralisation.
- To understand the timing and physical chemical conditions that led to gold deposition in the area.
- To contextualise the gold mineralisation within the regional geochronological and metamorphic history of the study area.

3. Location and Physiography

The area described in this study covers about 25 km^2 and lies between latitudes 15°00′ and 15°20′ S and longitude 34°45′ E and the western border of Malawi with Mozambique (34°35′ E). It is situated in the southern and central regions of Malawi about 40km north-west of Blantyre (Figure. 3). The area consists of the Kirk Plateau, the Border uplands, the Neno step, foothills zone, and the Shire Valley plain. Altitude in the area varies from about 370 m to over 1800 m. The ground gradually descends to the east from the border in a series of faults. The principal river is the Lisungwe River which starts from near Tsangano Hill and flows eastwards up to the edge of the foothills zone. It is joined by the Likudzi Stream and lower down by the Mwendangombe Stream, and at last it drains into the Shire River.

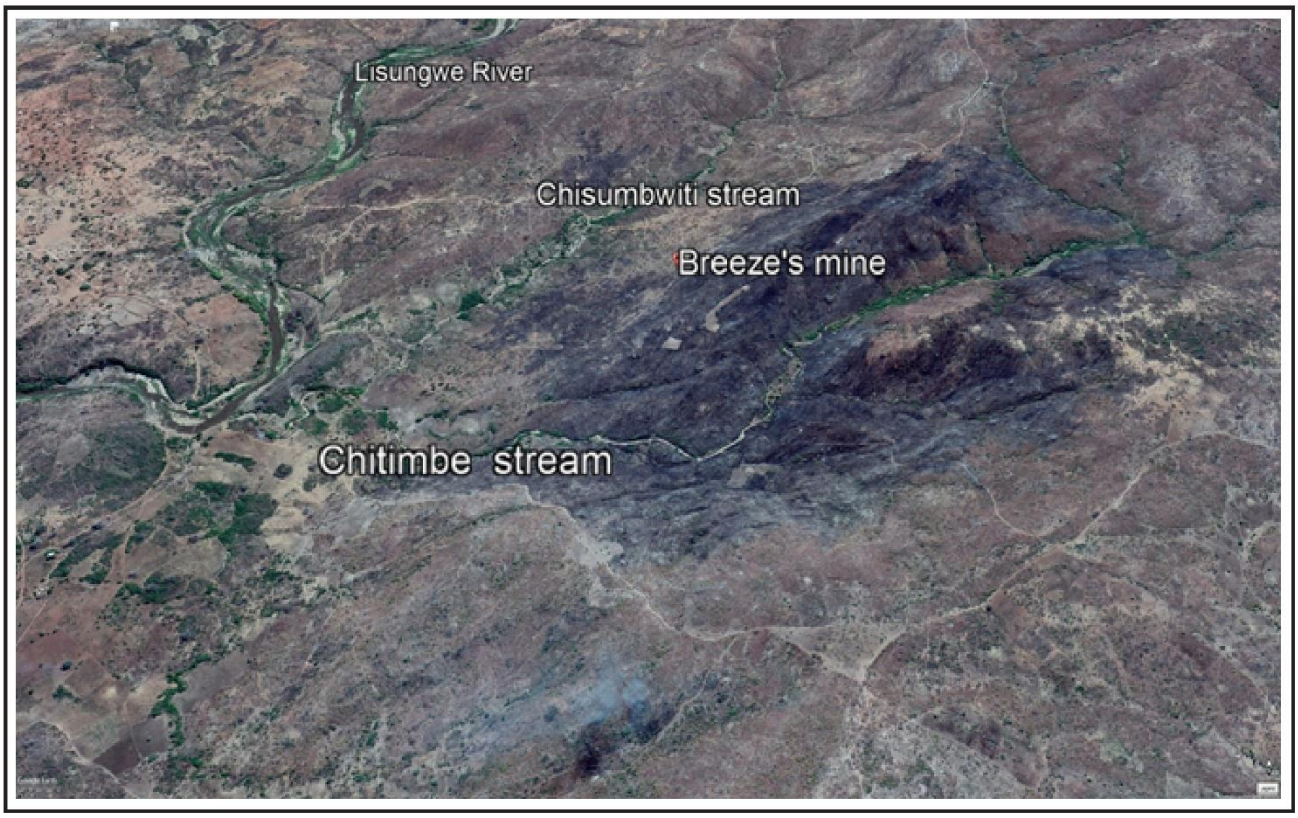

Figure 2. *Chisumbwiti river valley (area studied) all these streams have high gold mineralisation and artisanal mining takes place in them*

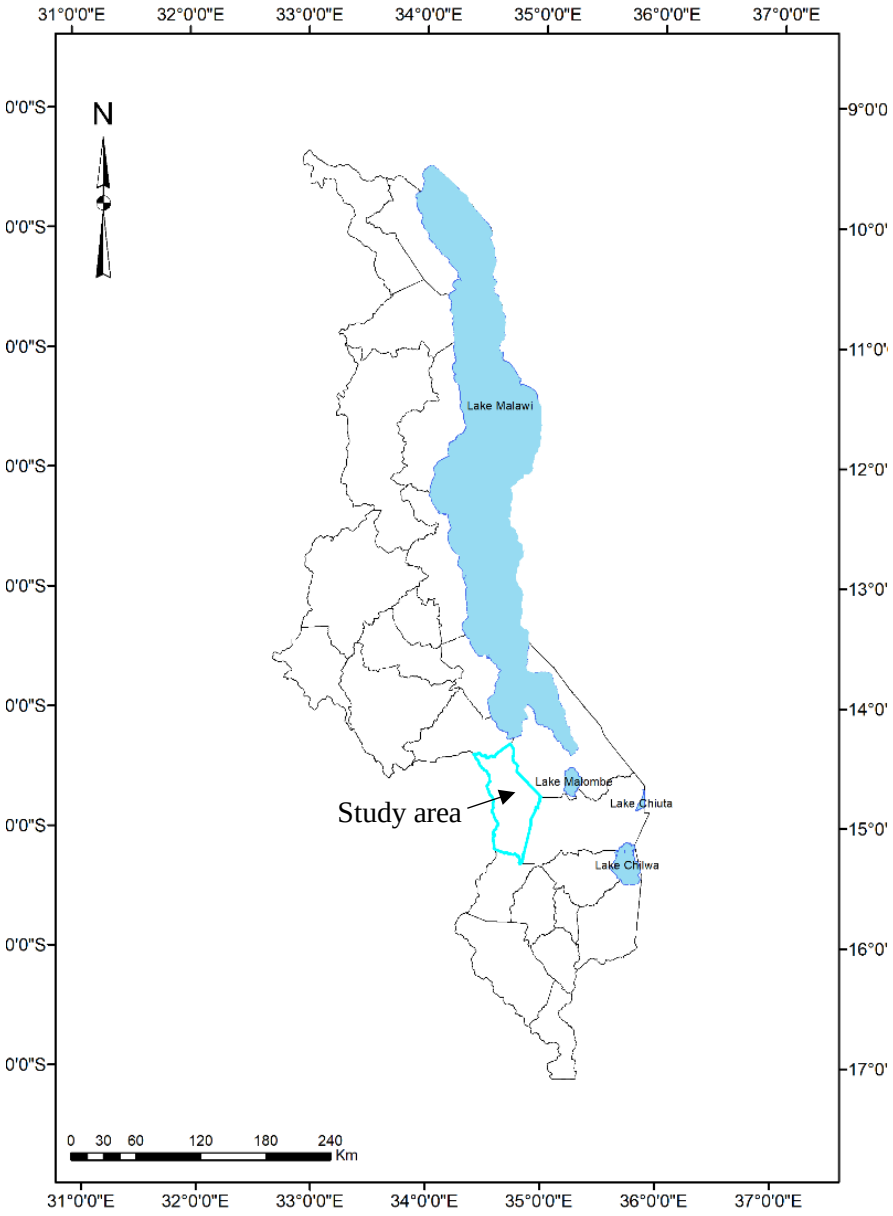

***Figure 3**. Location map of the study area and artisanal miners panning gold in the rivers around the study area*

4. Regional Geology

The geology of the Kirk Range, and indeed the whole of Malawi, has not been well constrained, with the existing geological map dating back to 1965 (Bloomfield. & Garson., 1965). The geology of Malawi is underlain by Precambrian to lower Paleozoic high-grade metamorphic para- and orthogneisses and schists commonly referred to Malawi basement complex rocks

(Cater & Bennet, 1973). These rocks have undergone high-grade metamorphism and polyphase deformation (Achille & Andreoli, 2001; Cater & Bennet, 1973, Dill, 2007; Dulanya, 2017; Dulanya, Morales-simfors, & Sivertun, 2010; Hori & Tomita, 1997) and a prolonged structural and metamorphic history. They are associated with three major orogenic events (Ubendian, Irumide, and Mozambiquean), (Ring et al., 2002; Sommer et al., 2003).

The Ubendian belt is characterized by NW-SE trending structures and was first described by McConnell (1950). It was formed during the Palaeoproterozoic Ubendian Orogeny between 2200-1800 Ma (De Waele et al., 2003). The rocks of the Ubendian belt are characterized by sequences of medium- to high grade metamorphic supracrustal gneisses and schist that were intruded by various plutonic igneous rocks (Lenoir et al., 1994). The rocks experienced peak metamorphic conditions of 750-850ºC at 18 kbar and record high pressure granulite facies conditions (Ring et al., 1997). The Ubendian belt rocks were structurally overprinted during the Mesoproterozoic (Irumide) and Neoproterozoic (East African/Pan-African) orogenies. These later events extensively altered the internal architecture of the belt and partly obscured the Palaeoproterozoic history.

Mesoproterozoic Irumide orogeny is a north-east trending orogenic belt. It is marked by rapid increase in metamorphic grade from greenschist facies conditions to granulite facies conditions. The Irumide Belt was first described by Ackermann (1950) and Ackermann and Forster (1960). The main structural trend of the Irumide belt is northeast and is related to extensive crustal shortening during the main stage of the Irumide orogeny. This orogenic belt is subdivided by crustal-scale shear zones into the Irumide s.s, the Southern Irumide, the Unango Subprovince, and the Nampula Subprovince with a general trend of NE-SW (De Waele et al., 2006; Boyd et al. 2009; Macey et al. 2010). The regional metamorphic grade in the Irumide Belt is of medium pressure/medium temperature Barrovian type, which is more consistent with an accretionary setting then a continent–continent collision. P–T–t models

suggest a clockwise metamorphic P–T–t path (Mapani, 1999) that is linked to the major shortening event recorded by northwest-verging thrusts. The timing of peak metamorphism in the Irumide belt constrained by SHRIMP U–Pb zircon dates between 1021 ± 16 and 1018 ± 5 Ma (De Waele et al., 2003).

The Pan African Orogeny occurred roughly at 800-500 Ma (De Waele et al., 2003), forming the Mozambique Belt. (Ring et al., 1997; Lenoir et al., 1994). The Pan African Orogeny (De Waele et al., 2003) was the last major orogenic event that shaped the overall geology of Malawi and resulted in significant overprinting of older orogenic features from the Ubendian- and Irumide orogenies (Ring et al., 1997). The Pan African Orogeny created N-S trending structures and reactivated older pre-existing structures. Peak conditions for the orogenic event were suggested to be 750-800ºC at roughly 12-13 kbar and subsequent amphibolite facies retrogression occurred at 550-700ºC at 5-8 kbar (Sommer et al., 2003). Regional geological map is shown in Figure 4.

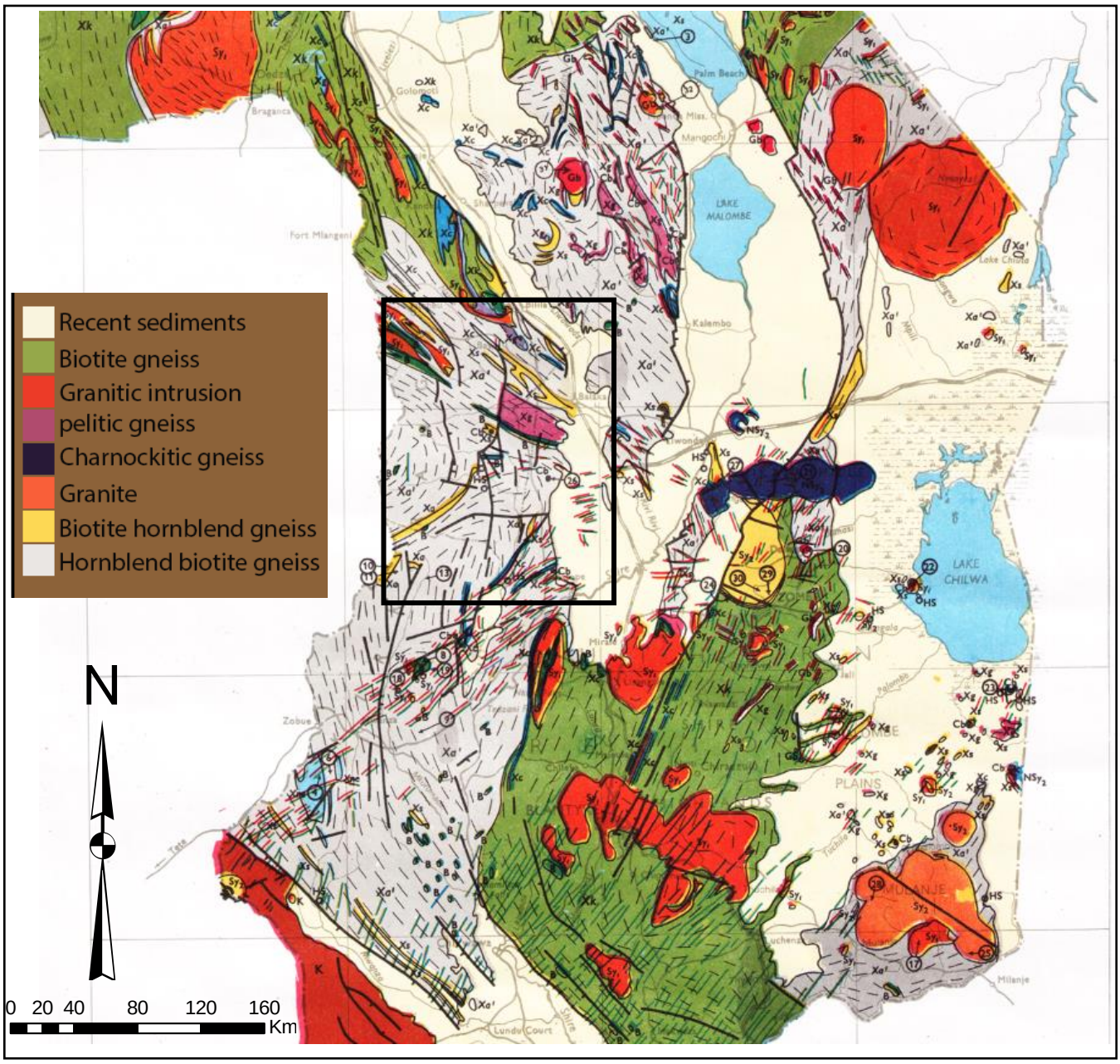

Figure 4 *Regional geological map of the study area (rectangle) (Source Geological Survey of Malawi)*

5. Characteristics of Orogenic Gold Setting

Orogenic gold deposits formed during compressional to transpressional deformation processes at convergent plate margins and are a major source of world gold production. These deposits are found in regionally metamorphosed belts throughout the world and are located adjacent to crustal-scale shear zones (Figure 5) (Goldfarb, Groves, & Gardoll, 2001; Pitcairn & Damon, 2006). Mineralisation is strongly structurally controlled and are generally sited in second or third order structures. Big crustal scale structures transport gold-bearing hydrothermal fluids which are then channelled to the network of smaller structural zones that host mineralisation (Goldfarb et al., 2001; Groves, 1993; Groves, Goldfarb, Robert, & Hart, 2003). The fluids associated with these gold deposits are of low-salinity, near-neutral, $H_2O–CO_2 \pm CH_4$ fluids which transport gold as a reduced sulphur complexes (Goldfarb et al., 2001). The source of the fluids is still controversial, but most studies indicate that the fluids are derived from devolatilization reactions from a deep source. It is estimated that approximately 1000 km^3 of hydrothermal fluid could be released from devolatilization of 1000 km^2 rock column less than 10 km thick during rapid burial in a convergent orogeny (Beaudoin, Therrien, & Savard, 2006). Gold mineralisation is mostly located in second- or third-order structures close to the crustal-scale shear zones, in brittle, brittle–ductile, and ductile deformational environments (Eilu & Grooves, 2001).,Slip along crustal scale shear zones cause dilation near jogs that draw fluids and deposits gold in an interconnected network of shear zones (Goldfarb et al., 2001).. Host rocks are commonly regionally metamorphosed in greenschist through lower amphibolite facies.

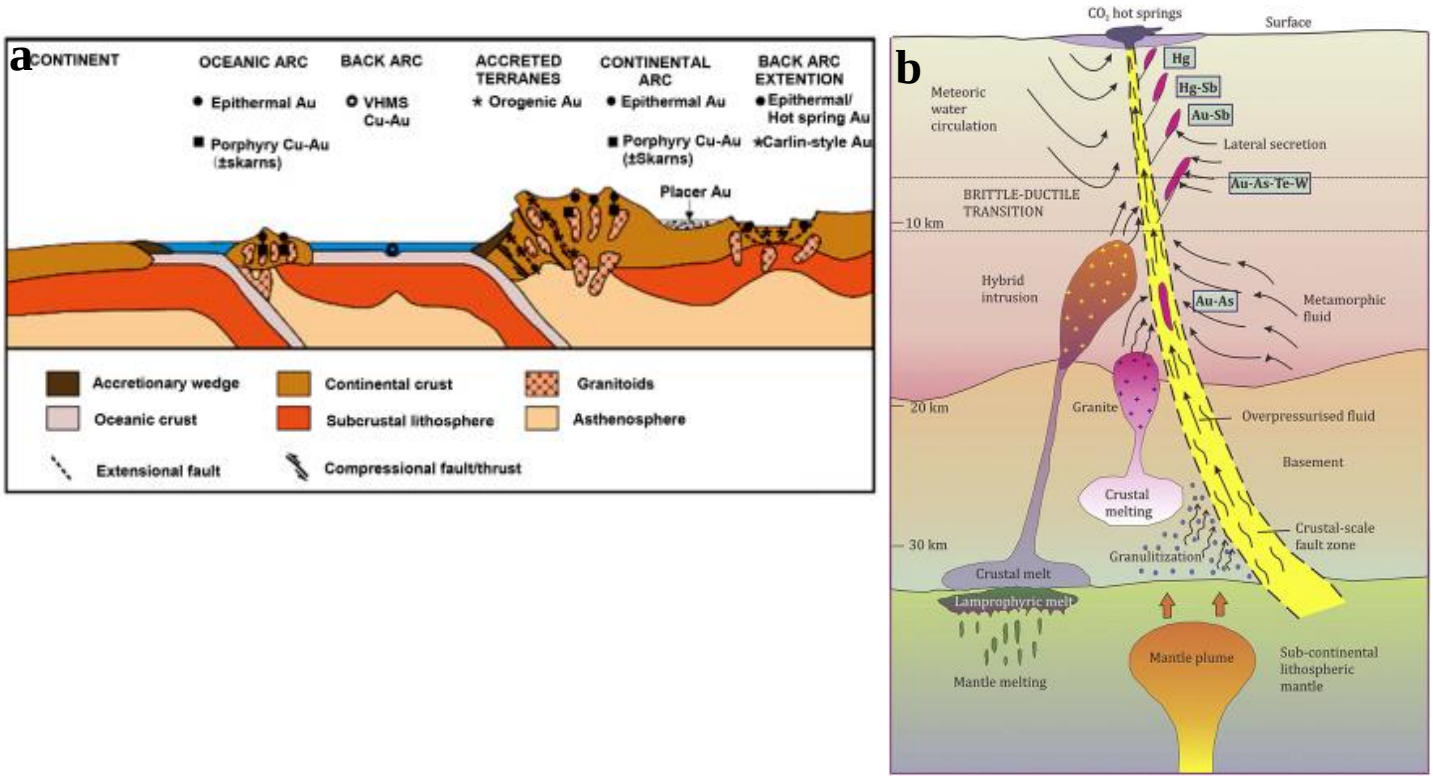

Figure 5: *Schematic diagram showing the tectonic setting and nature of orogenic gold deposits. (a) Plate tectonic environments of formation of orogenic gold deposits. (b) Depth profile of orogenic gold deposit (Source Groves et al. 1998).*

6. Major Themes and Thesis Structure

This thesis consists of five chapters written in the format of stand-alone scientific papers. Each section deals with a separate aspect pertaining to the study of gold mineralisation in the study area.

Chapter 2 is written as methods paper stressing the applicability of correlative use of XCT and microscopy in mapping and evaluating gold ore forming systems. In this chapter we apply a correlative XCT-microscopy approach towards understanding the nature of gold mineralisation at the Manondo-Choma gold prospect area in the Kirk Range. X-ray Computed Tomography (XCT) plus correlative microscopies have not yet been widely utilized in evaluating ore forming systems. The combination of 2-D and 3-D analysis provides a better understanding on

the nature of gold mineralisation. The chapter has been published in the research journal *Minerals* in 2020 (Chisambi et al., 2020).

Application of the technique outlined in Chapter 2 is portrayed in Chapter 3, which focuses on mapping and understanding structural controls of gold mineralisation in the area. This chapter focusses on developing a regional, local and microscopic understanding of the characteristics of gold occurrences in the mineralized Little Chisumbwiti river valley. Particular attention was devoted to mapping and understanding structural controls of gold mineralisation in the area. Structural mapping indicates that the area has been affected by at least two periods of deformation (D1-D2). The D1 deformation event is characterized by NW–SE directed crustal shortening (tentatively associated with the Southern Irumide orogeny) which produced NE–SW structures. Gold mineralisation in the Little Chisumbwiti river valley is hosted in NE-SW trending shear structures in quartz--sulphide vein sets, where it occurs as flakes ranging in size between 0.24 and 4 mm. These results have been published in the *South African Journal of Geology* in 2019 (Chisambi and von der Heyden, 2019).

Chapter 4 builds on work that was done in chapter 3, with more focus on geochemistry of hydrothermal fluids responsible for gold mineralisation in the area. It presents a detailed study of fluid inclusions and stable isotopes from the Manondo – Choma gold prospect in order to understand the origin and evolution of these hydrothermal fluids that were responsible for gold mineralisation and help to improve our understanding of the processes that resulted in the formation of the Manondo-Choma gold prospect. Fluid inclusions and microthermometry studies were carefully carried out on mineralized quartz veins from the area. This chapter also presents the metamorphic history of the area in order to contextualise the mineralisation in the region's geological history. A manuscript documenting the results from this investigation is in preparation for submission to the *African Journal of Earth Sciences* in 2020.

The concluding chapter (Chapter 5) presents a brief synopsis of the thesis, providing a summary of the findings outlined in the preceding chapters and a genetic model for gold mineralisation. Furthermore, it highlights possible avenues for future research and outstanding gaps in knowledge regarding gold mineralisation in Malawi. At the end of each chapter, a complete list of the relevant references is included, formatted to the style prescribed by the journal to which the chapter has been or will be submitted.

References

Achille, M., & Andreoli, G. (2001). Petrochemistry, Tectonic Evolution And Metasomatic Mineralisations Of Mozambique Belt Granulites From S Malawi And Tete (Mozambique). *Precambrian Research*, *25*(1984).

Ackermann, E.H., (1950). Ein neuer Faltengürtel in Nordrhodesien und seine tektonische Stellung im Afrikanischen Grundgebirge. *Geologische Rundschau*, 38, 24-39.

Ackermann, E.H., and Forster, A., (1960). Grundzuge der Stratigraphie und Struktur des Irumide Orogen. In: *21st International Geological Congress*.

Amponsah-tawiah, K. (2011). The Mining Industry in Ghana : A Blessing or a Curse. *International Journal of Business and Social Sciences*, *2*(12), 62–69.

Beaudoin, G., Therrien, R., & Savard, C. (2006). 3D numerical modelling of fluid flow in the Val-d ' Or orogenic gold district : major crustal shear zones drain fluids from overpressured vein fields. *Mineralium Deposita*, 82–98. https://doi.org/10.1007/s00126-005-0043-5

Boyd, R., Nordgulen, Ø., Thomas, R.J., Bingen, B., Bjerkgård, T., Grenne, T. and Jamal, D., (2010). The Geology And Geochemistry Of The East African Orogen In Northeastern Mozambique. *Geological Society Of South Africa*, 113, 87-129. Http://Doi.Org/10.2113/Gssajg.113.1.87

Bloomfield.K, & Garson.M.S. (1965). The Geology of the Kirk Range-Lisungwe Valley Area. Ministry of Natural Resources. Geological Survey Department. Bulletin No.17. *The Government Printer, Zomba. Malawi*.

Bloomfield, K., & Garson, M. S. (1965). The Geology Of The Kirk Range-Lisungwe Valley

Area. *Government print,* Zomba, Malawi.

Carter, G. S. (1973). The Geology And Mineral Resources Of Malawi. *Government print,* Zomba, Malawi.

De Waele, B., Wingate, M., Fitzsimons, I. & Mapani, B., (2003). Untying the Kibaran knot: A reassessment of Mesoproterozoic correlations in southern Africa based on SHRIMP U-Pb data from the Irumide belt). *Geological Society of America,* 31, 509{512.

De Waele, B., Kampunzu, A. and Tembo, F., (2006). The Mesoproterozoic Irumide belt of Zambia. *Journal of African EarthSciences* ,46,36-70. http://doi.org/10.1016/j.jafrearsci.2006.01.018

Dill, H. G. (2007). A review of mineral resources in Malawi : With special reference to aluminium variation in mineral deposits. *Journal of African Earth Sciences*, *47*, 153–173. https://doi.org/10.1016/j.jafrearsci.2006.12.006

Dulanya, Z. (2017). A review of the geomorphotectonic evolution of the south Malawi rift. *Journal of African Earth Sciences*.

Dulanya, Z., Morales-simfors, N., & Sivertun, Å. (2010). Journal of African Earth Sciences Comparative study of the silica and cation geothermometry of the Malawi hot springs : Potential alternative energy source. *Journal of African Earth Sciences*, *57*(4), 321–327. https://doi.org/10.1016/j.jafrearsci.2009.11.001

Eilu, P., & Grooves, D. (2001). Primary alteration and geochemical dispersion haloes of Archaean orogenic gold deposits in the Yilgarn Craton : the pre-weathering scenario. *Geochemistry: Exploration,Environment, Analysis*, *1*(1(3)), 183–200.

Goldfarb, R. J., Groves, D. I., & Gardoll, S. (2001). Orogenic gold and geologic time : a global

synthesis. *Ore Geology Reviews*.

Grooves, D. (1993). The crustal continuum model for late-Archaean lode-gold deposits of the Yilgarn Block, Western Australia. *Mineralium Deposita*, *374*, 366–374.

Grooves, D., Goldfarb, R., Robert, F., & Hart, C. (2003). Gold Deposits in Metamorphic Belts : Overview of Current Understanding , Outstanding Problems , Future Research , and Exploration Significance. *Economic Geology*, *98*, 1–29.

Hori, T., & Tomita, K. (1997). Regional Geochemical Reconnaissance of Kirk Range-Lisungwe, Malawi. *Kagoshima University*.

King, A., & Dawson, A. (1976). The geology of the Mangochi-Makanjila area. *Government Printer, Zomba*.

Kumah, A. (2006). Sustainability and gold mining in the developing world. *Journal of Cleaner Production*, *14*. https://doi.org/10.1016/j.jclepro.2004.08.007.

Lenoir, J. L. et al., (1995). The Palaeoproterozoic Ubendian shear belt in Tanzania: geochronology and structure. *Journal of African Earth Sciences,* 19, 169-184.

Macey, P.H., Miller, J.A., Rowe, C.D., Grantham, G.H., Siegfried, P., Armstrong, R.A. and Bacalau, J., (2010). Geology of the Monapo Klippe , northeast Mozambique and its significance for assembly of central Gondwana. *Precambrian Research,* 233, 259-281. http://doi.org/10.1016/j.precamres. 2013.03.012.

McConnell, R.B., (1950). Outline of the geology of Ufipa and Ubende. *Bulletin of Geological Survey of Tanganyika. East African Standard.* 62pp.

Ministry of Mining. (2013). *Mines And Minerals Policy Of Malawi*.

Pitcairn, I., & Damon, T. (2006). Sources of Metals and Fluids in Orogenic Gold Deposits :

Insights from the Otago and Alpine Schists , New Zealand. *Society of Economic Geologists*, *101*, 1525–1546.

Ring, U., Kroner, A., Buchwaldt, R., Toulkeridis, T. & Layer, P., (2002). Shear-zone patterns and eclogite-facies metamorphism in the Mozambique belt of northern Malawi, east-central Africa: implications for the assembly of Gondwana. *Precambrian Research*, 116, 19{56.

Ring, U., Kroner, A. & Toulkeridis, T., (1997). Palaeoproterozoic granulite-facies metamorphism and granitoid intrusions in the Ubendian-Usagaran Orogen of northern Malawi, east-central Africa. *Precambrian Research*, 85, 27{51.

Sommer, H., Kroner, A., Hauzenberger, C., Muhongo, S. & Windgate, M., (2003). Metamorphic petrology and zircon geochronology of high-grade rocks from the central Mozambique Belt of Tanzania: crustal recycling of Archean and Palaeoproterozoic material during the Pan-African orogeny. *Journal of Metamorphic Geology*, 21, 915{934.

Thatcher, E. C., & Walter, M. J. (1968). *The Geology of the South Lilongweplain and Dzalanyama Range, Bulletin No. 23. Government Printer, Zomba, Malawi.*

CHAPTER 2

Gold exploration in two and three dimensions: improved and correlative insights from microscopy and X-ray computed tomography

A presentation of the published research paper

This manuscript has been published in the research journal *minerals*, after review by four anonymous reviewers. I am the first author and Dr Bjorn von der Heyden is the co-author. The manuscript highlights the advantages of combining two-dimensional chemical and mineralogical data with three-dimensional structural/positional data, using a complex orogenic gold mineralisation system in the Kirk Range (southern Malawi) as a case study. It details the utility of this study approach both for quantifying gold concentrations in core samples (which is often nuggety and may thus be misrepresented by quarter- or half-core assays), and for understanding the spatial distribution of gold and associated structures and micro-structures in 3D space. Importantly, it posits that the latter point holds vast potential for exploration practitioners especially if the correlative approach can be automated and if the resultant spatially constrained microstructural can be fed directly into commercially available geological modelling software. Given that modern exploration efforts are targeting increasingly complex and low-grade ore deposits, we believe that the extra layers of information provided by using correlative 2D and 3D microscopies offer an exciting new tool to enhance and optimize minerals exploration workflows.

Data compilation, through XCT scanning and ore microscopy was performed by me through the help of Central Analytical Facility CT scan staff (Stephan Le Roux and Muofhe

Tshibalanganda) herein included as co-authors. I was also responsible for the written work and the creation of all the diagrams. I conceptualized the idea of correlative use of X-ray computed Tomography and microscopy in mapping gold mineralisation and Dr Bjorn von der Heyden contributed towards the writing in the capacity of a second author.

Article

Gold Exploration in Two and Three Dimensions: Improved and Correlative Insights from Microscopy and X-Ray Computed Tomography

Joshua Chisambi [1,2,*], Bjorn von der Heyden [1], Muofhe Tshibalanganda [3] and Stephan Le Roux [3]

1. Department of Earth Sciences, Stellenbosch University, Private Bag X1, Matieland, Stellenbosch 7602, South Africa; bvon@sun.ac.za
2. Department of Mining Engineering, University of Malawi, the Polytechnic, Private Bag 303, Chichiri, Blantyre 3, Malawi
3. Central Analytical Facility, Stellenbosch University, Private Bag X1, Matieland, Stellenbosch 7602, South Africa; muofhe@sun.ac.za (M.T.); lerouxsg@sun.ac.za (S.L.R.)

* Correspondence: jjchisambi@gmail.com or jchisambi@poly.ac.mw

Received: 3 April 2020; Accepted: 12 May 2020; Published: 25 May 2020

Abstract:

In this contribution, we highlight a correlative approach in which three-dimensional structural/positional data are combined with two dimensional chemical and mineralogical data to understand a complex orogenic gold mineralization system; we use the Kirk Range (southern Malawi) as a case study. Three dimensional structures and semi-quantitative mineral distributions were evaluated using X-ray Computed Tomography (XCT) and this was augmented with textural, mineralogical and chemical imaging using Scanning Electron Microscopy (SEM) and optical microscopy as well as fire assay. Our results detail the utility of the correlative approach both for quantifying gold concentrations in core samples (which is often nuggety and may thus be misrepresented by quarter- or half-core assays), and for understanding the spatial distribution of gold and associated structures and microstructures in 3D space. This approach overlays complementary datasets from 2D and 3D analytical protocols, thereby allowing a better and more comprehensive understanding on the distribution and structures controlling gold mineralization. Combining 3D XCT analyses with conventional 2D microscopies derive the full value out of a given exploration drilling program and it provides an excellent tool for understanding gold mineralization. Understanding the spatial distribution of gold and associated structures and microstructures in 3D space holds vast potential for exploration practitioners, especially if the correlative approach can be automated and if the resultant spatially-constrained microstructural information can be fed directly into commercially available geological modelling software. The extra layers of information provided by using correlative 2D and 3D microscopies offer an exciting new tool to enhance and optimize mineral exploration workflows, given that modern exploration efforts are targeting increasingly complex and low-grade ore deposits.

Keywords: gold exploration; X-ray computed tomography; correlative science

1. Introduction

Gold exploration continues to attract a vast proportion of the global minerals exploration budget (e.g., ~50% of the $10.1 billion exploration budget for 2018 [1]). Much of this gold has been won from ‘orogenic’ classes of gold mineralization [2,3], which generally form in

metamorphic terranes associated with accretionary or collisional orogenies [4]. These geological settings are typically characterized by a high level of structural complexity, in which gold mineralization may be multi-stage or may be overprinted or remobilized during progressive stages during the evolving orogenic cycle [5]. This high degree of geological complexity complicates modern day gold exploration efforts, which are already compromised by the fact that most easily-mined near-surface gold deposits have already been discovered and/or mined out [6,7].

To address this challenge, geoscientists are continually looking to develop and apply robust exploration techniques which can better constrain the spatial distribution of ore minerals within the host rocks and within mineralized structures [8]. Once ore bodies have been identified and drilled, the conventional approach towards understanding mineral textures and parageneses has predominantly been limited to two-dimensional analytical protocols (e.g., optical microscopy [9], scanning electron microscopy (including automated technologies, Quantitative Evaluation of Minerals by Scanning Electron Microscopy (QEMSCAN) technologies), electron microprobe micro-analysis [10], (synchrotron) X-ray Fluorescence Mapping [11], Laser induced breakdown spectroscopy, Raman spectroscopy and to a lesser extent, Laser Ablation Inductively Coupled Plasma Mass Spectroscopy (LA-ICP-MS) mapping [12]). Although these protocols provide detailed 2D textural, chemical and mineralogical information, they are inherently limited in that they fail to fully consider the mineralogical, textural, and structural heterogeneity extending into the third dimension. The advent and proliferation of bench-scale X-ray computed tomography (XCT) analytical protocols enables 3D information of ore samples to be able now to be routinely obtained [13,14]. This non-destructive XCT technology measures X-ray attenuation as an X-ray beam passes through a rotating ore sample (i.e., 360° measurement), where the X-ray attenuation varies as a function of mineral density and atomic

number [15,16]. Because of their relatively high density, ore minerals (e.g., sulphides and gold) can easily be identified and distinguished from a matrix of less dense silicate (rock-forming) minerals [14]. Importantly for orogenic gold studies, gold is characterized by an exceedingly high density (19.3 $g.cm^{-3}$) and thus, a high X-ray attenuation coefficient, which ensures that even very small grains can be distinguished and measured using XCT [17].

A growing body of scientific literature has realized the advantages of XCT based techniques for understanding the 3D internal structure of ore samples [17–23]. For example, [24] demonstrated the use of XCT as an analytical tool to quantify tungsten ore mineral content and ore grade. Similarly,[21] used lab-based XCT to characterize 3D textural settings of orogenic gold where they used combination of 3D visualization and mineral quantification methods to decipher spatial characteristics of ore-forming processes. Likewise, the authors in [25] investigated the distribution of sulphides using X-ray computed tomography to better understand how the base metal sulphides and gold formed in the Bushveld Igneous Complex, South Africa and Stillwater Complex, Montana, USA. Inasmuch as these examples serve to highlight the unique affordances of XCT in providing 3D textural (and to an extent mineralogical) data, the true power of XCT can only be fully realized if it is combined with the detailed chemical information supplied by more conventional 2D technologies (e.g., optical- and electron-microscopies, microprobes, etc.). In this contribution, we highlight a correlative approach, in which 3D XCT data are combined with 2D mineralogical and chemical data to understand a complex orogenic gold mineralization system in the Kirk Range (southern Malawi). Of special importance to orogenic gold deposits in which the siting of mineralization often has a strong structural control, we demonstrate the power of contextualizing observed 2D structural features in a 3D volume. We posit that export of this geometrically (XCT) contextualized structural data directly into geological databases and models will meaningfully

contribute to the depth of data obtained during orogenic gold exploration programs, and foresee that correlative XCT-microscopic approaches will in future become a more prominent component of the gold exploration workflow.

2. Materials and Methods

Four drill core samples (extracted from borehole JJ-01: 100.20 to 100.50 m, 120.5 to 120.10 m depth, coordinates 15.31721° S, 34.83958° E and borehole JJ-02: 60.5 to 60.20 m, 80.1 to 80.8 m depth, coordinates 15.30666° S, 34.84301° E) were selected from the gold bearing mineralized quartz veins from the Manondo-Choma gold prospect for XCT and correlative microscopy analyses. Three dimensional structures and semi-quantitative mineral distributions were evaluated using XCT and this was augmented with textural, mineralogical and chemical imaging using Scanning Electron Microscopy (SEM) and optical microscopy. Gold grades within the core samples were quantified using standard fire assay protocols [26].

2.1. High Resolution X-Ray Computed Tomography (XCT)

In order to understand the distribution of gold mineralization in mineralized drill core samples, four segments of the core sample (45 mm diameter; lengths respectively: 15, 3, 5 and 7 cm) were scanned using the Electric Phoenix VTomeX L240 micro X-ray Computed Tomography scanner system at the Central Analytical Facility (CAF), Stellenbosch University (South Africa), manufactured by General Electric Sensing and Inspection Technologies/Phoenix X-ray (Wunstorff, Germany). The XCT facility is described in more detail in [27]. To optimize scanning of gold-sulphide ores, the scanning parameters were set to 100 kV and 100 µA and the X-ray beam was filtered using a 0.5 mm Cu filter. Images were acquired using a dwell time of 500 ms. Each scan took about 4 h and the resulting model had a voxel size of 35 µm. Furthermore, a small subsample (dimensions 5mm in diameter) cut from the original core

sample JJ01 was also scanned at a high resolution using phoenix Nanotom S nanoCT scanner, manufactured by Phoenix X-ray (Wunstorff, Germany), the scanning parameters were set to 150 kV and 200 µA and the X-ray beam was filtered using a 0.5 mm Cu filter. Images were acquired using a dwell time of 500 ms. The resulting model had a voxel size of 10 µm.

These models were reconstructed using a filtered back projection algorithm built into the GE Datos 2.1 reconstruction package [27]. Subsequent data evaluation and visualization was conducted using Volume Graphics VGStudio Max 3.3, Heidelberg, Germany [28].

2.1.1. The XCT Thresholding Procedure for Gold in the Core Samples.

Thresholding is a process of material segmentation in X-ray computed tomography [16], in which materials or features of interest are mathematically separated from a background by distinguishing XCT model voxels according to threshold grey-scale values. To distinguish between voxels that represent gold, voxels that represent sulphides and voxels that represent matrix silicate minerals, we employed the global segmentation technique reported in [24]. Briefly, the global segmentation operation evaluates the grey-scale histogram of the entire core sample, identifies the main peaks in the histogram and defines the vertical segmentation line at the grey-scale value that marks the dip between the adjacent peaks. However, this method has a limitation of point spread function (PSF) [29]. Therefore, this threshold value is subsequently refined using a local threshold gradient search, in which the VGStudio Max 3.3 software identifies the sharpest change in grey value around the initial region of interest [24].

Figure 1 documents the grey value histograms for samples JJ01, JJ02, JJ04 and JJ05, wherein the automated global and local segmentation thresholding techniques have defined three main peaks. Based on the mineral densities and model mineral X-ray attenuation coefficients for the

minerals that we have identified in our core samples (Table 1), we assume that the left peak denotes the less dense bulk silicate mineral matrix, the middle peak represents the sulphides, and the right peak denotes the much denser gold. Gold grains were defined using the minimum grey value threshold of 59,868. The peak of gold shifts a bit among the samples, but we still use the same threshold value for all the samples because the variation is not much. Sulphides were defined using the minimum threshold of CT number 49,774. These histogram-derived threshold values represent mathematical transformations of the original X-ray data, which were collected across 16 bit grey values. Because of the closeness between X-ray attenuation coefficients between the different sulphide minerals (Figure 1e), the XCT grey value alone could not distinguish between the different sulphide phases. The validity of these peak assignments was confirmed by comparing the grey value distributions in XCT image slices to correlated polished surfaces that were evaluated using optical microscopy and scanning electron microscopy (SEM). Notably, the SEM images revealed that many of the gold grains were much smaller than the 35 µm XCT scanning resolution. This partial volume effect is one reason for the broadness of the gold peaks (Figure 1), and although these partial volumes still allow identification of where gold is preferentially sited (by raising the voxel grey value), it does mean that the XCT-based approach should be acknowledged as being semi-quantitative. Using the thresholded data, we could visualize mineral grain size distribution and textures in 3D space. Furthermore, the thresholded data enabled us to generate volumes for each of the

mineral phases (which were then used to calculate masses by considering known densities (Table 1)).

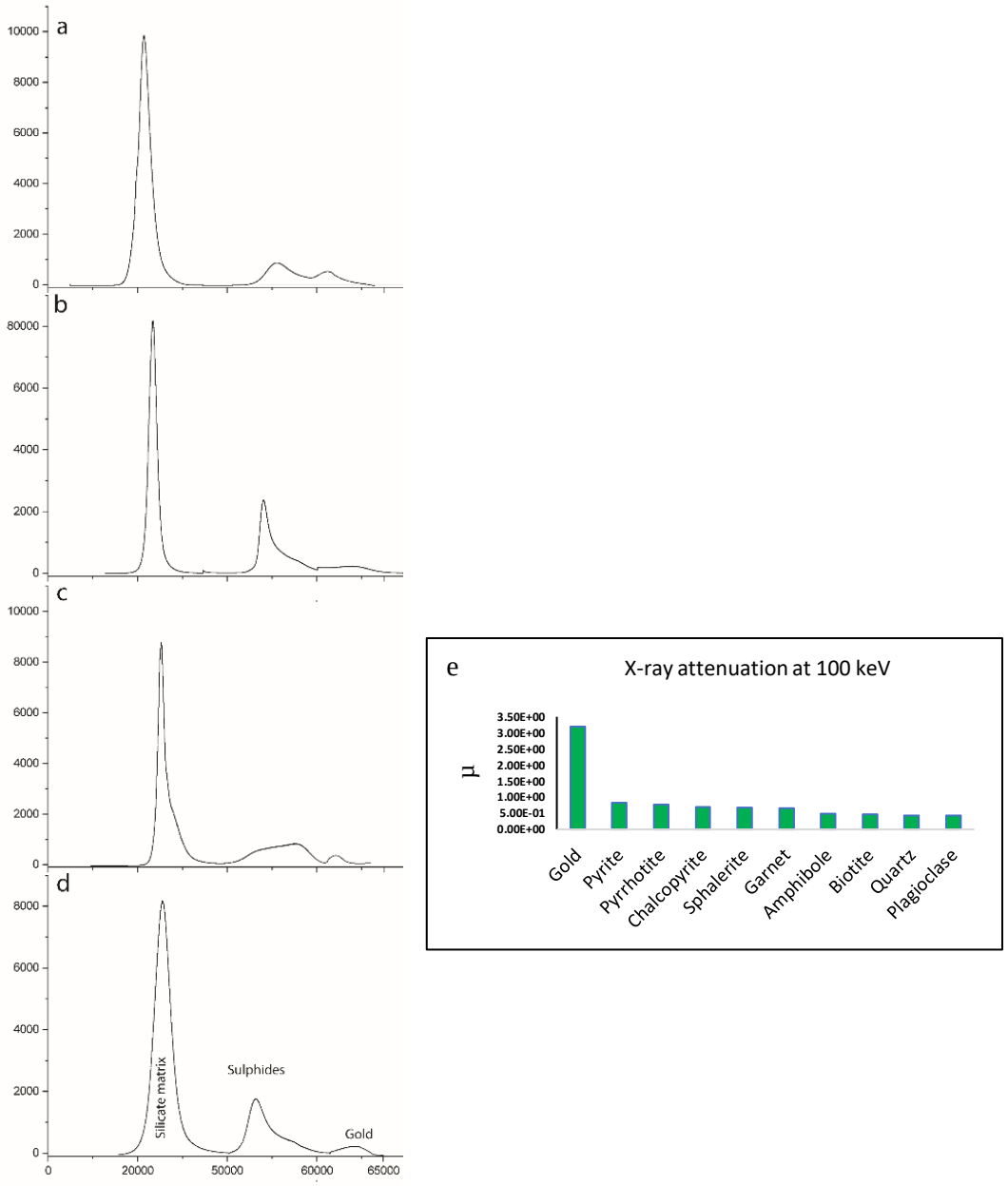

Figure 1 (a-d). *Histograms of the core samples from grey value mapping used in thresholding. The histograms distinguish three dominant peaks. The left peak denotes the less dense bulk silicate mineral matrix, the middle peak the sulphides and the right peak denotes the much denser gold mineral. Samples JJ01, JJ02, JJ04 and JJ05, x axis denotes grey values and y axis frequency. (**e**): X-ray attenuation coefficient at 100 keV [30]. The graph indicates that at 100 KeV energy, gold will have the highest attenuation by a large margin. The XCT technique could not resolve different sulphides from one another as their density range is narrow, but clearly distinguishes gold as high atomic number phases distinct from the sulphides.*

Table 1. Density range and X-ray attenuation coefficients of minerals present in the core samples. Density data are collected from [31] and X-ray attenuation coefficients are calculated using an Excel sheet developed by [32].

Mineral	Density g/cm³	X–Ray Attenuation Coefficient
Gold	19.3	3.20 E^{00}
Pyrite	5.01	8.32 E^{-01}
Pyrrhotite	4.65	7.72 E^{-01}
Chalcopyrite	4.19	6.96 E^{-01}
Sphalerite	4.1	6.81 E^{-01}
Garnet	3.93	6.52 E^{-01}
Amphibole	3	4.98 E^{-01}
Biotite	2.8	4.65 E^{-01}
Quartz	2.65	4.40 E^{-01}
Plagioclase	2.61	4.33 E^{-01}

2.1.2. Calibration of the XCT Thresholding Procedure for Gold in the Core Samples

To empirically verify that the small peak is indeed gold and is not confused with other minerals, gold grains identified in XCT (brightest and most dense spots) were intersected and proved in reflected light microscopy. We cut the core at an appropriate location and made thick sections. Reflected light microscopy identifies ubiquitous gold grains within the core samples, which proves that the dense minerals identified in XCT are indeed gold (Figure 2). Furthermore, in Figure 2c, the gold grain identified in XCT is proved in the reflected light microscopy in Figure 2d. We can see this gold grain in the reflected light microscopy. This empirically proves that the dense minerals found in our samples are gold. In addition, we extracted grey values representing 100% gold, grey values representing 100% sulphides and grey value representing 100% silicates. Extracted XCT grey values for gold brightest spot grains range in 61,586–65,000, falling within the small peak on the histogram; those for sulphides range in 50,000–59,000, falling within the sulphide peak; and those for silicates range in 1600 and 49,771,

falling within the silicate peak. This shows that our segmentation method is correct. However, grey values obtained from different scanners may differ, which would make comparison of the data difficult. To standardize this, grey values need to be correlated with Hounsfield units. This can be achieved by plotting the linear attenuation coefficient of the minerals in the core samples against grey values to provide a linear fit and a regression equation. The linear attenuation coefficient for each mineral at 100kev energy can be converted to CT numbers' Hounsfield units (HU) using the equation HU = (μ material − μ water)/(μ water) × 1000, where μ material = linear attenuation coefficient of material and μ water = linear attenuation coefficient of water. This can make the data comparable and has been demonstrated by the authors in [33].

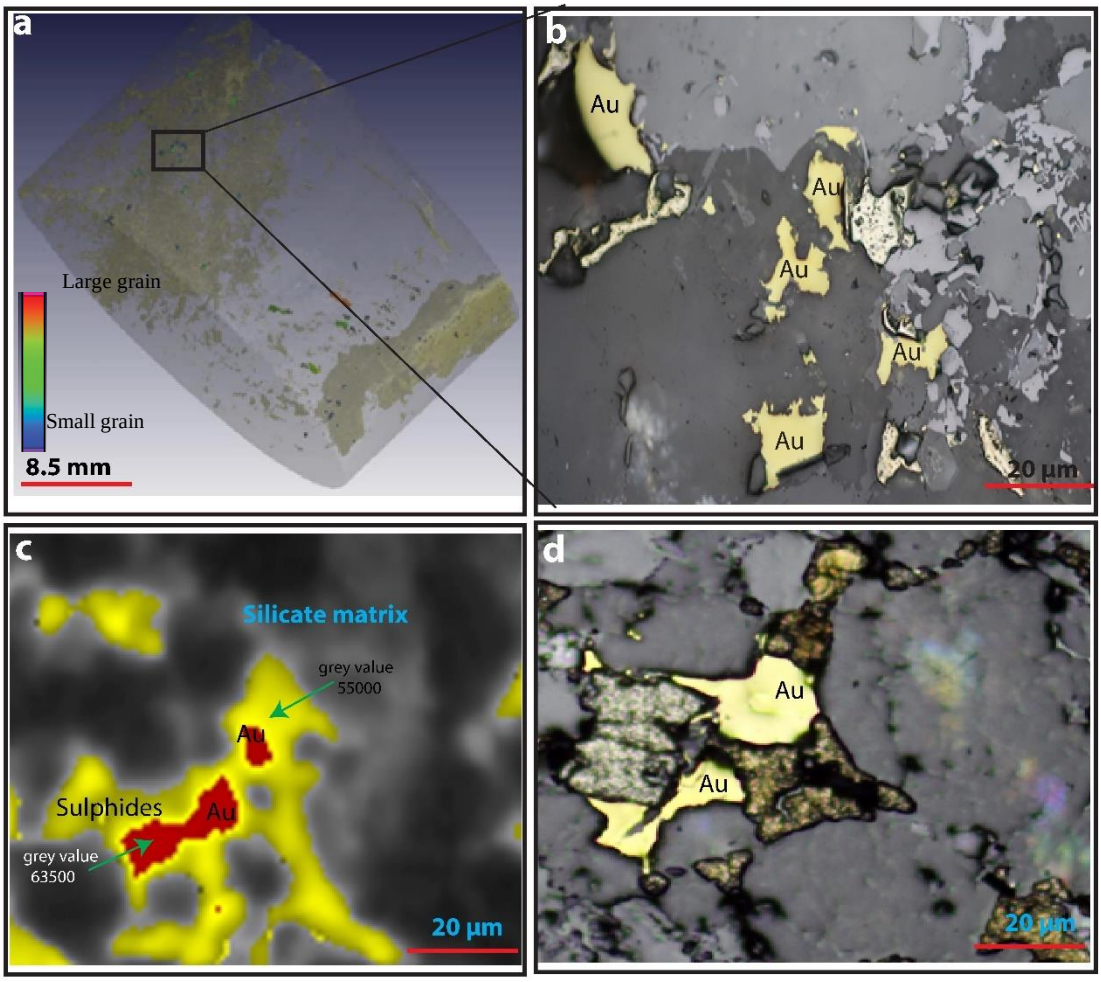

Figure 2. *X-ray computed tomography and reflected light images indicating gold grains identified in XCT and gold grains identified in reflected light microscopy. (a) The drill core was cut on the rectangle shown to make thick sections. Grey colour in the drill core is the*

silicate matrix, the yellow colour indicates sulphides and other colours represent gold, distributed according to gold grain volume (warm colours = large grains, cold colours = smaller grains). (b) Reflected light microscopy shows ubiquitous presence of gold, which proves that the dense minerals we see in XCT are indeed gold. (c,d) Gold grain in XCT, same grain in reflected light microscopy. In Figure 2c, the yellow colour indicates sulphides, dark colour indicates silicate matrix and red colour indicates gold. Figure 2c is coloured according to density (warm colours = most dense gold grains, yellow colours = medium density sulphides, dark/grey colour = less dense silicate matrix).

2.2. Thin and Polished Section Photo Montages

Based on the gold distribution information provided by XCT data, we physically cut the cores samples at appropriate positions to intersect the identified gold and made thin and thick sections. The appropriate surfaces were polished and subjected to reflected and transmitted light microscopy. Thin and thick sections were described using a Nikon Eclipse E 200 petrological microscope at Stellenbosch University; digital photomicrographs were captured and stitched to make image mosaic of the thin and thick sections using PT GUI software. The 2D optical microscopy image was compared with the 3D XCT image for a specific region of the samples. The XCT data and microscopy data were aligned manually by visually aligning prominent features using commercially available Volume Graphics software [28]. Correlative microscopies in other geoscience studies (e.g., fluorescence microscopy + SEM [34]) have proven to be more precise and can expose the physical and chemical character of ore minerals at a better spatial resolution and analytical precision [35].

2.3. SEM Mapping

Scanning Electron Microscopy combined with an Electron Dispersive Spectrometer (SEM-EDS) was utilized to provide further insights into the mineralogy, textures and distribution of gold in the evaluated samples. Polished blocks, previously evaluated using reflected light optical microscopy, were coated with carbon to prevent localized charging and any resultant

distortions or reflections of the electron beam. The SEM/EDS analyses were conducted at the Electron Microscopy Unit of the Central Analytical Facility (Stellenbosch University, South Africa) using a Zeiss EVO MA15VP Scanning Electron Microscope. SEM/EDS analyses were carried out in a nitrogen atmosphere at pressures from 65 to 96 Pa, voltages from 20 to 30 kV, working distance for EDS analyses of 8.5 mm and magnifications ranging between 1000× and 5000×.

2.4. Fire Assay

Fire assay analyses were conducted on subsamples of each of the cores that were scanned using XCT. Each subsample sent for fire assay was sectioned both physically and in the corresponding XCT reconstructed model. This ensured that the assayed gold grades could be accurately compared to calculated gold grades, which were derived from the XCT gold volumes generated after the thresholding procedure described in Section 2.1.1. The remaining core sample was reserved for future analytical work. Fire assay analyses were conducted at the ALS mineral services laboratory (Johannesburg, South Africa). Gold was assayed using fusion process at temperatures of 1200°C to obtain the lead button that was then subjected to cupellation. Full details for this analytical technique are reported in reference [26].

3. Results

3.1. Thresholding and Quantification using XCT Data

The histogram of the measured grey values (Figure 1) provides a clear indication that the core sample contains mineral material from three markedly different density (or more correctly; X-ray attenuation coefficient) fractions viz. the silicate matrix, the sulphide paragenesis, and a

distinctly high density material that we assume to largely represent gold. Other mineral phases that could be present with such high X-ray attenuation coefficients include galena, barite and native silver; however, none of these minerals were identified in the follow-up petrographic investigations.

The silicate mineralogy is quantitatively dominant throughout the core samples evaluated and have grey values ranging between 1600 and 49,771. Detailed interrogation of the XCT data revealed that we can see foliation within the silicates (Figure 3a) and pick out some garnet porphyroblasts (Figure 3b). Garnet porphyroblasts (density 3.93 gcm^3) have relatively high grey values in the range 42,000 to 47,000, which are close to the grey value range expected for sulphides (Table 1). Thin sections made from the core prove the presence of garnet (Figure 3c). Due to the closeness of garnet grey values and those of sulphides, there could be a possible overlap of garnet with sulphides' peak. Immediately adjacent to the bright sulphides vein, there is a change in grey values, which may be an indicator of hydrothermal alteration (Figure 3b), followed by a dark silicate matrix with grey values less than 20,000. From the silicate matrix, we can see three phases, garnets, hydrothermally alteration adjacent to the vein and the dark silicate minerals that cannot be differentiated due to close density ranges. From microscopy, these dark silicate minerals are quartz, feldspars, amphiboles and biotite (Table 1).

The sulphide mineral paragenesis is represented in the XCT data by grey values ranging between 49,774 and 59,868. From reflected light microscopy, this assemblage includes minor amounts of chalcopyrite, sphalerite and pyrrhotite, with pyrite as the dominant (>80% modal proportion among sulphide minerals) sulphide phase. The density for these sulphides range between 4.1 and 5.01 g/cm^3 (Table 1), and it is thus, not possible to discern between the different sulphide minerals using XCT alone (highlighting the need for correlative

microscopies in order to derive additional detailed mineralogical information (Section 4.2)). In the core samples evaluated, the grey values representing the sulphides are generally distributed along planar features which reflect the main vein network, and which in turn is structurally controlled in response to the regional stresses experienced by the geology during its deformational history. By considering the number of voxels ascribed to sulphide minerals through our thresholding approach and by deriving a weighted average density for the sulphide paragenesis, the mass of sulphide could be estimated for each of the core samples. These estimated masses ranged between 1.15 and 5.3 g (Table 2).

Gold in the core samples was identified by using a minimum grey value threshold value of 59,868. This represents the brightest pixels in the XCT images (Figure 4), since gold has the highest X-ray attenuation coefficient of all the minerals identified in the cores (Figure 1e). The presence of gold in our samples was confirmed using reflected light microscopy, Scanning Electron Microscopy (Figures 2 and 3d), and traditional fire assay. Voxels representing gold were predominantly found in association with the sulphides in the vein network, although a small proportion of these voxels were also located in the silicate host rock, particularly in close proximity to the vein network (Figure 4a, b). The identified gold grains ranged in size between less than 0.14 to 0.7 mm in diameter, and a calculation based on the volume of the gold voxels and the known density of gold (19.32 $g.cm^{-3}$) estimates that the mass of gold in each sample ranges between 0.095 and 0.25 g, corresponding to a calculated gold grade of between 0.03 and 0.14 ppm (Table 2).

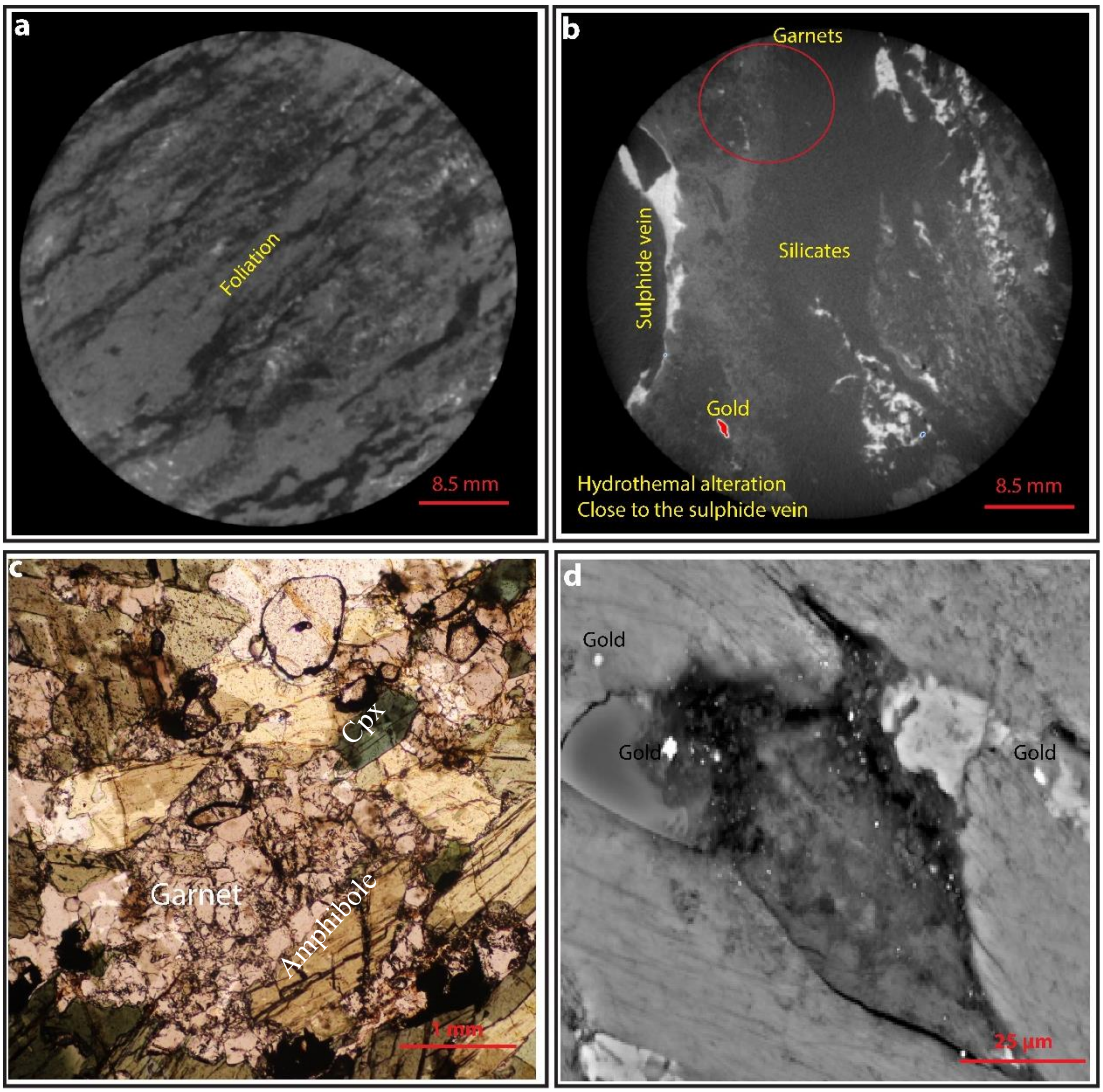

Figure 3. *(**a**) Foliation within the silicates in the XCT image slice; the foliation is attributed to minerals biotite, amphibole, garnet, muscovite, quartz and feldspar. (**b**) XCT image slice of silicate matrix minerals bright pixels in red circle depicts garnet porphyroblasts identified as small round white dots. (**c**) Thin section made from the core proving the presence of garnet. (**d**) Backscattered gold elemental map obtained from the SEM analysis of the 2D cut surface of the core. The bright spots represent the spots where gold was found. Gold grains are small in SEM due to partial volume effect. Sample JJ01 and JJ02.*

Table 2. Distribution of gold and sulphides in analysed drill core samples. Average density of sulphides was calculated by averaging the densities of individual sulphides identified in 2D microscopy.

Gold.

Sample	Weight of Core (g)	Gold Volume (mm^3)	Density (g/cm^3)	Mass of Gold(g)	Gold Grade XCT (ppm)
JJ 01	136.17	4.93	19.30	0.10	0.07
JJ 02	384.70	7.18	19.30	0.14	0.04
JJ 04	89.56	6.70	19.30	0.12	0.14
JJ 05	919.05	13.32	19.30	0.26	0.03

Sulphides.

Sample	Weight of Core (g)	Sulphide Volume (cm^3)	Avg Density g/cm3	Mass of Sulphides (g)	Concentration of Sulphides %
JJ 01	136.17	0.26	4.48	1.15	0.84
JJ 02	384.7	1.17	4.48	5.26	1.37
JJ 04	89.56	0.72	4.48	3.24	3.62
JJ 05	919.05	0.34	4.48	1.52	0.17

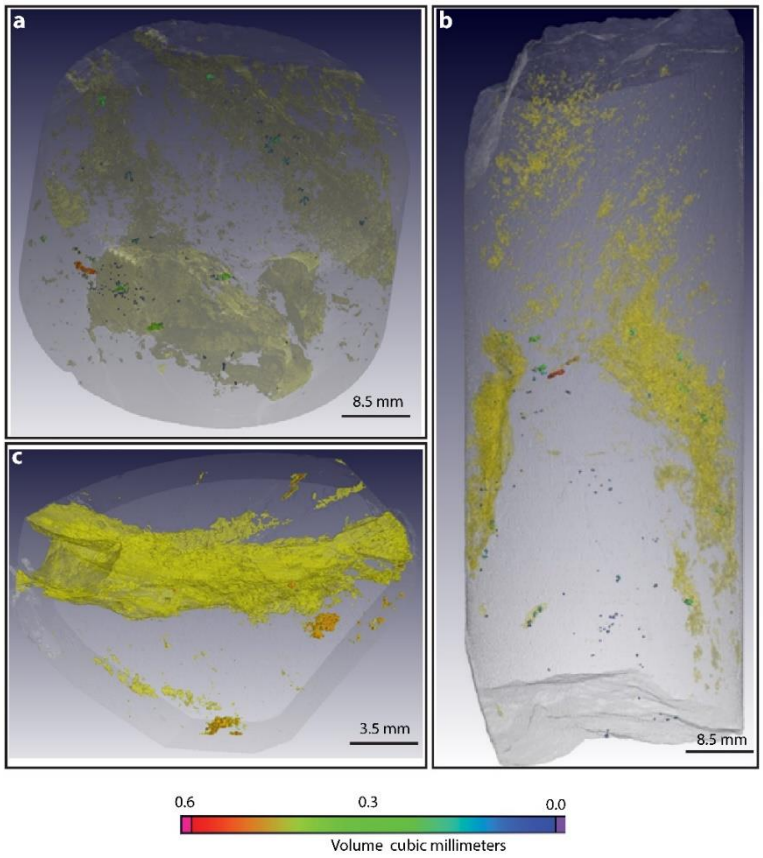

***Figure 4**. **(a,b).** XCT images showing 3D distribution of gold in mineralized drill core samples from gold-rich hydrothermal veins. The grey colour is the silicate matrix, the yellow colour indicates sulphides and the other colours represent gold, distributed according to gold grain volume (warm colours = large grains, cold colours = smaller grains). Samples JJ01 and JJ05 (**c**) is a thick section made from sample JJ04.*

3.1.1. Fire Assay to Calibrate XCT Threshold Values

Fire assay analyses were conducted to confirm the presence of gold in our samples and to calibrate the calculated gold grades derived from XCT data. The fire assay analyses were conducted on quarter cores derived from the original scanned cores, and these data compared to calculated gold grades for the corresponding quarter of the core, which was sectioned digitally from the 3D XCT model (Figure 5). Fire assay data reveal that the gold grades for the respective cores in ppm are 0.03 (JJ1), 0.02 (JJ2), 0.01(JJ4) and 0 (JJ5), (Table 3). The fire assay shows a strong and positive linear relationship with the gold grades calculated from our XCT thresholding protocol (Figure 6a: $y = 0.5888x - 0.0011$; $r^2 = 0.5$). The linear best-fit line has a slope that is less than the 1:1 line, indicative that the XCT protocol generally overestimates the mass of gold present in the core samples.

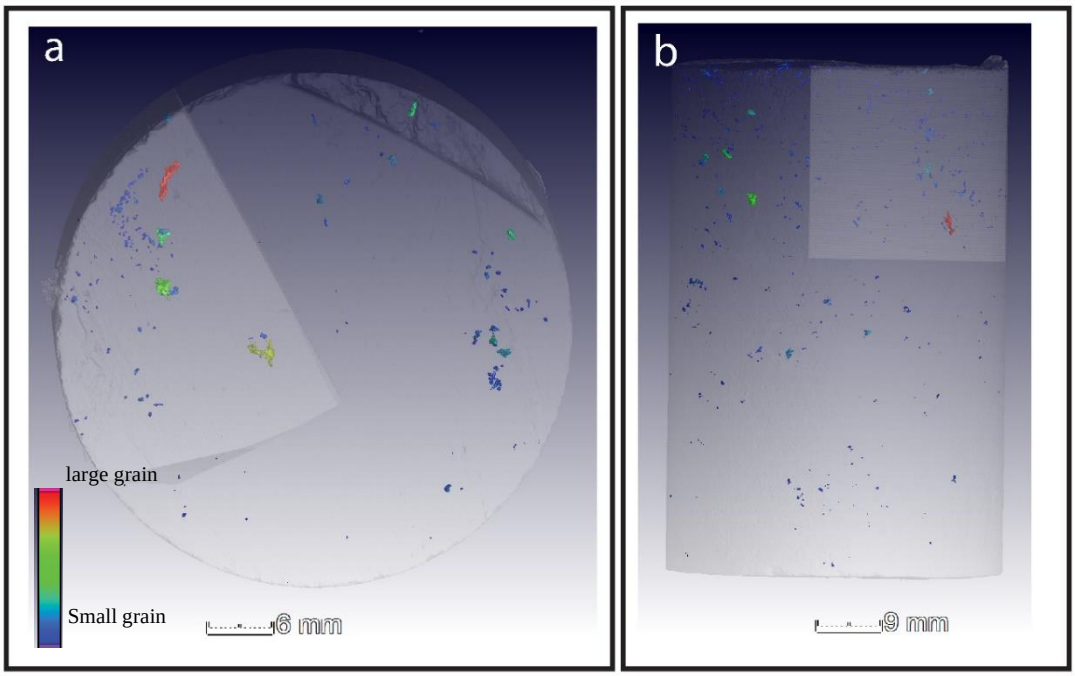

Figure 5 (a,b). *Quarter cores that were sent for fire assay analysis cut from the whole cores. The grey colour in the drill core is the silicate matrix and other colours represent gold, distributed according to gold grain volume (warm colours = large grains, cold colours = smaller grains). Samples JJ01 and JJ02.*

The equation of the best-fit line does however provide a useful internal calibration for the XCT data. Figure 7 compares the distribution of gold from the XCT model data using the original threshold value derived from the global segmentation protocol 59,868, to a threshold value that has been selected to ensure that the XCT calculated gold grades fall on the 1:1 line with fire assay gold grades. This exercise reveals that calibrating XCT values based on fire assay to the threshold grey value in our case, of 63,000, other dense minerals disappear, and gold is only present in the vein and not necessarily in the wall rock (Figure 7b) and is ~1:1 with fire assay (Figure 6c, Table 3), disregarding the JJ05 sample in which the assayed gold grades were below the detection limit. If we take grey values below 63,000, we have more gold grains making XCT to generally overestimate the mass of gold present in the core sample (Figure 7a).

A final test was conducted on the calibrated XCT core models in order to comment on the in situ nugget effect that may be induced by only assaying a quarter core. Quarter cores have relatively high gold values than the whole core due to the nugget effect (Table 3), except sample JJ04. The nugget effect is attributed to the heterogeneous distribution of gold grains in the core samples. Some regions of the core are rich in gold and others are not. This is so because vein systems typically contain both barren and mineralized segments with gold grade varying laterally, vertically and across the core. Furthermore, finer grained gold mineralization usually has a high geological nugget effect [36]. Hence, some of the quarter cores have high gold values compared to the whole core (Table 3).

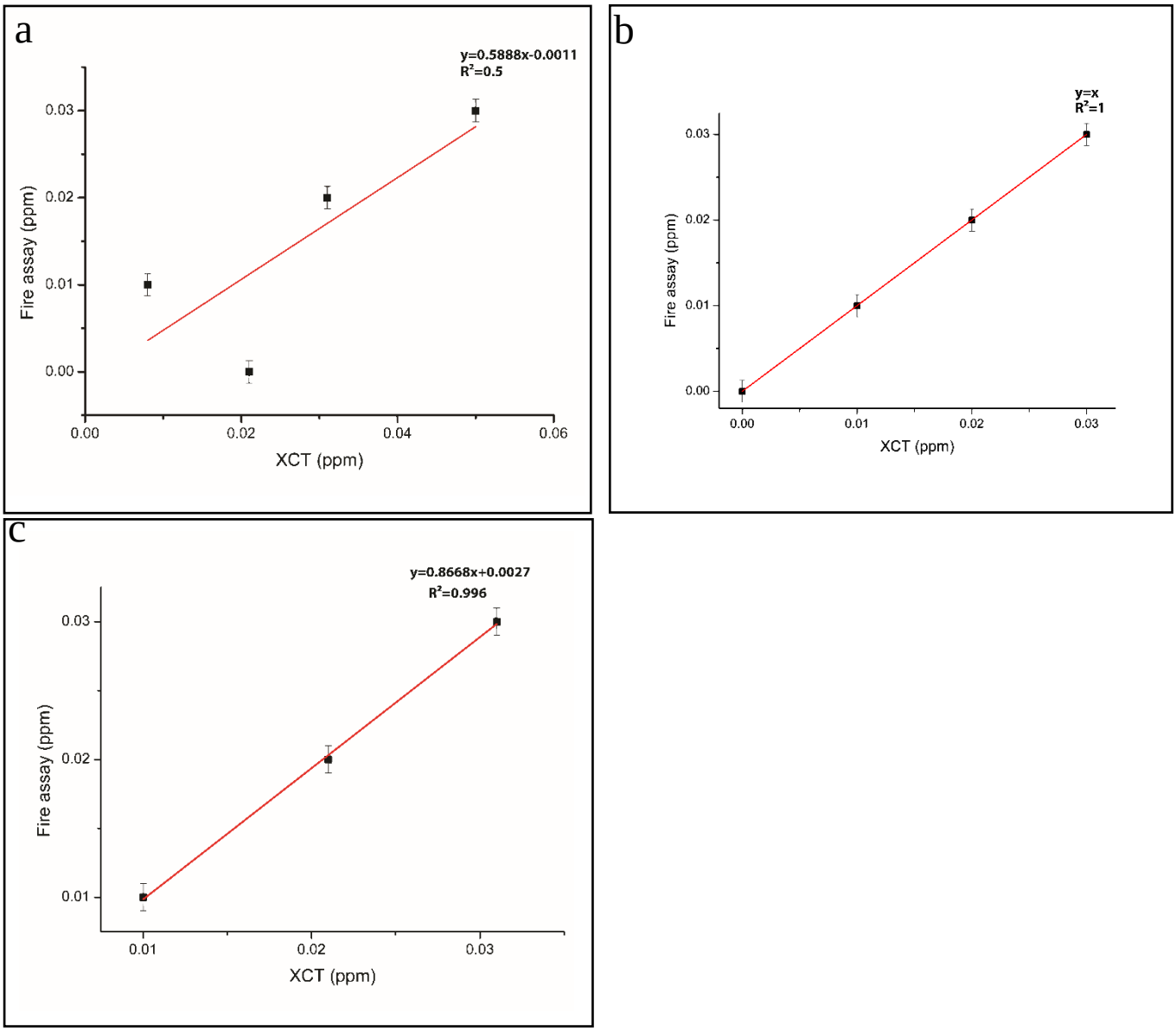

Figure 6. *Correlation between XCT and Fire assay data. (**a**) Correlation between XCT and fire assay of quarter core before calibration. (**b**) 1:1 linear best fit line of XCT and fire assay. (**c**) Correlation between XCT and fire assay of quarter core after calibration. Error bar ± 0.001.*

Table 3. (Top) Gold grade of the scanned core samples calculated by XCT analysis and gold grade obtained by fire assay. (Middle) Calculated gold grade after calibrating using fire assay at threshold grey value of 63,000. (Bottom) comparison of gold grades before and after calibration.

Sample	Weight of Core (g)	Gold Volume (cm3)	Mass Gold (g)	Gold Grade XCT(ppm)	Gold Grade Fire Assay (ppm)
JJ 01	50.56	0.0013	0.025	0.050	0.03
JJ 02	50.085	0.0008	0.015	0.031	0.02
JJ 04	60.175	0.00025	0.005	0.008	0.01
JJ 05	55.205	0.0006	0.012	0.021	0

Sample	Weight of Core (g)	Gold Volume (cm^3)	Mass Gold (g)	Gold Grade XCT(ppm)	Gold Grade Fire Assay (ppm)
JJ 01	50.56	0.0008	0.015	0.031	0.03
JJ 02	50.085	0.00054	0.010	0.021	0.02
JJ 04	60.175	0.0003	0.006	0.010	0.01

Sample	Gold Grade before Calibration (Quarter Core) XCT(ppm)	Gold Grade after Calibration (Quarter Core) XCT(ppm)	Gold Grade Fire Assay (Quarter Core) (ppm)	Gold Grade Whole Core after Calibration XCT(ppm)	% Difference between Calibrated Whole Core Gold XCT Data and Fire Assay
JJ 01	0.05	0.031	0.03	0.02	−0.04
JJ 02	0.031	0.021	0.02	0.004	−0.04
JJ 04	0.008	0.01	0.01	0.043	0.03
JJ 05	0.021	0.01	0	0.01	0.01

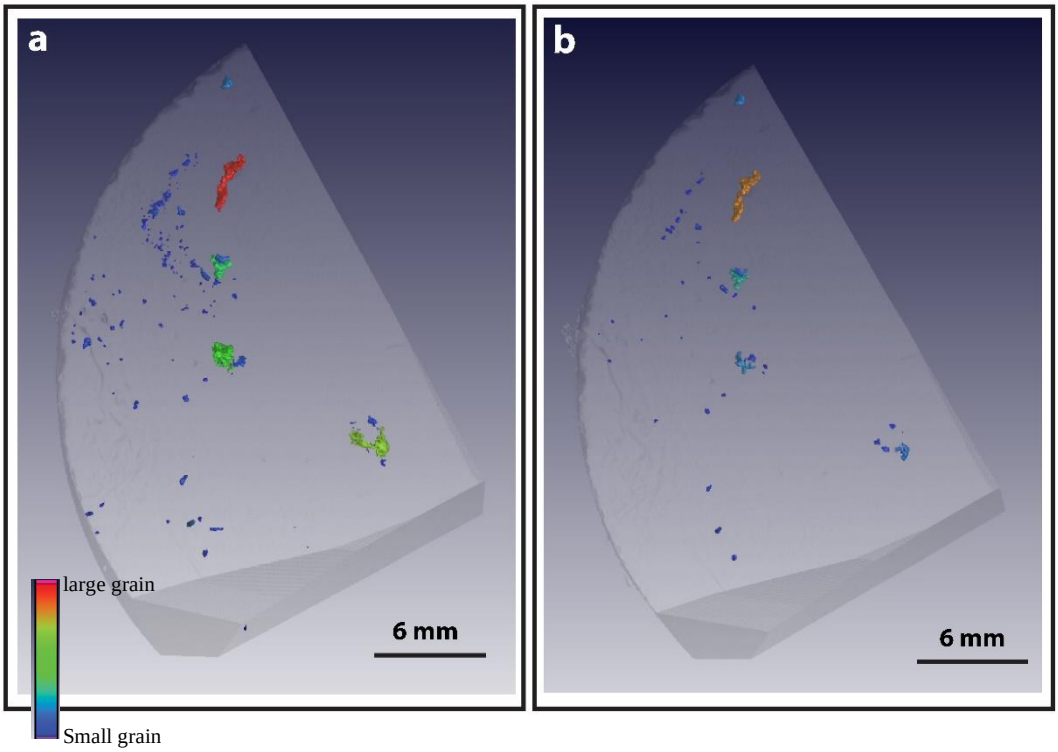

Figure 7(a,b). *Distribution of gold grains in the core after segmenting using a threshold value of 59,868 and 63,000 grey values respectively, at 59,868 XCT generally overestimate the mass of gold present in the core sample. The grey colour is the silicate matrix and other colours represent gold, distributed according to gold grain volume (warm colours = large grains, cold colours = smaller grains). Sample JJ01.*

3.2. Textural and Mineralogical Correlations between 2D and 3D Study Approaches

The preceding section highlights the utility of XCT towards understanding and semi-quantitatively analysing gold distributions in three dimensional reconstructions of exploration borehole core samples. When used independently however, this approach fails to discern between different sulphide minerals in the assemblage and poorly resolves microstructural features that may have important implications for the exploration efforts. It is thus imperative to combine 3D XCT analyses with conventional 2D microscopies in order to derive the full value out of a given exploration drilling program. Figure 8 compares a montage of 2D optical (reflected light) microscopy images with the corresponding image slice extracted from an XCT

model. The correlation was conducted manually by visually aligning prominent features using the commercially available Volume Graphic software. An artefact of this imperfect overlap is depicted in Figure 8a, in which a notable gold grain is intersected in the image slice but was either slightly below the polished surface or was above the polished surface and was subsequently cut and polished away. Indeed, when preparing polished sections of finely disseminated gold mineralization, intersection of discrete gold grains can only be fortuitous if cutting and polishing is not guided by prior XCT analysis.

Figure 8b further contrasts the level of mineralogical detail that is achieved in the XCT image slice versus the petrographic montage. The XCT model provides a three-dimensional overview of the sulphide spatial distribution, reveals low-level textural information (e.g., mineral stretching along the shear plane is clearly evident), and enables a truer representation of the mineral size distributions (2D approaches provide apparent mineral sizes). However, it clearly lacks in its ability to discern between different sulphide mineral phases. In comparison, the 2D reflected light petrographic montage enables that the individual sulphide mineral phases can be identified, their paragenetic relationships can be more deeply investigated, and additional microstructural details (e.g., mica fish, rotated porphyroblasts) can be used to augment and enrich the understanding of the structural controls on the mineralization. Some disadvantages of the 2D petrographic study approaches include that they are destructive to the original core sample, the samples require preparation (i.e., cutting and polishing may be time-consuming), selection of sub-samples for thin/thick sectioning may introduce unconscious bias into the ultimate dataset, true mineral sizes cannot be discerned, and the 3D kinematics associated with the structural controls cannot be fully studied. These results (summarized in Table 4) clearly highlight that there is extra information that can be obtained from microscopy that cannot be

obtained from XCT, and vice versa. Hence, from an optimized exploration perspective, it is important that these techniques should be used correlatively.

Table 4. Summary on information that can be obtained from combined approach.

2D Petrography	3D Computed Tomography	Combined and 2D and 3D Correlative Approach
Apparent size	True size and orientation	True size
Relative sense of motion (e.g., sinistral vs. dextral) associated with structural features	Absolute 3D orientation of major structures	Deeper understanding of orientation of major structures
Resolution determined by lenses on microscope	35 μm voxel resolution	Enables that 2 μm resolution can be spatially constrained within a 35 μm voxel size theoretical XCT model
Observation of microstructural features e.g., mica fish, rotated porphyroblasts, mineral stretching, etc.	Only major structures observed, possible identification of mineral stretching in dense gold samples	Microstructural details can be positioned in 3D space given x,y z coordinates
Identification of individual mineral phases	Broad categorization of mineral phases based on X-ray attenuation coefficients	A better and more comprehensive understanding of mineral phases. Identified mineral phases can be quantified and positioned in 3D space

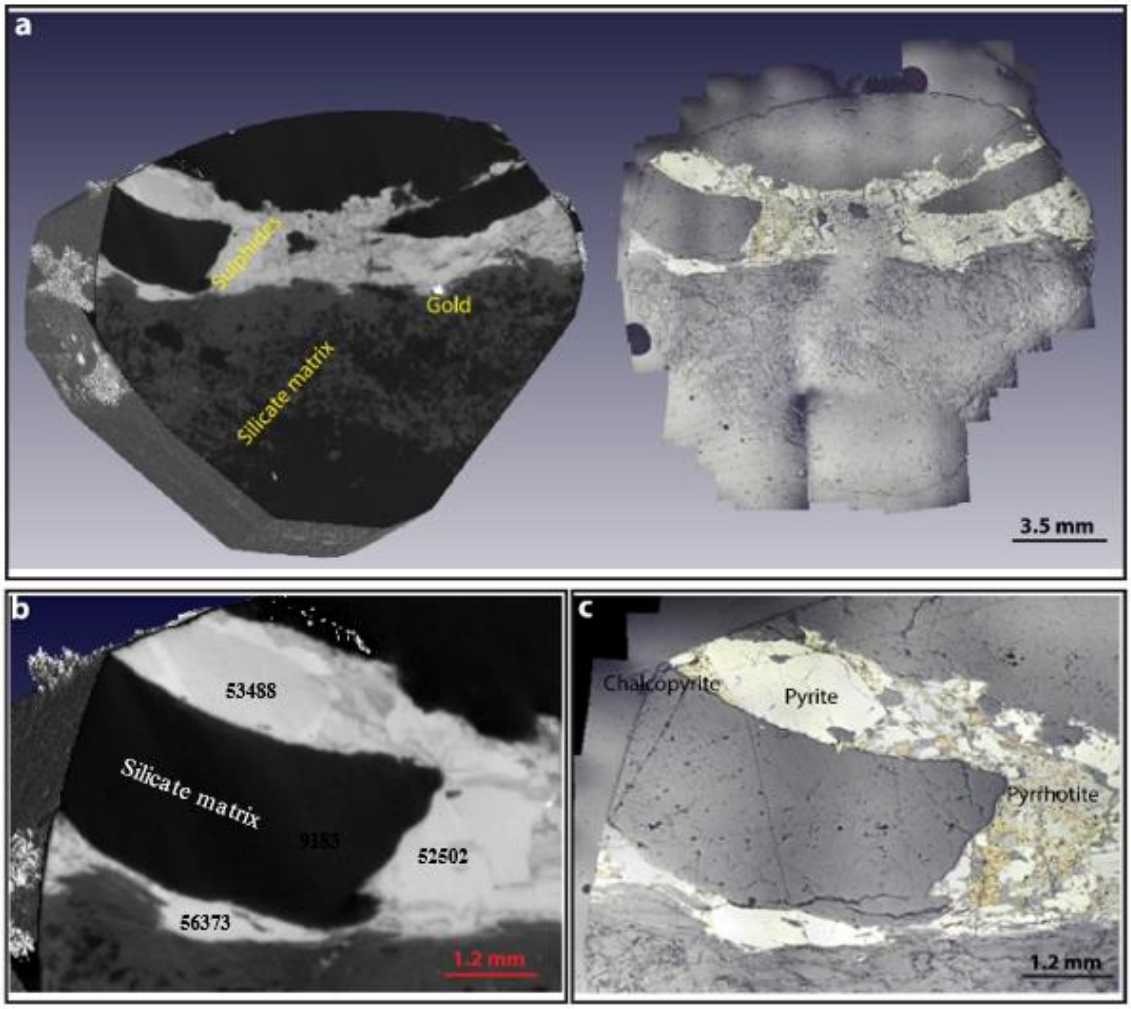

Figure 8 (a). *Precise overlay of thin section and XCT scan images in 3D. The correlation was conducted manually by visually aligning prominent features using Volume Graphic software. A notable gold grain is intersected in the XCT image slice but was either slightly below the polished surface or was above the polished surface and was subsequently cut and polished away. The high-resolution X-ray computed tomography and microscopy analyses indicate that gold and accessory sulphides are not randomly distributed but rather follow specific orientation. They are distributed along shear fracture planes rather than disseminated throughout the cores. This suggests that gold was precipitated along the shear plane together with the sulphides during the ore-forming processes. The bright gold grain is not seen in reflected light microscopy, but it is easily seen in XCT image. (**b**) Zoomed in image of sulphides from XCT indicating that they cannot be differentiated due to a narrow density range. (**c**) The sulphide mineral assemblage comprises pyrite, pyrrhotite and chalcopyrite determined from detailed 2D examination of polished sections. Thick section cut from sample JJ04.*

4. Discussion

The use of XCT in combination with microscopy provides an excellent tool for understanding gold mineralization, which is often nuggety and difficult to study because of its ppm-level grades. Although the application of this combined approach is not yet widespread, this approach overlays complementary datasets from 2D and 3D analytical protocols, thereby allowing a better and more comprehensive understanding on the distribution and structures controlling gold mineralization. In order to investigate the feasibility of the combined approach and its practical utility, we consider an example from the Manondo-Choma gold prospect (southern Malawi).

4.1. Advantages of Correlative Approaches to Exploration: Case Study from the Manondo-Choma Mineralization (Malawi)

4.1.1. Geological Context

The Kirk Range is a medium- to high-metamorphic grade mobile belt which is related to the Southern Irumide orogeny and which is located in south-central Malawi [37]. It is situated approximately 40 km north-west of Blantyre and lies between latitudes 15.30° S to 15.31° S and the longitudes 34.82° E to 34.85° E, near to the western border between Malawi and Mozambique. The major lithologies in the area comprise a suite of NE trending gneissic rocks that underwent amphibolite-granulite facies metamorphism [38]. These lithological units are characterized by polyphase deformation showing evidence of reworking possibly by the pan-African orogeny (800–550 Ma) [39].

Gold mineralization at the Manondo-Choma prospect has recently been described by the authors in [38]. Briefly, the gold is hosted predominantly in biotite schists and gneisses and is

associated with a sulphide mineral paragenesis. Regional structures as well as mineralized quartz-sulphide vein sets exhibit a NE–SW trend, which is consistent with the deformation fabrics associated with the southern Irumide orogeny [40–42]. Textural and microstructural observations reveal that the vein sets have experienced subsequent deformation and overprinting, which has likely led to transposition of the primary gold mineralization on a regional scale [38].

4.1.2. Correlated 2D and 3D Insights into Gold Mineralization at the Manondo-Choma Prospect

Four segments of drill core were selected for detailed scanning and modelling using XCT and correlative reflected and transmitted light microscopies. The XCT reconstructions reveal that the gold is hosted primarily in sub-vertical vein structures that strike in a NE–SW direction (Figure 9b). The fine-grained gold flakes are sub-rounded in texture, range in size between 0.01 and 0.04 mm, and are typically elongated parallel to the direction of the strike of the host vein (Figure 9c). Gold grades for the different core segments range between 0.01 and 0.03ppm from fire assay and 0.01–0.031ppm calculated from XCT (Table 3; after corrections to account for nugget effects inherent in gold mineralization (see Section 3.1.1.)) and show good agreement with the gold grades measured using fire assay analytical protocols. The gold is strongly associated with sulphide minerals which also orientate preferentially in the NE–SW strike direction. Minor gold is also associated with the wall rock, perhaps reflecting a second-order lithological or geochemical control on the siting of the mineralization [38]. Although the XCT image slices show subtle differences in the grey values among different sulphide minerals, these grey values could not be used to unequivocally determine sulphide speciation and did not allow detailed comment on the textural and temporal relationships within the ore paragenesis.

Thus, to augment the gold spatial, size and shape distribution data, correlative 2D petrographic analyses were conducted on selected sub-samples of the core segments. These sub-samples were best selected based on prior evaluation of the 3D XCT models, whereby gold-rich regions of the core segment were targeted for the further detailed petrographic work. Reflected light microscopy revealed that the sulphide mineral assemblage is dominated by pyrite (~80% modal proportion), with the remaining 20% of the sulphides represented by chalcopyrite, sphalerite and pyrrhotite. Early formed pyrrhotite showed the strongest mineral stretching, which was parallel to both the stretching identified in the gold flakes and to the orientation of the main vein structure. Transmitted light microscopy enabled that microtextures and shear sense indicators could be identified within the silicate mineralogy associated with the vein structure. For example, 2D microscopy indicates the presence of shear in the silicate mineralogy within the vein structure defined by grain size reduction (Figure 9e) and display flow structures that indicate ductile deformation of the core (Figure 9 f,g). In standard 2D petrography, this information can give insights into whether the mineralized vein experienced a dextral or sinistral sense of shear (i.e., X–Y directionality). However, by considering this information in light of the known orientation of the vein from prior XCT work, the kinematics can further constrained with reference to the Z-direction. Furthermore, the correlative approach allows the microstructures observed in polished sections to be confidently positioned in X,Y,Z space (using the known depth of sub-sampling down an orientated drill string). To advance exploration efforts, these orientated and positioned microstructural data can be pulled directly into implicit modelling software as an additional layer of information which could be readily analysed and iterated to finalize geological or grade interpretations.

The outcomes from this correlative study conducted at the Manondo-Choma gold prospect thus highlight that the gold is intimately associated with sulphide mineralization in NE–SW trending

SE-dipping quartz-sulphide vein structures that show a dextral sense of shear. These structures were identified by considering the complementary 2D and 3D datasets, and the orientations are found to match those of the regional NE–SW magnetic trends identified using geophysics [32] (Figure 9a), and which are tentatively related to the southern Irumide orogeny. In addition to the value that the correlative approach unlocks for exploration at the front end of the mine value chain, it also reveals vital information that can assist during later processing and beneficiation of the ore assemblage. For example, XCT scanning provides definitive information on the size, distribution and mineralogical association of the gold, all of which can control the liberation efficiencies during minerals processing. Similarly, the distribution and semi-quantitative evaluation of the sulphide minerals (Table 2), offers a unique methodology to predict acid mine drainage capacity associated with an ore prospect, especially given that sulphide concentrations are difficult to measure using standard XRF quantification approaches [43]. Related to this, the complementary petrographic information related to sulphide speciation further has important implications for the presence of metal ‘sweeteners’ (e.g., Cu, Zn) that may add additional economic value to an ore prospect, and for the presence of any deleterious elements (e.g., As) that may require special consideration to ensure that the environmental impacts of downstream mining are minimized.

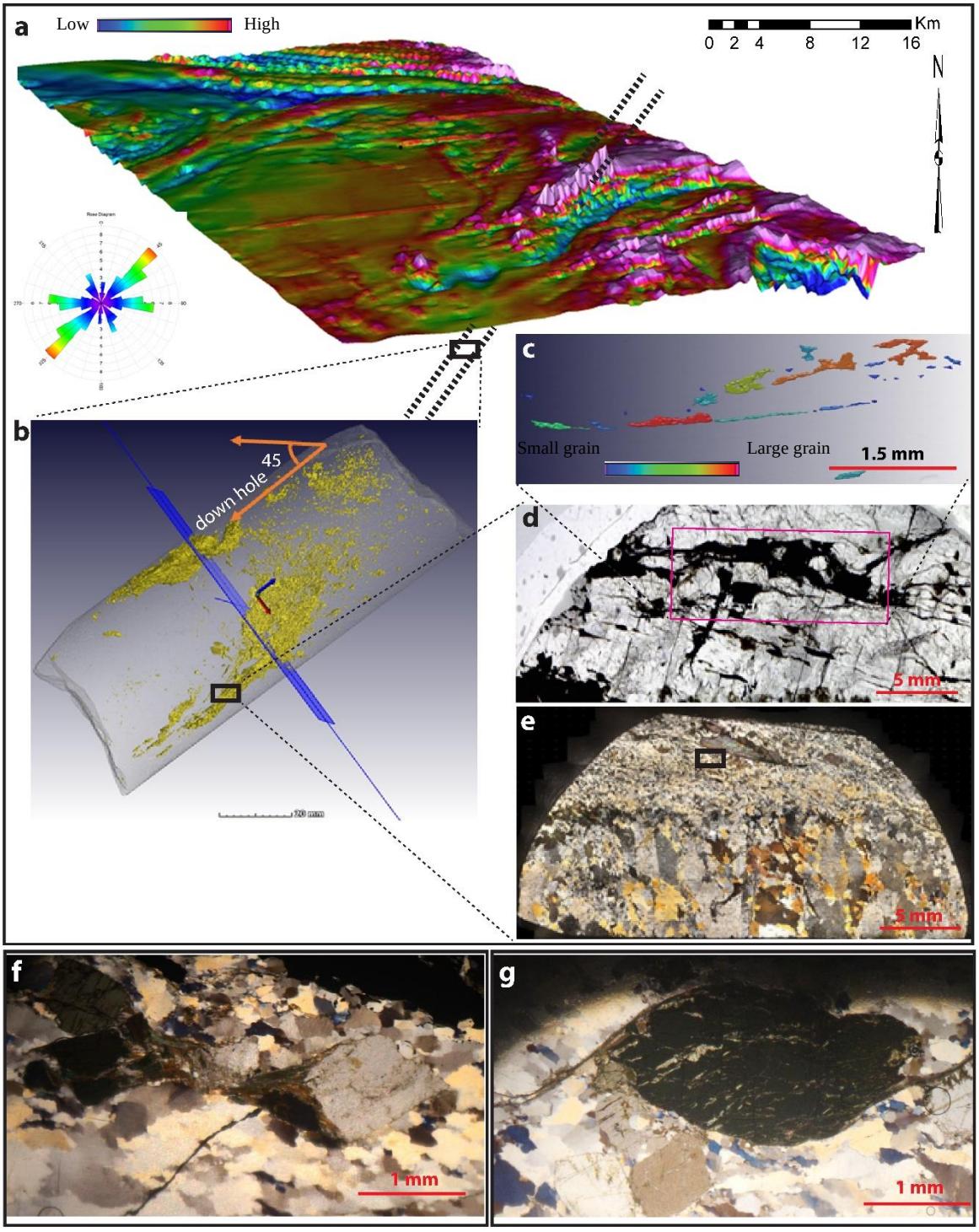

Figure 9. *Nature of gold mineralization.* ***(a)*** *Structures (faults, fractures, shear zones and dykes) that were derived from interpretation of airborne magnetic data. The magnetic data show prominent lineaments that represent faults and shear zones. The faults and fractures and shear zones are thought to have acted as conduits for mineralizing hydrothermal fluids. Rose diagram show the dominant trend of structures to be NE–SW.* ***(b)*** *Drill core drilled from the indicated hole show that the mineralized vein system and the sulphide distribution also show the same trend; the distribution of the sulphides show that the sulphide minerals occur as an interconnected subvertical network and have preferred orientation. The orientation of*

*sulphides is consistent with dominant structures in the field. The grey colour is the silicate matrix and the yellow colour indicates sulphides. (**c**) XCT scanned image of the thin section made from indicated rectangle shows gold grains have been elongated/stretched in this dominant NE orientation along the shear plane, (warm colours = large gold grains, cold colours = smaller gold grains). (**d,e**) Milled grains and stretched minerals in thin section from the drill core cut along the rectangle indicated on the drill core indicating shearing. (**f,g**) Shear sense indicators observed from thin section e above on the shear plane using a 50× objective lens. Sample JJ05.*

4.2. Recommendations for Further Development

The use of correlative microscopies in minerals exploration has not yet reached its full maturity, yet the example from the Manondo-Choma gold prospect clearly indicates its high potential for incorporation in routine minerals exploration workflows. This is especially pertinent for gold exploration endeavours given the nuggety distribution of the ore within mineralized vein sets. As bench-scale XCT machines become increasingly commercially available, it is anticipated that the approach will be adopted more extensively among exploration practitioners. However, in order to optimize the approach, the following recommendations apply:

- Need for automated alignment algorithms based on optical image analysis methodologies to match 2D montages to their positioning in XYZ space. This will help as it will require minimal initial user input. The manual approach can take 4 h.
- Need to develop software interfaces that allow XYZ positioned and orientated microstructural and mineralogical data (mapped in 3D space in XCT software) directly into common implicit and explicit geological modelling software.
- Need to optimize voxel sizes to match fine grained gold mineralization.
- Need to optimize the scanning parameters, or resolution of the sensors to better discern between different sulphide moieties using XCT technologies (and between gold and other dense minerals with high X-ray attenuation coefficients such as barite, galena etc.).

- Opportunities to develop other computed tomography techniques to provide detailed mineralogical, chemical and valence distributions in 3D space (synchrotron XRD computed tomography [44], synchrotron XRF CT [45]and synchrotron XANES CT respectively [46]).

5. Conclusions

We have highlighted a correlative approach in which 3D XCT data are combined with 2D mineralogical and chemical data to understand a complex orogenic gold mineralization. The use of XCT in combination with microscopy provides an excellent tool for understanding gold mineralization. Contextualizing 2D structural features in a 3D volume enables a deeper understanding of the structures that control mineralization and characterize the distribution of gold. Given that modern exploration efforts are targeting increasingly complex and low-grade ore deposits, the extra layers of information provided by using correlative 2D and 3D microscopies offer an exciting new tool to enhance and optimize minerals exploration workflows. It is anticipated that the approach will be adopted more extensively among exploration practitioners. Although the approach is especially well suited to gold mineralization (nuggety textures, high density and X-ray absorption coefficients of Au), it can also be applied to a range of other mineralization styles (e.g., disseminated sulphide mineralization, tungstate mineralization in skarns, etc.).

Author Contributions: Formal analysis, Stephan Le Roux and Muofhe Tshibalanganda; Supervision, Bjorn von der Heyden; Writing—original draft, Joshua Chisambi.

Funding: Funding for the project was supported in part through grants to J. Chisambi (World Bank, Skills Development Project), and to B. von der Heyden (National Research Foundation of South Africa: Grant #106006, and additional support from DST-NRF CIMERA).

Conflicts of Interest: The authors declare no conflict of interest.

References

1. Intelligence, S.G.M. *World Exploration Trends 2018*; Global S.P.: New York, NY, USA, 2019.
2. Phillips, G. Australian and global setting for gold in 2013. In Proceedings of the World Gold 2013, Brisbane, Australia, 26–29 September 2013.
3. Gaboury, D. Parameters for the formation of orogenic gold deposits Parameters for the formation of orogenic gold deposits. *Appl. Earth Sci.* **2019**, *128*, 124–133.
4. Groves, D.I. Gold Deposits in Metamorphic Belts: Overview of Current Understanding, Outstanding Problems, Future Research, and Exploration Significance. *Econ. Geol.* **2003**, *98*, 1–29, doi:10.2113/98.1.1.
5. Augustin, J.; Gaboury, D. Multi-stage and multi-sourced fluid and gold in the formation of orogenic gold deposits in the world-class Mana district of Burkina Faso–Revealed by LA-ICP-MS analysis of pyrites and arsenopyrites. *Ore Geol. Rev.* **2019**, *104*, 495–521.
6. Goldfarb, R.; Groves, D.; Gardoll, S. Orogenic gold and geologic time: A global synthesis. *Ore Geol. Rev.* **2001**, *18*, 1–75, doi:10.1016/s0169-1368(01)00016-6.
7. Grooves, D. The crustal continuum model for late-Archaean lode-gold deposits of the Yilgarn Block, Western Australia. *Miner. Depos.* **1993**, *374*, 366–374.
8. Popov, O.; Talovina, I.; Lieberwirth, H.; Duryagina, A. Quantitative Microstructural Analysis and X-ray Computed Tomography of Ores and Rocks–Comparison of Results. *Minerals* **2020**, *10*, 129.
9. Asadi, H.H.; Voncken, J.H.L.; Kühnel, R.A.; Hale, M. Petrography, mineralogy and geochemistry of the Zarshuran Carlin-like gold deposit, northwest Iran. *Miner. Deposita* **2000**, *35*, 656–671, doi:10.1007/s001260050269.

10. Pašava, J.; Svojtka, M.; Jana, Ď.; Drábek, M.; Halodová, P.; Haluzová, E. Laser ablation ICPMS study of trace element chemistry in molybdenite coupled with scanning electron microscopy (SEM)—An important tool for identi fi cation of different types of mineralization. *Ore Geol. Rev.* **2016**, *72*, 874–895.
11. Stromberg, J.M.; Van Loon, L.L.; Gordon, R.; Woll, A.; Feng, R.; Schumann, D.; Banerjee, N.R. Applications of synchrotron X-ray techniques to orogenic gold studies; examples from the Timmins gold camp. *Ore Geol. Rev.* **2019**, *104*, 589–602, doi:10.1016/j.oregeorev.2018.11.015.
12. Butler, I.B.Ł.; Nesbitt, R.W. Trace element distributions in the chalcopyrite wall of a black smoker chimney: Insights from laser ablation inductively coupled plasma mass spectrometry (LA–ICP–MS). *Earth Planet Sci.* **1999**, *167*, 335–345.
13. Godel, B. High-Resolution X-Ray Computed Tomography and Its Application to Ore Deposits: From Data Acquisition to Quantitative Three-Dimensional Measurements with Case Studies from Ni-Cu-PGE Deposits. *Econ. Geol.* **2013**, *108*, 2005–2019, doi:10.2113/econgeo.108.8.2005.
14. Kyle, J.R.; Ketcham, R.A. Application of high resolution X-ray computed tomography to mineral deposit origin, evaluation, and processing. *Ore Geol. Rev.* **2015**, *65*, 821–839, doi:10.1016/j.oregeorev.2014.09.034.
15. Baker, D.; Mancini, L.; Polacci, M.; Higgins, M.; Gualda, G.A.R.; Hill, R.; Rivers, M. An introduction to the application of X-ray microtomography to the three-dimensional study of igneous rocks. *Lithos* **2012**, *148*, 262–276, doi:10.1016/j.lithos.2012.06.008.
16. Fatima, A.; Venkatesh, A.S.; Mukherjee, R.; Agrawal, A.K.; Singh, B.; Sarkar, P.S.; Shripathi, T. 3D spatial distribution of ore mineral phases using high resolution synchrotron micro-computed tomography (μCT) combined with optical microscopy 3D spatial distribution of ore mineral phases using high resolution synchrotron micro-

computed tomography (μCT) combined with optical microscopy. *Appl. Radiat. Isot.* **2019**, *148*, 49–59.

17. Kyle, J.R.; Mote, A.S.; Ketcham, R.A. High resolution X-ray computed tomography studies of Grasberg porphyry Cu-Au ores, Papua, Indonesia. *Miner. Deposita* **2008**, *43*, 519–532, doi:10.1007/s00126-008-0180-8.
18. Naudé, G.; Hoffman, J.; Theron, S.J.; Coetzer, G. The use of X-ray computed tomography in the characterisation of coal and associated char reductants. *Miner. Eng.* **2013**, *52*, 143–154, doi:10.1016/j.mineng.2013.05.012.
19. Elangovan, P.; Hezel, D.C.; Howard, L.; Armstrong, R.; Abel, R.L. Computers & Geosciences PhaseQuant: A tool for quantifying tomographic data sets of geological specimens. *Comput. Geosci*. **2012**, *48*, 323–329.
20. Díaz, D.; Hahn, D.W.; Molina, A. Quanti fi cation of gold and silver in minerals by laser-induced breakdown spectroscopy. *Spectrochim. Acta Part B* **2017**, *136*, 106–115.
21. Sayab, M.; Suuronen, J.-P.; Molnar, F.; Villanova, J.; Kallonen, A.; O'Brien, H.; Lahtinen, R.; Lehtonen, M. Three-dimensional textural and quantitative analyses of orogenic gold at the nanoscale. *Geology* **2016**, *44*, 739–742, doi:10.1130/g38074.1.
22. Maire, E.; Withers, P.J.; Maire, E.; Withers, P.J. Quantitative X-ray tomography. *Int. Mater. Rev*. **2013**, *59*, 1–43.
23. Zhang, P.; Lee, Y.; Zhang, J. A review of high-resolution X-ray computed tomography applied to petroleum geology and a case Study, *Micron*, vol. 124, no. 102702, **2019**.
24. Le Roux, S.; Du Plessis, A.; Rozendaal, A. The quantitative analysis of tungsten ore using X-ray microCT: Case study. *Comput. Geosci.* **2015**, *85*, 75–80, doi:10.1016/j.cageo.2015.09.009.
25. Godel, B.; Barnes, S.-J.; Maier, W.D. 3-D Distribution of Sulphide Minerals in the Merensky Reef (Bushveld Complex, South Africa) and the J-M Reef (Stillwater Complex,

USA) and their Relationship to Microstructures Using X-Ray Computed Tomography. *J. Pet.* **2006**, *47*, 1853–1872, doi:10.1093/petrology/egl029.

26. ALS. *ALS Geochemistry Service*; ALS Laboratory: Johannesburg, South Africa,2013.
27. Du Plessis, A.; Le Roux, S.; Guelpa, A. The CT Scanner Facility at Stellenbosch University: An open access X-ray computed tomography laboratory. *Nucl. Instrum. Methods Phys. Res. Sect. B* **2016**, *384*, 42–49, doi:10.1016/j.nimb.2016.08.005.
28. Volume Graphics GmbH. *VG Studio Max 3.1 User's Manual*; Volume Graphics GmbH: Heidelberg, Germany, 2001.
29. Ketcham, R.A. Resolution-invariant measurements of small objects in polychromatic CT data. In Proceedings of the Developments in X-Ray Tomography XII. International Society for Optics and Photonics, San Diego, CA, USA, 8–12 March 2019; Volume 11113, p. 111130B, doi:10.1117/12.2532082.
30. Berger, M. XCOM: Photon Cross Sections Database. In *National Bureau of Standards*; Center for Radiation Research: Washington, DC, USA, 1998.
31. Density of Minerals. Available online: www.webminerals.com (accessed on 23 March, 2020).
32. Bam, L. Developing Protocols for XCT Scanning of Dense Mineral Ore Samples with Applications to Geology and Minerals Processing. Ph.D. Thesis, Stellenbosch University, Stellenbosch, South Africa, 2019.
33. Reeves, T.; Mah, P.; McDavid, W. Deriving Hounsfield units using grey levels in cone beam CT: A clinical application. *Dentomaxillofacial Radiol.* **2012**, *41*, 500–508, doi:10.1259/dmfr/31640433.
34. Gazley, M.F.; Duclaux, G.; A Fisher, L.; De Beer, S.; Smith, P.; Taylor, M.; Swanson, R.; Hough, R.M.; Cleverley, J.S. 3D visualisation of portable X-ray fluorescence data to improve geological understanding and predict metallurgical performance at Plutonic Gold

Mine, Western Australia. *Appl. Earth Sci.* **2011**, *120*, 88–96, doi:10.1179/1743275812y.0000000002.

35. Cook, N.J.; Cook, N.J.; Courtney-Davies, L.; Slattery, A.D.; Verdugo-Ihl, M.R.; Courtney-Davies, L.; Gao, W. Advances and Opportunities in Ore Mineralogy. *Minerals* **2017**, *7*, 233, doi:10.3390/min7120233.
36. Dominy, S.C.; Edgar, W.B. Approaches to reporting grade uncertainty in high nugget gold veins. *Appl. Earth Sci.* **2012**, *121*, 29–42, doi:10.1179/1743275812y.0000000013.
37. Bloomfield, K.; Garson, M.S. *The Geology of the Kirk Range-Lisungwe Valley Area*; Ministry of Natural Resources. Geological Survey Department. Bulletin No.17; Government Printer: Zomba, Malawi, 1965.
38. Chisambi, J.; von der Heyden, B. Primary gold mineralization at Manondo–Choma area, Kirk range, Southern Malawi. *S. Afr. J. Geol*. **2019**, *122*, 505–518.
39. De Waele, B.; Fitzsimons, I.; Wingate, M.T.D.; Tembo, F.; Mapani, B.; Belousova, E. The geochronological framework of the Irumide Belt: A prolonged crustal history along the margin of the Bangweulu Craton. *Am. J. Sci.* **2009**, *309*, 132–187, doi:10.2475/02.2009.03.
40. De Waele, B.; Kampunzu, A.; Mapani, B.; Tembo, F. The Mesoproterozoic Irumide belt of Zambia. *J. Afr. Earth Sci.* **2006**, *46*, 36–70, doi:10.1016/j.jafrearsci.2006.01.018.
41. Boyd, R.; Nordgulen, O.; Thomas, R.J.; Bingen, B.; Bjerkgård, T.; Grenne, T.; Henderson, I.H.C.; Melezhik, V.; Often, M.; Sandstad, J.S.; et al. The Geology And Geochemistry Of The East African Orogen In Northeastern Mozambique. *S. Afr. J. Geol.* **2010**, *113*, 87–129, doi:10.2113/gssajg.113.1.87.
42. Bingen, B.; Jacobs, J.; Viola, G.; Henderson, I.H.C.; Skår, Ø.; Boyd, R.; Thomas, R.J.; Solli, A.; Key, R.; Daudi, E. Geochronology of the Precambrian crust in the Mozambique belt in NE Mozambique, and implications for Gondwana assembly. *Precambrian Res.* **2009**, *170*, 231–255, doi:10.1016/j.precamres.2009.01.005.

43. Czerewko, M.A.; Cripps, J.C.; Reid, J.M.; Duffell, C.G. Sulfur species in geological materials–sources and quantification. *Cem. Concr. Compos.* **2002**, *25*, 657–671.
44. Leißner, T.; Diener, A.; Löwer, E.; Ditscherlein, R.; Krüger, K.; Kwade, A.; Peuker, U.A. 3D ex-situ and in-situ X-ray CT process studies in particle technology–A perspective. *Adv. Powder Technol*. **2020**, *31*, 78–86.
45. De Samber, B.; Silversmit, G.; Evens, R.; De Schamphelaere, K.; Janssen, C.; Masschaele, B.; Van Hoorebeke, L.; Balcaen, L.; Vanhaecke, F.; Falkenberg, G.; et al. Three-dimensional elemental imaging by means of synchrotron radiation micro-XRF: Developments and applications in environmental chemistry. *Anal. Bioanal. Chem.* **2007**, *390*, 267–271, doi:10.1007/s00216-007-1694-0.
46. Meneses, C.T.; Macedo, M.A.; Vicentin, F.C. Li x Mn 2 O 4 thin films characterization by X-ray, electrical conductivity and XANES. *Microelectron. J.* **2003**, *34*, 561–563.

CHAPTER 3

Primary gold mineralisation in the Lisungwe Valley area, Kirk Range, southern Malawi

A presentation of the published research paper

This manuscript has been published in the research journal *South African Journal of Geology*, after review by three anonymous reviewers. I am the first author and Dr Bjorn von der Heyden is the co-author. The manuscript represents the first detailed geological study investigating the controls of primary gold mineralisation in the mineralized Little Chisumbwiti river valley, located in the Kirk Range region which forms part of Southern Irumide mobile belt in southern Malawi. Our study area has been especially selected since it represents a region that has been historically understudied, despite its clear endowment with gold as evidenced by the previous stream sediment geochemical surveys, the prevalence of artisanal placer gold miners, and the presence of historical mining adits that were operational during the early 20th century. The manuscript employs a multi-scaled approach (using airborne magnetic and radiometric data, field mapping, and micro-scale X-ray, electron, and light characterization techniques) to comprehensively understand the nature of the gold mineralisation in the highly-prospective Little Chisumbwiti river valley. The findings are contextualized within the current understanding of Malawi's geological and tectonic history, and are used to develop an exploration guide towards further discovery of gold resources in the greater Kirk Range area (and elsewhere in south-central Malawi)

I was responsible for the writing of this manuscript as well as the creation of all the figures. Field data collection was mainly done by me and all the subsubsequent data analyses were

conducted by me under the supervision of Dr Bjorn von der Heyden. Prof Alex Kisters provided critical review of the manuscript during the final stages of revision.

Primary gold mineralisation in the Lisungwe Valley area, Kirk Range, southern Malawi

Joshua Chisambi[1,2] and Bjorn von der Heyden[1]

[1]Department of Earth Sciences, Stellenbosch University, South Africa.

[2]Department of Mining Engineering, University of Malawi, the Polytechnic

Email: jjchisambi@gmail.com ; bvon@sun.ac.za

Abstract

A conspicuous paucity in gold resources in Malawi's mineral inventory may be partially attributed to a general low resolution in the knowledge of Malawi's geology, coupled with historical under-exploration for this important economic commodity. To address this knowledge gap, the present study focusses on developing a regional, local and microscopic understanding of the characteristics of gold occurrences in the mineralized Little Chisumbwiti river valley, located in the Kirk Range region which forms part of Southern Irumide mobile belt in southern Malawi. Regional scale interpretations are afforded by in-depth investigation of airborne geophysical data, which are then supported by ground geological mapping and by microscopic observations using optical and electron microscopy, and X-ray computed tomography (XCT). Structural mapping and regional geophysics indicate that the area has been affected by at least two periods of deformation (D1-D2). The D1 deformation event is characterized by NW–SE directed crustal shortening (tentatively associated with the Southern Irumide orogeny) which produced NE–SW structures. Gold mineralisation in the Little Chisumbwiti river valley is hosted in NE-SW trending quartz--sulphide vein sets, where it occurs as flakes ranging in size between 0.24 and 4 mm. The gold is associated with a paragenetically-late pyrite-chalcopyrite-sphalerite generation of sulphide precipitation, and to a lesser extent, with sericitised biotite schist wall rock. Exploration in the Kirk Range region should focus on the NE-SW structures, which represent potential conduits for fluid flow during the D1-related hypogene Au mineralisation event, however the impacts of subsequent D2 deformation must also be considered. Locally, wall rock lithology (e.g., Fe (II)-rich biotite schists) may have an additional second order control on the siting of gold mineralisation. The new insights reported in this study contribute meaningfully towards advancing the status of Malawi's regional geology and should serve as a useful resource for future exploration efforts undertaken in the Kirk Range, and in other parts of south/central Malawi occurring within the Southern Irumide tectonic block.

Keywords

Gold mineralisation, Kirk Range, quartz veins, exploration, Malawi.

1. Introduction

Despite its proximity to well-established gold fields in Tanzania (Kuehn et al., 1990), Mozambique (Westerhof et al., 2008a; Westerhof et al., 2008b) and Zambia (Fritz et al., 2013)

the gold endowment of Malawi remains relatively under-studied and is thus poorly constrained. Malawian geology is dominated by Proterozoic crystalline basement rocks (Malawian Basement Complex; Carter and Bennett, 1973), which have been affected by the Ubendian (2200 – 1800 Ma) orogeny in the north of the country (Dodson et al., 1975; Lenoir et al., 1995; Ring et al., 1997; Boven et al., 1999; De Waele et al., 2003; Vrana et al., 2004), the Irumide and South Irumide orogenies (1050 – 950 Ma) in the center and south, and the Mozambique (Pan-African: 800 -500 Ma) orogenic cycle in the south of the country (Andreoli, 1984; Kröner et al., 2001). Southern Malawi also hosts the majority of the country's reported artisanal placer gold workings (Figure 1; Hori and Tomita, 1997; Dill, 2007; British Geological Survey, 2009), yet detailed information regarding the associated primary mineralisation remains sparse. The placer gold showings, the spatial proximity and geological similarities (lithological and tectonic history) to mineralized regions in adjoining countries, and the general dearth of exploration and detailed geological mapping thus renders the south of Malawi a relatively prospective area for further gold exploration.

One area in which both placer and primary gold mineralisation have been discovered in southern Malawi is the Lisungwe River Valley in the greater Kirk Range region (Bloomfield and Garson, 1965; British Geological Survey, 2009; Mshali, 2009). It is dominated by Proterozoic to lower Paleozoic gneisses, granulites and schists, broadly classified as the Malawian Basement (Bloomfield and Garson, 1965). The area has been subjected to a regional geological survey (1934-1935; reported in Bloomfield and Garson, 1965) and several geochemical stream sediment sampling campaigns (Malunga, 1992; Hori and Tomita, 1997). These studies have suggested that the primary gold mineralisation is hosted in quartz stringer-type veins, and have indicated that the placer gold showings are regionally distributed in river catchments draining into the Lisungwe River along a ~22 km transect between Kasamba in the

south and Likudzi in the north (Bloomfield and Garson, 1965). The highest placer gold grades are found in the Little Chisumbwiti River valley, a tributary of the main Lisungwe River where gold has previously been mined from the Breeze's and Phalula Mines (Figure 2; British Geological Survey, 2009). These studies, however, do not report the detailed geology of the area, nor do they provide any details as to the controls and characteristics of the primary gold mineralisation.

The present study seeks to better understand the characteristics and controls of gold mineralisation in the greater Kirk Range area by using the Little Chisumbwiti river valley as a case study. Specifically, we utilize a combination of detailed field mapping, airborne geophysics, and micro-analytical techniques to describe the mineralisation, both its regional setting and its local controls. The results provide constraints on the gold mineralisation in the area, also with the aim to guide future exploration efforts, thereby increasing the prospectivity for southern Malawi's hitherto poorly understood gold resources.

Table 1: Summary of the regional tectono-metamorphic history of the Malawian geology

Deformation event	Geochronology Date/ Peak metamorphism	Orientation of fabric	Metamorphic grade	Area affected in Malawi	References
Ubendian	2200 – 1800 Ma	NW-SE	Granulite facies	Northern Malawi	De Waele and Mapani (2002); Lenoir (1995); Ring et al., (1997).
Irumide	1050-950 Ma	NE-SW	Greenschist to amphibolite facies	Central Malawi	De Waele and Mapani (2002); Lenoir (1995); Ring et al., (1997)
South Irumide (including Unango and Nampula complexes)	~ 1021 ± 16 and 1004 ± 16 Ma	NE-SW	Greenschist to amphibolite facies.	Southern Malawi	Fullgraf et al., (2017); DeWaele et al., (2006); De Waele (2005); Bingen et al., (2009).
Pan African	~800–500 Ma	N-S	Amphibolite- to granulite-facies	Whole Malawi	Fullgraf et al., (2017); Bingen et al., (2009).
Kuunga	~550–480 Ma	E-W	Greenschist to amphibolite facies	Southern Malawi	Fullgraf et al., (2017); Kröner et al., (2001).
Southern Malawi rifting	~330–180 Ma.	NE-SW NNE-SSW	N/A	Southern Malawi	Grantham et al., (2008); Johnson et al., (2005); Castaing (1991);Briden and Mcclelland (1993); Boyd et al., (2010); Thomas et al., (2014).

2. Regional geology

Malawi has a complex geological history (Table 1) and is dominated by lithologies and structures related to the formation of three major orogenic belts, viz. the Ubendian Belt (2200-1800 Ma), the Irumide Belt (1050-950 Ma), and the Mozambique Belt (800-500 Ma) (De Waele and Mapani, 2002; Lenoir, 1995; Ring et al., 1997). The Ubendian orogeny marks the amalgamation of the Tanzanian Craton against the Bangweulu block (Boniface et al., 2014; McConnell, 1950), and has resulted in NW-SE trending structures, predominantly in the northern regions of Malawi (Ring et al., 1997). The younger Irumide belt trends NE-SW and stretches from Zambia through central and southern Malawi to the north of Mozambique (Ackermann, 1950; Ackermann and Forster, 1960; De Waele et al., 2006). Crustal shortening and thickening was associated with amphibolite-grade metamorphism and widespread granite magmatism and anataxis (Boyd et al., 2010; De Waele et al., 2009; Macey et al., 2010). The Irumide belt is subdivided by crustal-scale shear zones into the Irumide *sensu stricto*, the Southern Irumide, the Unango and the Nampula sub-provinces. The Nampula province was pervasively re-worked during the Late Neoproterozoic Kuunga orogeny resulting in the ENE-WSW-trending Lurio belt (Figure 1; Boyd et al., 2010; De Waele et al., 2006). The Pan African Orogeny (~800-500 Ma) formed the Mozambique Belt (De Waele et al., 2009; Ring et al., 1997), which experienced peak metamorphic conditions of 750-800°C at roughly 12-13 kbar and subsequent amphibolite facies retrogression at 550-700°C and 5-8 kbar (Sommer and Kröner, 2013). Pan African tectonism and high grade metamorphism caused significant overprinting and reactivation of older structures inherited from the Ubendian, Irumide and Kuunga orogenic episodes (Ring et al., 1997) and resulted in the development of predominantly N-S trending structures and fabrics.

This regional scale understanding of the Malawian basement geology is derived largely from detailed work conducted in the east of Zambia (Karmakar and Schenk, 2016) and in the north

of Mozambique (Bingen et al., 2009; Boyd et al., 2010) with only a limited body of work focused specifically on Malawian rocks (e.g., Andreoli, 1984; Bloomfield and Garson, 1965; Kröner and Collins, 2001). Importantly, Kröner and Collins (2001) have shown that the high-grade gneiss assemblage of southern Malawi, covering the Kirk Range study area, reached peak metamorphic conditions at 900 ± 70°C and 9.5 ± 1.5 kbar during the Pan-African overprint. The region is bounded by the Mwambeshi shear to north, Sanangoè shear belt to the south and Lurio shear belt to the east and thus coincides with a continuation of the Southern Irumide Belt (Figure 1) which represents a tectonised edge of the Niassa Craton (e.g., Andreoli, 1984; Kröner and Collins, 2001). Malawi's recent geological history is dominated by carbonatite magmatism associated with the East African rift system, giving rise to the Chilwa Alkaline Province which includes the Kangankunde intrusion in the Kirk Range located just north of the study area (Broom, 2017; Duraiswami and Shaikh, 2014).

3. Methods

Based on the presence of historical mine sites (Figure 2), the proximity to the Manondo-Choma thrust as an important first-order structure, and prominent gold geochemical anomalies reported by earlier workers (Hori and Tomita, 1997), we selected the Little Chisumbwiti river valley (~15.31°E; 34.85°S) for detailed geological mapping and sampling. Regional-scale data are derived from a geophysical dataset collected by Sander Geophysics Limited (2013). The geophysical data were ground-truthed through field work in the area in order to integrate the mineralisation with the regional geology. Thin sections and X-ray computed tomography (XCT) were used to characterize the ore- and alteration mineralogy and textural characteristics of the mineralisation**.**

3.1. Airborne Geophysics

Between 2013 and 2014, a high-resolution geophysical survey was conducted by Sander Geophysics Limited (SGL) under the auspices of the World Bank's Mining Governance and Growth Support Project (MGGSP) in Malawi. Airborne geophysical data were collected over the entire country using a 250-meter line spacing and 60-meter ground clearance. The collected data included magnetic anomaly measurements and gamma-ray spectrometric measurements of the potassium (K), thorium (Th) and uranium (U) signals (Sander Geophysics, 2013). All geophysical data were subsequently processed using Geosoft Oasis Montaj software (Geosoft, 2008). Specifically, the original data lines were gridded using a minimum curvature gridding method (Briggs, 1974) and a 50 m grid cell size to provide smoothed spatial continuity across the area of interest.

Magnetic anomalies usually have a complex shape due to the variation of the Earth's magnetic field at the point of measurement. To resolve this, reduction of the total magnetic field to the pole was applied using the reduction to the pole (RTP) algorithm (Kis, 1990). This reduction positions the anomalies more directly over their causative bodies, and hence makes interpretation easier (Li, 2008). The resulting grids were further filtered to enhance any high intensity magnetic bodies and structures. The applied filters included the analytical signal, first vertical derivative (Beckett, 2003; Cooper, 2012; Cooper and Liu, 2011) and tilt derivative (MacLeod and Jones, 1993). The analytical signal was used to delineate the edges of the magnetic anomalies**.** Tilt- and first vertical derivatives enhance linear geological features, such as faults, dykes and provided an excellent base for the structural interpretation (e.g., AlSaud, 2008). Geological features were then extracted from the processed images using visual image interpretation techniques (Drury, 2001).

Single band (K, Th and U) pseudo-colour images derived from the radiometric data were used to confirm the mapped surface geology and structures (Wilford, 1997). Additionally, Th/K ratio maps were generated in Oasis Montage using the grid math algorithm to enhance subtle features which may not have been obvious in the original grids (Tourliere et al., 2003).

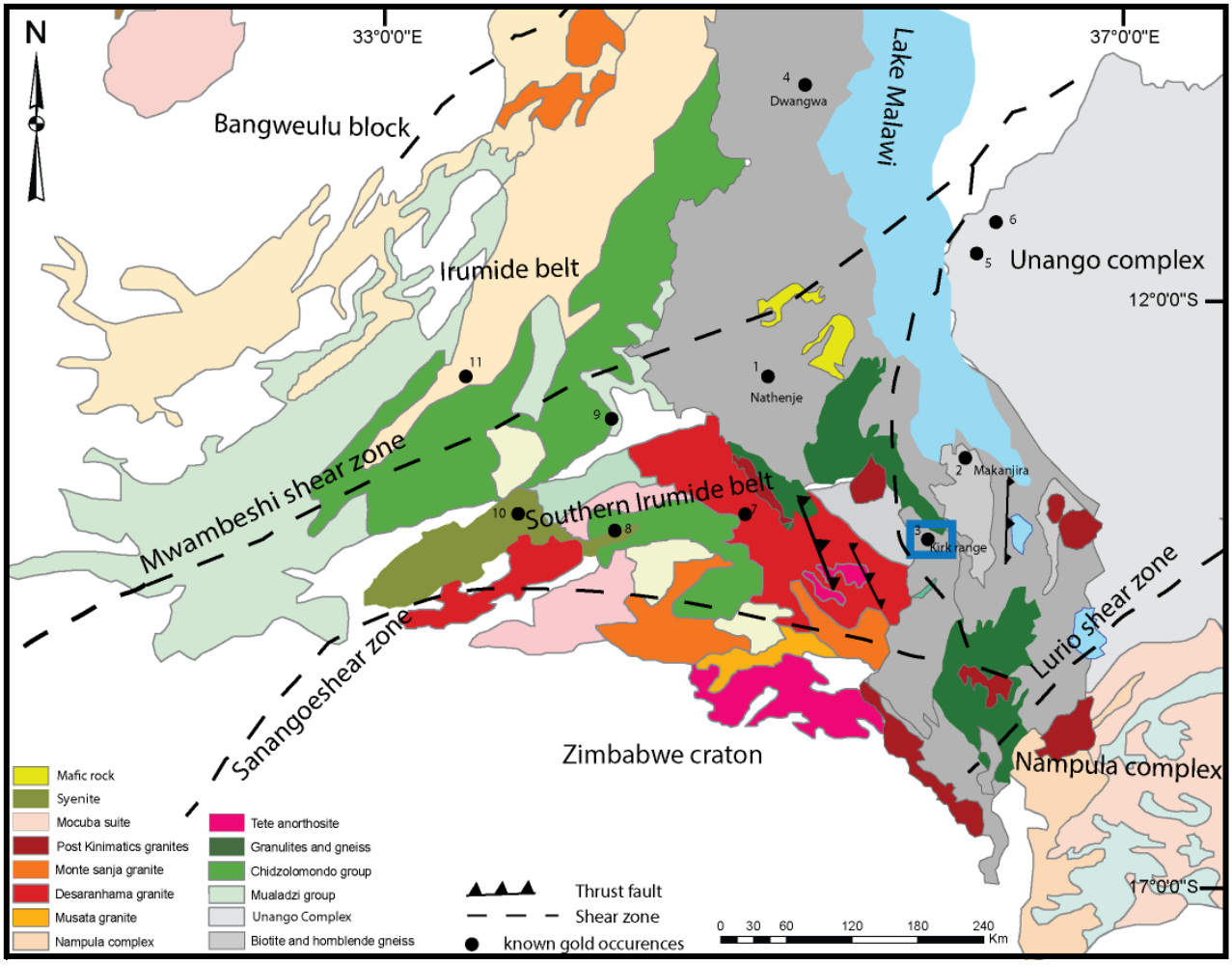

Figure 1 : *Regional geology for southern Malawi and surrounding countries (after Andreoli, 1984; Bjerkgard et al., 2009; Boyd et al., 2010; Karmakar and Schenk, 2016; Macey et al., 2010). The location of the study area is indicated by the blue rectangle and the locations of known and mined gold deposits are indicated by the black circles. These include Malawian placer gold workings ([1]Nathenje, [2]Makanjira, [3]Kirkrange and [4]Dwangwa), and gold workings in adjacent countries: [5,6]Niassa gold belt, [7]Kabwe, [8]Rufunsa, [9]Kanyemba, [10]Zambezi and [11]Mumbwa (Bjerkgard et al., 2009; Westerhof et al., 2008).*

3.2. Field mapping of the Manondo-Choma- Lisungwe Valley area

The geophysical results were ground-truthed during two mapping and sampling campaigns in December 2016 and 2017 in the Little Chisumbwiti Valley and its immediate surrounds (Figure 2). The 10 km^2 area spans the latitudes 15.30°S to 15.31°S and the longitudes 34.82° E to 34.85° E and is moderately vegetated. Major lithological units were sampled for subsequent thin and thick section mineralogical analyses using a Nikon Eclipse E 200 polarizing microscope in reflected and transmitted light.

3.2.1. Core sample selection

Additionally, core segments sampled from 35-mm diameter drill cores (JJ-01: 100.20–100.50 m depth; JJ-02: 60-63 m depth) extracted from the Breeze's and Phalula mine areas (coordinates 15.31721°S, 34.83958°E and 15.30666°S, 34.84301°E), which were obtained from the Geological Survey Department of Malawi, were used to further characterize the mineralogy and distribution of gold. Although representing a limited dataset, these two drill holes represent the only subsurface geological material available to the authors for in-depth geological investigation. The final depths for JJ-01 and JJ-02 were 252.98 m and 288.64 m respectively, and the sampled intersections were selected based on the presence of quartz veining.

3.3. Petrography and textures of mineralized lithologies

Detailed mineralogical and textural evaluations of lithologies in the study area were conducted using a range of petrographic, electron microscopy and X-ray computed tomography (XCT) techniques. These techniques were applied specifically to mineralized core intersections in order to better understand the sub-millimeter controls on the distribution, textures and

parageneses of the gold occurrence within quartz veins. Two-dimensional observations were afforded by reflected and transmitted light petrography using a Nikon Eclipse E 200 microscope and by scanning electron microscopy (SEM). Although 2D imaging provides useful insights, three-dimensional observations provide a much more holistic and comprehensive understanding of mineralisation textures (e.g., Sayab et al., 2016). We thus applied high resolution X-ray computed tomography to drilled core samples to evaluate the distribution and associations of gold with sulphide minerals in three-dimensional space.

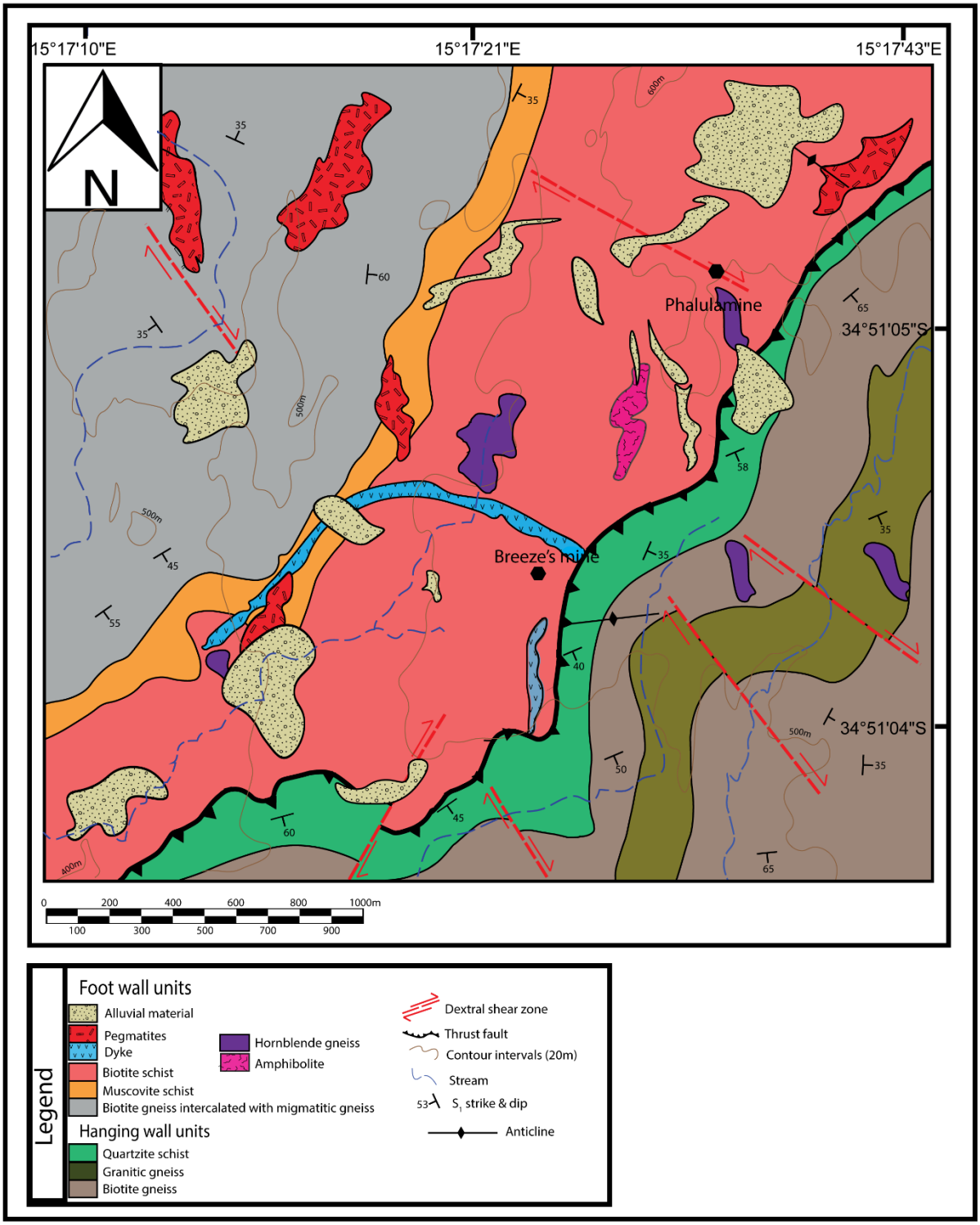

Figure 2: *Lithological map of the Little Chisumbwiti River valley indicating the location of the Breeze's and Phalula historical mine sites. Artisanal mining currently takes place in the river channels indicated.*

3.3.1. X-ray Computed Tomography (XCT)

The core samples were scanned using the Electric Phoenix VTomeX L240 Micro Computed Tomography Scanner system at the Central Analytical Facility (Stellenbosch University). The scanner was set-up to 100 kV, 100 μA with image acquisitions of 500 ms, and the X-ray beam was filtered with a 0.5 mm Cu filter. The scans were performed at a 35 μm resolution and reconstructed into a 3D model using GE Datos 2.1 reconstruction package by means of a filtered back-projection algorithm, and the data were visualized and analyzed using Volume Graphics VGStudio Max 3.1 (Kaufman and Mueller, 2003).

3.3.2. Scanning Electron Microscopy (SEM)

In order to validate the results from the XCT scan and to provide additional chemical information, the prepared thick section mounts were imaged and probed using a Zeiss® EVO MA15VP Scanning Electron Microscope equipped with an Oxford Instrument® Energy Dispersive X-ray Spectroscopy (EDS) sensor (Central Analytical Facility, Stellenbosch University). Samples were mounted in resin, polished and coated with carbon to prevent localized charging and any resulting distortion or reflection of the electron beam. The SEM and EDS analyses were collected in a nitrogen atmosphere at pressures ranging between 65 Pa and 96 Pa, voltages ranging between 20 kV and 30 kV, magnifications of between 1000 and 5000 times and an 8.5 mm working distance for the EDS analyses.

4. Results

4.1. Regional structures interpreted from airborne geophysics

Aeromagnetic data allow for the identification of dominant linear trends in the greater Lisungwe Valley (Figure 3a, b). These linear features are interpreted to represent faults, dykes and deep level basement shear zones. The rose diagram in Figure 3c presents a compilation of the orientations of the linear features and underlines the prevalent NE-SW structural grain of the region. This also reflects the predominant strike of main lithological packages in the Little Chisumbwiti river valley (Figure 2). On a regional scale, the NE-SW trends of structures and lithologies can probably be ascribed to strains related to the Irumide event (Table 1, Boyd et al., 2010; De Waele et al., 2009). De Waele et al., (2008) have suggested that many of these Irumide age structures may have been reactivated during the collision of east and west Gondwana during the Pan-African Orogeny (800 – 500 Ma). A first-order structure in the region is the Manondo-Choma thrust (Figure 3a, b), which has previously been suggested as a controlling structure for Au mineralisation in the Lisungwe Valley area (British Geological Survey, 2009). Importantly, the siting of the Breeze's and Phalula mines is spatially associated with the southern termination of the SE dipping thrust.

The second-most prevalent orientation recorded in the geophysical dataset results from linear features striking in an E-W direction. This orientation is tentatively assigned to the ~550 – 480 Ma Kuunga Orogeny, which affected southern Malawi and resulted in the formation of shear zones (e.g., Lurio Shear Zone, Figure 1) and brittle faults (Table 1). The NW-SE and N-S linear components reflected in Figure 3 are minor components in the regional geology and arise largely from a dominant ring feature identified in the south east of the geophysical dataset.

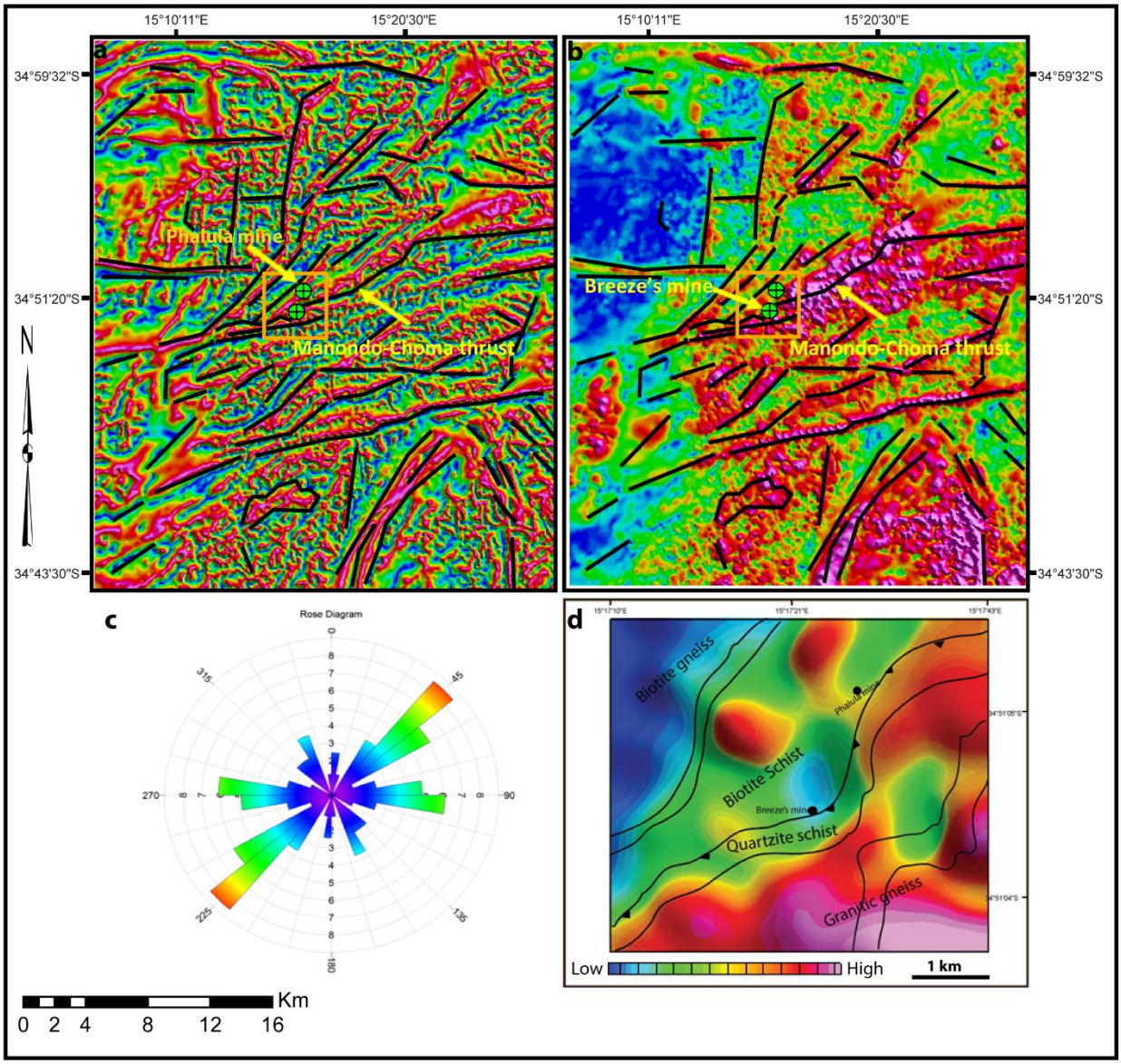

Figure 3: *Prominent lineaments representing structures (faults, fractures, shear zones and dykes) interpreted from airborne magnetic data. Deep-seated faults, fractures and shear zones are regarded as potential conduits for mineralising hydrothermal fluids. (a) Tilt derivative image, (b) Analytical signal image, and (c) Rose diagram summarising the dominant trends of structures identified in the regional area. In images (a) and (b), the yellow box is the study area and the green hatched circles reflect the locations of Breeze's and Phalula mines. (d) Th/K ratio map of the study area (yellow box), low Th/k around Breeze's mine indicates potassic alteration.*

4.2. Local geology of the Little Chisumbwiti river valley

The major lithologies in the area comprise a suite of NE trending gneissic rocks that underwent amphibolite-granulite facies metamorphism. These lithological units are characterized by polyphase deformation. The area is dominated by Manondo-Choma thrust fault that separates a moderately steep south-easterly dipping hanging-wall, from highly deformed and isoclinally-folded basement lithologies in the footwall (Figure 2).

4.2.1. Basement units in the footwall of the Manondo-Choma thrust

Biotite Schist

A biotite schist forms the immediate foot wall of Manondo-Choma thrust. This unit has an apparent thickness of approximately 1000 m. In outcrop, the biotite schist is highly weathered, complicating the correlation of the unit in the field. When fresh, the biotite schist is dark in colour, medium grained and composed of biotite, hornblende, plagioclase, variable amounts of quartz, and in places, garnet. Intrafolial, isoclinal folds are common and testify to the pervasive transposition of earlier fabrics into the SE-dipping foliation. Dismembered, boudinaged and refolded quartz blebs form relics of original quartz veins (Figure 4a). The gold mineralisation is preferentially hosted in the biotite schist, which is also the host rock of the mineralisation identified in drill cores JJ-01 and JJ-02.

Muscovite Schist

The biotite schist is underlain by a thin unit of muscovite schist, containing muscovite and variable amounts of quartz and feldspar. The muscovite schist varies considerably in appearance depending on its mica and quartz-feldspar content, from a glistening schist to a more massive, but foliated gneiss. Textures vary from granoblastic to schistose accordingly.

Biotite Gneiss

A biotite gneiss unit is developed in the north-west section of the study area. This unit is intercalated with migmatitic biotite gneiss that shows evidence of localized partial melting (Figure 4b). The gneisses are dark-brownish to dark-grey when fresh, or brownish on weathered surface. Petrographically the gneisses comprise biotite, plagioclase, quartz ± muscovite. The gneissic texture is formed by mesocratic and leucocratic bands that range from 1 cm to 5 cm in thickness (Figure 4c). The leucocratic bands are dominated by quartz and flattened feldspar whereas the mesocratic bands consist mainly of hornblende and biotite. These gneisses are highly strained and associated with a penetrative fabric defined by aligned mica and amphibole. Similar to other units of the basement rocks, the gneisses are folded into tight- to isoclinal folds and show small-scale, late stage brittle faulting (Figure 4 c, d).

Migmatitic biotite gneiss

The migmatitic biotite gneiss units are intercalated within the biotite gneiss and have been mapped as one unit with the biotite gneiss in Figure 2. These migmatitic gneiss rocks show evidence of in situ partial melting (migmatitic texture, Figure 4b). They have a NE-SW trend and form outcrops that range from 10 m to 30 m wide. The migmatitic texture is mainly defined by 5 mm to 5 cm thick leucosome and melanosome bands. The leucosomes are dominated by segregations of quartz and feldspar, whereas the melanosomes are mainly rich in biotite and/or hornblende and peritectic garnet. In places, these lithological units are folded (Figure 4b).

Mineralogically, the migmatitic gneiss is dominated by quartz, feldspar (plagioclase and K-feldspar), biotite and garnet.

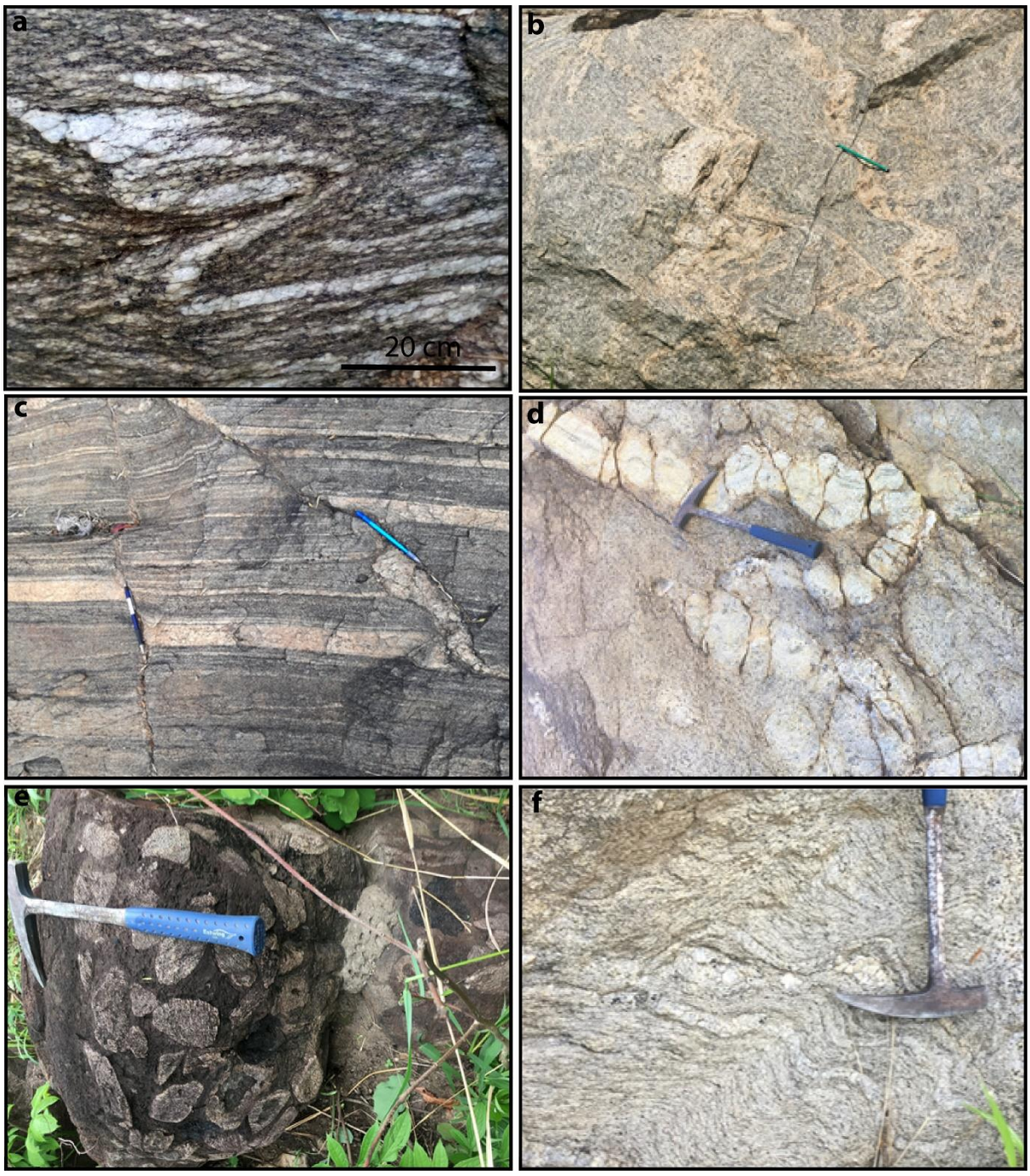

Figure 4: *Selected lithological units identified in the Little Chisumbwiti river valley. (a) Tightly folded biotite schist and foliation (S1) parallel quartz-feldspar segregations, truncated by low-angle spaced biotite foliation. The biotite schist is the main host of the gold mineralisation. (b) Migmatitic biotite gneiss with leucocratic segregations interpreted to represent partial melting of the rock. (c) Small-scale, late stage brittle faulting of banded biotite gneiss. (d) Biotite gneiss showing tight isoclinal folding. (e) Large phenocrysts in mafic dykes, some of which reflect compositional zoning. (f) Refolded (type 3) fold interference pattern in granitic gneisses, illustrating the degree of transposition (S1) in parts of the sequence.*

Amphibolites

Amphibolites were noted only in the central part of the study area. They mainly occur as lenticular, tightly folded lenses with apparent thicknesses ranging between 5 to 50 m within the biotite schist. These rocks are generally coarse grained, dark grey with a granoblastic texture and contain large distinctive flakes of biotite. Compositionally, amphibole dominate and texturally they range from medium grained equigranular- to very coarse grained.

Pegmatites

Pegmatites occur only in the footwall units. They are typically dyke-like bodies or elongated lenses with steep dips and variable orientations. They vary in size up to a few tens of meters wide and a few hundred meters long. They cut across the foliation of the gneisses and schists and show no sign of plastic deformation. Being relatively more resistant to weathering than surrounding rocks, they commonly give rise to low ridges, topped by boulders of pegmatitic material. They are largely dominated by K-feldspar and minor amounts of muscovite.

Dykes

Two dykes were mapped in the studied area and range from dioritic to gabbroic in composition. A smaller dyke is orientated N-S and has a vertical dip, whereas the larger dyke trends NE-SW and curves in response to the topographical effects on the north side of the Little Chisumbwiti river valley (Figure 2). Both dykes are characterized by a high proportion of phenocrysts, some of which are zoned exhibiting core/rim structures (Figure 4e). Chilled margins are locally observed at the contacts between the dykes and their country rocks. The dykes are the youngest intrusive unit within the footwall suite of rocks as they crosscut the isoclinally-folded basement lithologies. Both dykes terminate at the mapped thrust structure providing clues towards the relative timing of the thrust event.

4.2.2. Geological descriptions of hanging wall units

Quartzite schist

The immediate hanging wall of the Manondo-Choma thrust is made up of a quartzite schist unit. The quartzite schist occurs as a narrow concordant band in the central part of the area, forming a weathering-resistant ridge with a NE trend. The quartzite outcrops for about 3 km in length, dipping to the south-east. It is a fine to medium grained, white granular rock, with poor to moderate foliation. The rock is dominated by quartz. The quartz occurs as flattened, lenticular grains and grain aggregates within the schist.

Granitic gneisses

The quartzite schist unit is overlain by granitic gneiss. The granitic gneisses are locally deformed, gneissosity is defined by the grain-shape preferred orientation of recrystallized feldspar and quartz-feldspar aggregates (Figure 4f). The granitic gneisses are leucocratic, coarse grained and have interlocking textures. The mineral assemblage consists of quartz, k-feldspar, plagioclase and biotite.

4.3. Structural deformation in the Little Chisumbwiti valley

Lithological units are characterized by polyphase deformation. Based on field and overprinting relationships, two episodes of deformation (D1–D2) can be identified in the area.

D1 deformation

The earliest fabric that can be seen in the region is a main and penetrative, regionally SE dipping S1 foliation. Abundant isoclinal folds contained in S1 point to the pervasive transposition of any primary features into this fabric (Figure 4a). Biotite-garnet assemblages in, e.g., biotite schist units, hornblende bearing assemblages in biotite gneiss, the presence of in-situ partial melts in gneiss and the pervasive crystal-plastic deformation textures shown by

granitic gneiss suggest that the deformation fabrics occurred during amphibolite to possibly granulite facies metamorphic conditions. The D1 deformation and accompanying high-grade metamorphism also resulted in the development of compositional layering comprised of mafic and felsic mineral bands (Figure 4c). This fabric is most pronounced in the footwall of the Manondo-Choma thrust.

D2 deformation

Earlier D1 fabrics and structures have been refolded by upright F2 folds here ascribed to a D2 deformation phase. This deformation phase is characterized by a NW striking metamorphic foliation (S2) which dips NE. D2 deformation occurred in a stress field in which the entire sequence openly folded about NW-SE trending folds (Figure 2). The D2 folding event is associated with a weakly developed spaced cleavage (S2), which controls the preferred orientation of retrograde minerals such as chlorite, muscovite and minor biotite, pointing to probably mid-greenschist-facies grades of metamorphism during deformation. Based on field relations, D2 is tentatively linked to a later metamorphic event (i.e., either Kuunga or pan-African related). The D2 NW-SE fabric, however, matches neither the E-W Kuunga grain, nor the N-S Pan-African grain, and thus could be a local manifestation of either of these two events.

4.4. Quartz vein generations

In the broader region, previous workers (Bloomfield and Garson, 1965) have identified four different quartz vein generations. In the Chisumbwiti River valley, we have recognized only two generations of quartz veins, including a NE trending gold and sulphide-mineralized generation of quartz veins and N-S trending quartz veins that crosscut the foliation.

The first-generation quartz veins are milky and crystalline. They are S1 foliation-parallel quartz veins (Figure 5 a), showing NE-SW trends and SE dips and co-planar with the major structures

on the airborne geophysics and the general foliation and strike of the dominant lithologies (Figure 3). The quartz veins are up to 20 cm to 35 cm thick. They appear sheared and boudinaged in the S1 foliation plane (Figure 5a), suggesting a pre- to syn D1 timing. Quartz veins tend to be gold mineralized where they occur in the biotite schist unit. Veins within granitic gneisses and quartzites are, in contrast, barren. These sets of veins were also identified in drill core segments intersecting biotite schist and were found at 100.2–100.5 m (JJ-01) and 60–63 m (JJ-02) depth.

Second-generation quartz veins crosscut the first-generation quartz veins (Figure 5b) and have a general N-S orientation with an E dip and are associated with the D2 deformation event. These quartz veins have been deformed and often show thickness variability along strike arising from the regional deformation. The veins are pinkish in colour and show no association with sulphides or gold mineralisation.

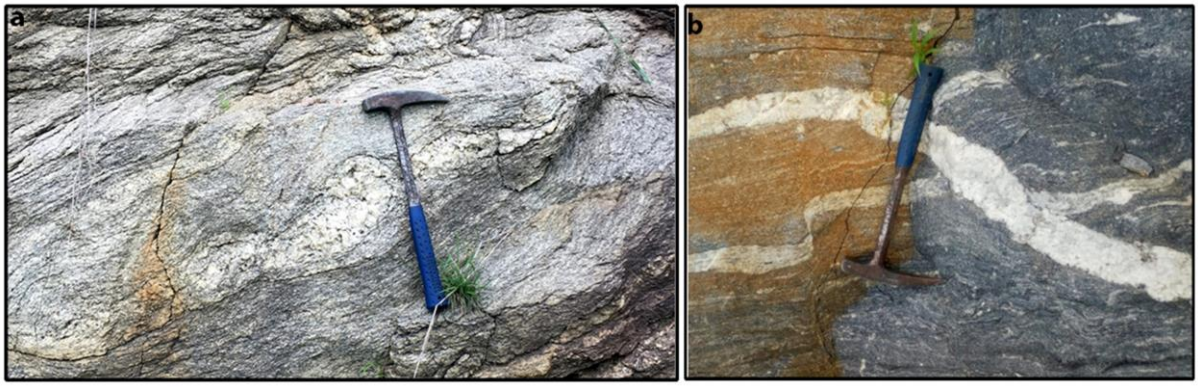

Figure 5: *Generations of quartz veins. (a) First-generation quartz vein parallel to dominant foliation which trends in a NE-SW direction. The vein is sheared and boudinaged in the S1 foliation plane, suggesting a pre- to syn D1 timing. (b) Second-generation quartz vein cross cutting first generation vein. This generation of quartz veining is barren of gold mineralisation.*

4.5. Nature of gold mineralisation in the Little Chisumbwiti valley

Quartz vein systems mineralized with economic grades of gold were previously mined at Breeze's and Phalula mines (Figure 2). From the drill core samples derived from boreholes JJ-

01 and JJ-02, we identified these economic to sub-economic grade quartz vein sets which were hosted in the biotite schist lithology. Hydrothermal wall rock alteration around the host rock is mainly associated with sericitisation and chloritization (Figure 6a) in which plagioclase is being altered to sericite. Possibly related to this wall-rock alteration, the radiometric data reveal that the Breeze's mine site is characterized by an anomalously low Th/K signature (Figure 3d), although this signature is absent at the Phalula mine site. The sulphide mineral assemblage comprises pyrite, pyrrhotite, chalcopyrite, sphalerite and gold (Figure 6b, c, e). Pyrrhotite is the earliest formed mineral in the paragenetic sequence, and shows a strong mineral stretching orientated in the direction of the shear foliation (Figure 6e). Pyrite is the dominant sulphide mineral and makes up approximately 80% of the total sulphide population. Pyrite replaces much of the earlier pyrrhotite (Figure 6e) and additionally forms a population of euhedral to subhedral discrete grains. Chalcopyrite and sphalerite are paragenetically late-stage minerals that concentrate along late fractures. Furthermore, chalcopyrite commonly develops as rims around the pre-existing pyrite minerals, whereas sphalerite forms anhedral fine-grained crystals commonly displaying "chalcopyrite disease" (Figure 6b). The gold is associated with a paragenetically-late pyrite-chalcopyrite-sphalerite generation of sulphide precipitation, and to a lesser extent, with sericitised biotite schist wall rock.

Whereas petrographic approaches can only provide mineralogical and spatial information in two dimensions, the advent of X-ray computed tomography (XCT) has enabled detailed spatial resolution of mineralogical information in three dimensions (e.g., Kyle and Ketcham, 2015). Figure 6d illustrate the advantages of XCT towards understanding the spatial distribution of dense minerals (e.g., gold, sulphides- yellow colours) in a less dense host lithology (e.g., silicate minerals- grey colours). Sulphides form sub-vertical veinlets with preferred orientation with respect to the quartz vein and host rock. The orientation of sulphides is consistent with the regional foliation in the biotite schist host rock and the orientation of early formed

pyrrhotite (Figure 6d, e). Gold displays a high attenuation coefficient relative to the other minerals. On this basis, gold stands out as a brighter phase relative to sulphide minerals and the silicate matrix minerals when exposed to X-ray energy. Our 3D analyses and visualizations of the distributions of mineral phases show that Au at the Manondo-Choma gold prospect associates with both the sulphide veinlets and occurs within the matrix of the proximal hydrothermally altered wall rocks. Identified gold grains range in size between 0.24 mm and 4 mm (Figure 6d), where larger sized particles show a brighter colouration due to the partial-volume effect (Kyle and Ketcham, 2015). The XCT scanned images of the thin section (Figure 6f) indicate an elongated array of gold grains along the same orientation as the sulphides.

The presence and speciation of gold was validated using SEM-EDS analysis (Figure 6c). SEM results confirm that gold is present both in association with the sulphides veinlets but also as discrete flakes hosted in the sericitised wall rock.

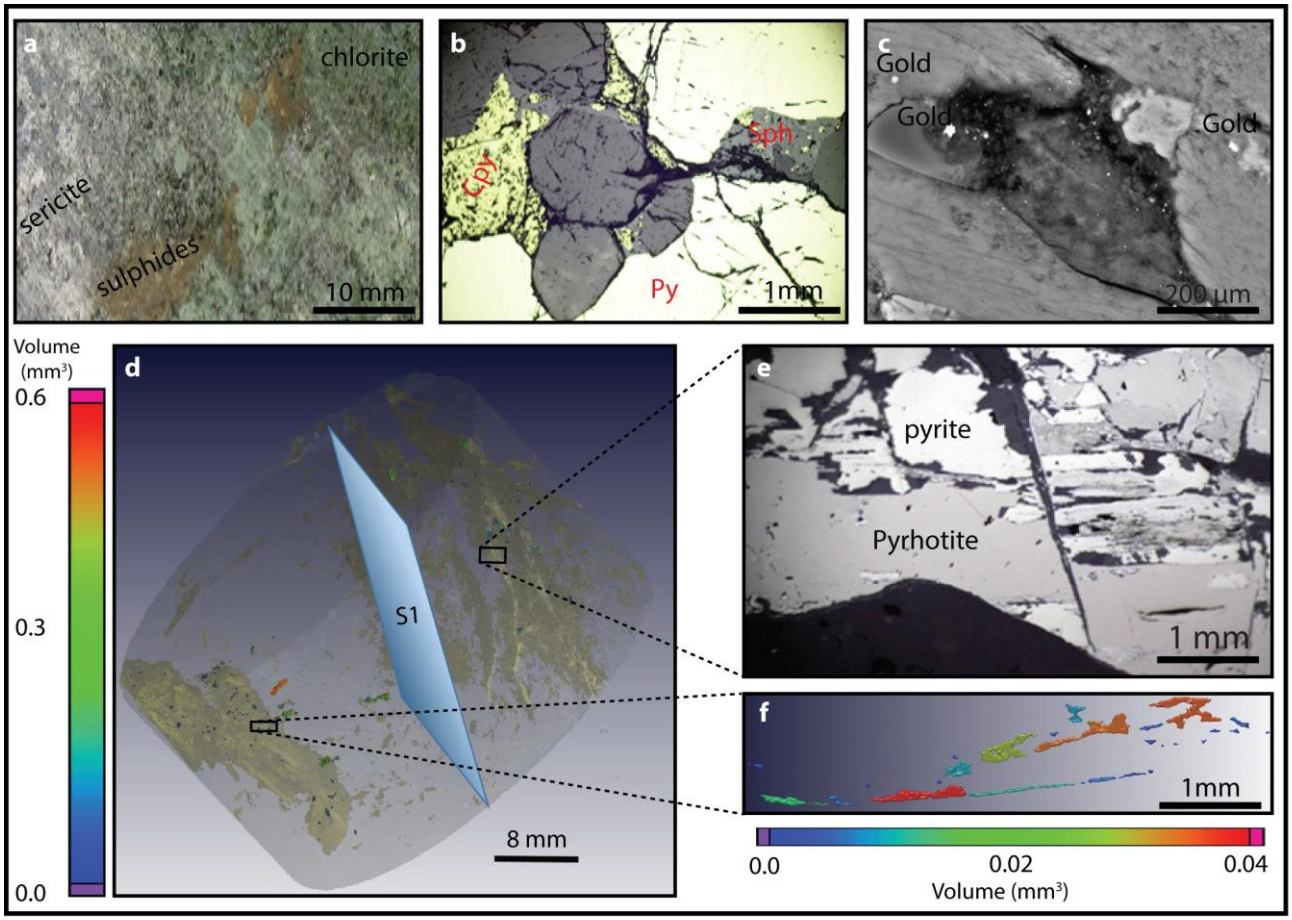

Figure 6: *Nature of gold mineralisation in the Lisungwe valley area. (a) Hydrothermal wall rock alteration (sericitisation and chloritization) observed proximal to first generation quartz veining in the biotite schist host rock. (b) Sulphide mineral assemblage comprised of pyrite, pyrrhotite, chalcopyrite and sphalerite. (c) Backscattered gold elemental map obtained from the SEM analysis of the 2D cut surface of the core. The bright spots are identified gold grains using energy dispersive spectrometry (EDS). (d) XCT image showing 3D distribution of gold in mineralized drill core sample from gold-rich hydrothermal veins. Grey colour is the silicate matrix, yellow colour indicates sulphides, other colours represent gold, distributed according to gold grain volume (warm colours = large grains, cold colours = smaller grains). Sulphide mineralisation occur in preferred orientation along the S1 foliation plane which is consistent with the regional foliation in the biotite schist host rock. (e) Reflected light micrograph of early formed pyrrhotite deformed and stretched in the NE-SW direction of shearing. A correlative approach to combining XCT with light microscopy enables that the sectioned polished block can be located according to the original XCT scan. The orientation of sulphides in XCT image is consistent with the orientation of early formed pyrrhotite. (f) XCT scanned image of the thin section made from indicated rectangle, show gold grains have been elongated/stretched in this dominant NE orientation along the foliation plane.*

5. Discussion

5.1. First insights into the structural controls on gold mineralisation in the Little Chisumbwiti river valley

Field evidence and drill drilling intersections reveal that gold mineralized veins occur primarily in the highly sheared biotite schist lithology, which has experienced localized sericitisation. The surface expression of this wall-rock alteration appears to reflect as a low Th/K signal, as detected by airborne geophysics (Figure 3d) at least at one of the two mineralized sites. The sulphide distribution in the mineralized vein system trends parallel to the wall rock foliation in a NE-SW direction and the mineralized veins trends in the same direction (Figures 5a).

Supporting micro-textural evidence suggests that a shear zone is the controlling structure for hydrothermal fluid flow and gold mineralisation in the area (Figure 6f). This is in agreement with numerous studies that have indicated a close relationship between hydrothermal fluid migration and shearing (e.g., Bedeaux et al., 2017; Cox and Ruming, 2004 and Manighetti et al., 2009). The quartz sulphide veins that we evaluated were boudinaged, exhibited rotated porphyroclasts and a reduction in grain size due to cataclasis and contained multiple generations of fluid inclusion trails. Additionally, early formed pyrrhotite has been deformed and stretched in the NE-SW direction of shearing (Figure 6e) and gold grains also appear to be elongated in this dominant orientation (Figure 6f). This is interpreted to reflect the introduction of gold during the D1 orogenic cycle. Subsequent deformation to the area during late D1, and later structural overprinting by the D2 deformation event are expected to have led to a transposition and “smearing-out” of the original mineralisation, perhaps explaining the sub-economic status of these deposits and the vast area (i.e., >22 km transect) over which low grades of placer gold are distributed.

The microstructural, computed tomography, and field mapping data all thus point towards the D1 NE-SW regional fabric having important implications for the siting of gold in the Manondo-Choma gold district. Importantly, this orientation is consistent with the deformation fabrics developed during the southern Irumide orogeny (Boyd et al., 2010; De Waele et al., 2009; Macey et al., 2010). Furthermore, this orientation shows close agreement to the gold mineralisation structures identified in goldfields in Zambia and Mozambique (Figure 1), where gold is also associated with NE shear structures in the Tete province and the Unango complex (Ring et al., 2002). Genetic relationships between these deposits may give credence to Bjerkgard and co-workers' (2009) thesis that southern African gold deposits may share provincial-scale structural relationships.

5.2. Advances towards the exploration potential for similar gold deposits in Malawi

Our detailed study of the primary mineralisation in the Little Chisumbwiti river valley of the greater Lisungwe Valley region in the Kirk Range has enabled meaningful insights that may benefit and enhance gold prospectivity, particularly in southern and central Malawi. To this end, the following findings are relevant:

1) As per standard exploration practice, the presence of placer gold deposits points unequivocally towards an up-stream source of primary or hypogene gold mineralisation. This is indeed the case for the Lisungwe Valley region, where significant gold grades reported in stream sediment assays (Hori and Tomita, 1997, Dill, 2007, British Geological Survey, 2009) have directed the drilling efforts conducted by the Geological Survey Department of Malawi and have led to the delineation of the current study area in the Little Chisumbwiti river valley. It should be

noted that anomalous gold grades have been reported in several other tributaries of the Lisungwe River (Hori and Tomita, 1997, British Geological Survey, 2009), and the prospectivity of these tributaries is further confirmed by ongoing artisanal mining operations. Furthermore, Figure 1 highlights three other sites (Dwangwa, Nathenje, Makanjira) in Malawi where the presence of artisanal mining warrants further detailed exploration efforts.

2) In the greater Lisungwe Valley area, mineralizing fluid flow is interpreted to have been directed predominantly along NE-SW trending regional structures that are tentatively associated with the southern Irumide orogenic belt. In the Little Chisumbwiti river valley, gold was introduced in the NE-SW trending shear zone during the Irumide orogeny and the NE-SW trending structures appear to be prospective for future gold exploration efforts. Importantly, second order structural (e.g., fault intersections, dilational jogs, terminal fault splays, etc.) and lithological controls (lithological competency contrasts, reactive wall rock lithologies) coincident with these NE-SW trending structures should be regarded as being especially prospective. The effects of later D2 deformation however, must also be acknowledged, since transposition of an original discrete gold ore body may explain the relatively low grades and vast area over which the associated placer gold is found. This transposition will thus negatively impact gold prospectivity and will complicate gold exploration in the Kirk Range area.

3) The mineralisation at the Breeze's mine site coincides with a localized airborne radiometric signature reflecting a strong enrichment of K relative to Th. Intense hydrothermal alteration is usually associated with K enrichment. The hydrothermal fluids responsible for mineralisation may thus have been responsible for imparting a measurable radiometric signature to the surrounding host rock through alteration mineral reactions. However, this phenomenon is not observed at the Phalula mine site

and the hypothesis should thus be further tested by ground proofing the gold potential in other areas in the Lisungwe Valley (notably where NE-SW trending structures co-occur with rocks with low Th/K radiometric signatures).

4) Our XCT and SEM results indicate that gold is present both in association with the sulphide minerals in veinlets, but also as discrete flakes hosted in the sericitised wall rock. The latter observation implies that the Fe-bearing biotite-rich wall rock may impose a second-order lithological or geochemical control on the siting of gold mineralisation. For example, Phillips and Powell (2015) have highlighted the importance of Fe-bearing minerals as sulphidation reaction sites during gold precipitation in a hydrothermal model for the Witwatersrand gold mineralisation, and Pearce and coworkers (2015) have invoked biotite breakdown as part of a reaction mechanism for gold distribution in a dolerite-hosted orogenic gold deposit. Our results do allow comment on the mechanism by which gold associates with the wall-rock, we posit that this association may prove to be a useful additional guide for future gold exploration efforts in the Kirk Range.

6. Conclusion

Our study aimed to better understand the characteristics and controls of gold mineralisation in the greater Kirk Range area, highlighting the geological and structural controls on gold mineralisation. The gold mineralisation is preferentially associated with SE dipping biotite schist lithologies that have experienced multiple generations of folding and shearing. Gold mineralisation in the Little Chisumbwiti river valley is specifically located in ductile shear structures trending in a NE-SW direction, which are conformable with the regional structural fabric and are tentatively correlated to the southern Irumide regional deformation event (D1). Subsequent structural overprinting and reactivation by later deformation (i.e., D2) is observed in the field relationships and the microstructural observations, and may negatively impact the

gold prospectivity of the broader Kirk Range area. The findings documented herein can be used to advise future gold exploration efforts targeting mineralisation hosted in Malawian geology.

Acknowledgements

The authors would like to extend their gratitude to Dr M. Mayne and especially to Prof A. Kisters for their comments which helped to strengthen the manuscript. The authors would further like to thank the editor and the two anonymous reviewers for their inputs and advice towards improving the final manuscript. Funding for the project was supported in part through grants to J. Chisambi (World Bank, Skills Development Project), and to B. von der Heyden (National Research Foundation of South Africa: Grant #106006, and additional support from DST-NRF CIMERA).

References

Ackermann, E. H., 1950. Ein neuer Faltengürtel in Nordrhodesien und seine tektonische Stellung im Afrikanischen Grundgebirge. Geologische Rundschau, 38, 24–39.

Ackermann, E. H., & Forster, A., 1960. Grundzuge der Stratigraphie und Struktur des Irumide Orogen. In: 21st International Geological Congress.

AlSaud, M. M., 2008. Structural mapping from high resolution aeromagnetic data in west central Arabian Shield, Saudi Arabia using normalized derivatives. Arabian Journal of Geosciences, 1(2), 129–136. http://doi.org/10.1007/s12517-008-0012-2

Andreoli, M., 1984. Petrochemistry,Tectonic Evolution and metasomatic Mineralisation of Mozambique belt Granulites from South Malawi and Tete (Mozambique). Precambrian Research, 25 (1984) 161--186.

Beckett, K. A., 2003. Airborne Geophysics Applied To Groundwater Modelling, In: Roach I.C. ed. 2003. Advances in Regolith, pp. 8-10. CRC LEME.

Bingen, B., Jacobs, J., Viola, G., Henderson, I. H. C., Skår, Ø., Boyd, R., Daudi, E. X. F., 2009. Geochronology of the Precambrian crust in the Mozambique belt in NE Mozambique, and implications for Gondwana assembly. Precambrian Research, 170, 231–255. http://doi.org/10.1016/j.precamres.2009.01.005

Bjerkgard, T., Stein, H. J., Bingen, B., Henderson, I. H. C., Sandstad, J. S., and Moniz, A., 2009. The Niassa Gold Belt, northern Mozambique – A segment of a continental-scale Pan-African gold-bearing structure.? Journal of African Earth Sciences, 53(1–2), 45–58. http://doi.org/10.1016/j.jafrearsci.2008.09.003

Boniface, N., Schenk, V., and Appel, P., 2014. Mesoproterozoic high-grade metamorphism in pelitic rocks of the northwestern Ubendian Belt: Implication for the extension of the

Kibaran intra-continental basins to Tanzania. Precambrian Research, 249, 215–228. http://doi.org/10.1016/j.precamres.2014.05.010

Boven, A., 1999. Timing of exhumation of a high-pressure mafic granulite terrane of the Paleoproterozoic Ubende belt (West Tanzania). Precambrian Research, 93(1), 119–137. doi:10.1016/s0301-9268(98)00101-6

Boyd, R., Nordgulen, Ø., Thomas, R. J., Bingen, B., Bjerkgård, T., Grenne, T., Jamal, D., 2010. The Geology And Geochemistry Of The East African Orogen In Northeastern Mozambique. Geological Society Of South Africa, 113, 87–129. Http://Doi.Org/10.2113/Gssajg.113.1.87

Bloomfield, K. and Garson M. S., 1965. The Geology of the Kirk Range-Lisungwe Valley Area. Bull. Geol. Surv. Mw. 17. Government printer, Zomba. 234pp

Briggs, I., 1974. Machine Contouring Using Minimum Curvature. Geophysics,Vol.39 (1), 39-48.

British Geological Survey., 2009. Mineral potential of Malawi 4. Deposits resulting from residual weathering, placer and rift-related sedimentation. Ministry Of Energy And Mines Report, Republic Of Malawi. 8pp

Broom-Fendley, S., Wall, F., Spiro, B., and Ullmann, C., 2017. Deducing the source and composition of rare earth mineralising fluids in carbonatites: insights from isotopic (C, O, 87Sr/86Sr) data from Kangankunde, Malawi. Springer. http:// doi.org/10.1007/s00410-017-1412-7

Carter, G. S. and Bennet, J. D. 1973. The Geology and Mineral Resources of Malawi. Bull. Geol. Surv. Mw., 6. Government printer, Zomba. 62pp

Cooper, G. R. J.,2012. The semi-automatic interpretation of magnetic dyke anomalies.

Computers and Geosciences, 44, 95–99. http://doi.org/10.1016/j.cageo.2012.02.016

Cooper, S. M., and Liu, T., 2011. A magnetic and gravity investigation of the Liberia Basin , West Africa. Journal of African Earth Sciences, 59(2–3), 159–167. http://doi.org/10.1016/j.jafrearsci.2010.07.006

De Waele, B., Fitzsimons, I. C. W., Tembo, F., and Mapani, B., 2009. The geochronological framework of the Irumide Belt : A prolonged crustal history along the margin of the Bangweulu Craton. American Journal of Science. http://doi.org/10.2475/02.2009.03

De Waele, B., Kampunzu, A., and Tembo, F.,2006. The Mesoproterozoic Irumide belt of Zambia. Journal of African Earth Sciences, 46, 36–70. http://doi.org/10.1016/j.jafrearsci.2006.01.018

De Waele, B., Liegeois, J., Nemchin, A. A., and Tembo, F., 2006. Isotopic and geochemical evidence of Proterozoic episodic crustal reworking within the Irumide Belt of south-central Africa, the southern metacratonic boundary of an Archaean Bangweulu Craton. Precambrian Research, 148, 225–256. http://doi.org/10.1016/j.precamres.2006.05.006

De Waele, B., and Mapani, B., 2002. Geology and correlation of the central Irumide belt. Journal of African Earth Sciences, 35, 385–397.

Dentith, M., and Mudge, S., 2014. Geophysics for the Mineral Exploration Geoscientist. Cambridge University Press. 516pp

Dickson, B. L., and Scott, K. M., 1997. Interpretation of aerial gamma-ray surveys-adding the geochemical factors. Journal of Australian Geology and Geophysics, 17(2), 187–200.

Dill, H. G., 2007. A review of mineral resources in Malawi: With special reference to aluminium variation in mineral deposits. Journal of African Earth Sciences, 47(3), 153–173, doi:10.1016/j.jafrearsci.2006.12.006

Dodson, M. H., Cavanagh, B. J., Thatcher, E. C., and Aftalion, M., 1975. Age limits for the Ubendian metamorphic episode in Northern Malawi. Geological Magazine, 112(04), 403. doi:10.1017/s0016756800046793

Drury, S., 2001. Image interpretation in Geology, 3rd ed. Nelson Thornes, Cheltenham, UK . 279pp

Duraiswami, R. A., and Shaikh, T. N., 2014. Fluid-rock interaction in the Kangankunde Carbonatite Complex, Malawi: SEM based evidence for late stage pervasive hydrothermal mineralisation. Central European Journal of Geosciences, Volume 6, Issue 4, pp 476–491.

Fritz, H., Abdelsalam, M., Ali, K. A., Bingen, B., Collins, A. S., Fowler, A. R.,and Viola, G., 2013. Orogen styles in the East African Orogen : A review of the Neoproterozoic to Cambrian tectonic evolution. Journal of African Earth Sciences, 86, 65–106. http://doi.org/10.1016/j.jafrearsci.2013.06.004

Geosoft., 2008. Oasis montaj Viewer 7.0 The core software platform for working with large volume spatial data Quick Start™ Tutorial.

Herbert, S., Woldai, T., Carranza, M., and Ruitenbeek, F. J. A. Van., 2014. Predictive mapping of prospectivity for orogenic gold in Uganda. Journal of African Earth Sciences. http://doi.org/10.1016/j.jafrearsci.2014.03.001

Hori, T., and Tomita, K., 1997. Regional Geochemical Reconnaissance of Kirk Range-Lisungwe, Malawi. Reports of the Faculty of Science, Kagoshima University, 30, 37-50. http://hdl.handle.net/10232/6222

Karmakar, S., and Schenk, V., 2016. Mesoproterozoic UHT metamorphism in the Southern Irumide Belt , Chipata , Zambia : Petrology and in-situ monazite dating Mesoproterozoic UHT metamorphism in the Southern Irumide Belt , Chipata , Zambia : Petrology and in

situ monazite dating. Precambrian Research, 275 332–356. http://doi.org/10.1016/j.precamres.2016.01.018

Kaufman, A.,and Mueller, K., 2003. Volume Visualization and Volume Graphics. Center for Visual Computing, Computer Science Department, Stony Brook University, Vi(v), 3044–3056.

Kis, K. I., 1990. Transfer properties of the reduction of magnetic anomalies to the pole and to the equator. Society of Exploration Geophysics, 55(9), 1141–1147.

Kröner, A.,and Collins, A., 2001. The East African Orogen: New Zircon and Nd Ages and Implications for Rodinia and Gondwana Supercontinent Formation and Dispersal. Gondwana Research, (2), 179–181.

Kuehn, S., Ogola, J., and Sango, P., 1990. Regional Setting and Nature of Gold Mineralisation in Tanzania and Southwest Kenya. Precambrian Research, 46, 71–82.

Kyle, and Ketcham, A., 2015. Application of high resolution X-ray computed tomography to mineral deposit origin , evaluation , and processing. Ore Geology Reviews, 65, 821–839. http://doi.org/10.1016/j.oregeorev.2014.09.034

Lenoir, J. L. et al., 1995. The Palaeoproterozoic Ubendian shear belt in Tanzania: geochronology and structure. Journal of African Earth Sciences, 19(3), 169–184.

Li, X., 2008. Magnetic reduction-to-the-pole at low latitudes: Observations and considerations. The Leading Edge, 27(8), 990–1002. http://doi.org/10.1190/1.2967550

Macey, P. H., Miller, J. A., Rowe, C. D., Grantham, G. H., Siegfried, P., Armstrong, R. A., and Bacalau, J., 2010. Geology of the Monapo Klippe , NE Mozambique and its significance for assembly of central Gondwana. Precambrian Research, 233, 259–281. http://doi.org/10.1016/j.precamres.2013.03.012

MacLeod, Jones, K., D., 1993. 3-D Analytic signal in the interpretation of total magnetic field data at low magnetic latitudes. Exploration Geophysics. (1993) **24,** 679-688.

Malunga, G., 1992. Geochemical Exploration of Gold in the Likudzi Block, Geological Survey of Malawi, unpublished report. Geological Survey of Malawi, unpublished report. 42pp

McConnell, R. B., 1950. Outline of the geology of Ufipa and Ubende. Bulletin of Geological Survey of Tanganyika. East African Standard. 62pp

Nafiz, M., and Akaryal, E., 2015. Gamma ray spectrometry for recognition of hydrothermal alteration zones related to a low sul fi dation epithermal gold mineralisation (eastern Pontides, NE Türkiye). Journal of Applied Geophysics, 122, 74–85. http://doi.org/10.1016/j.jappgeo.2015.09.003

Pearce, M. A., White, A. J. R., Fisher, L. A., Hough, R. M., and Cleverley, J. S., 2015. Gold deposition caused by carbonation of biotite during late-stage fluid flow. Lithos, 239, 114–127. http://doi.org/10.1016/j.lithos.2015.10.010

Phillips, G. N., and Powell, R., 2015. A practical classification of gold deposits, with a theoretical basis. Ore Geology Reviews, 65(P3), 568–573. http://doi.org/10.1016/j.oregeorev.2014.04.006

Ranjbar, H., Masoumi, F., and Carranza, E. J. M., 2011. Evaluation of geophysics and spaceborne multispectral data for alteration mapping in the Sar Cheshmeh mining area , Iran. International Journal of Remote Sensing, 1161. http://doi.org/10.1080/01431161003745665

Ring, U., Kröner, A., and Toulkeridis, T., 1997. Palaeoproterozoic granulite-facies meta-morphism and granitoid intrusions in the Ubendian-Usagaran Orogen of northern Malawi, east-central Africa. Precambrian Reserch., 85, 27–51.

Sander Geophysics., 2013. Data Processing Report High Resolution Airborne Magnetic and Gravity Survey : The Comprehensive Countrywide Airborne Geophysical Survey for The Government of The Republic of Malawi , The Ministry of Mining.

Sayab, M., Suuronen, J., Molnár, F., Villanova, J., Kallonen, A., Brien, H. O., and Lehtonen, M., 2016. Three-dimensional textural and quantitative analyses of orogenic gold at the nanoscale. The Geological Society of America, 44(9), 739–742. http://doi.org/10.1130/G38074.1

Sommer, H., and Kröner, A., 2013. Ultra-high temperature granulite-facies metamorphic rocks from the Mozambique belt of SW Tanzania AR. Lithos, 170–171, 117–143. http://doi.org/10.1016/j.lithos.2013.02.014

Tourliere, B., Perrin, J., Leberre, P., and Pasquet, J., 2003. Use of airborne gamma-ray spectrometry for kaolin exploration. Journal of Applied Geophysics, 53(2–3), 91–102. http://doi.org/10.1016/S0926-9851(03)00040-5

Vrána, S., Kachlík, V., Kröner, A., Marheine, D.,Seifert, A. V., Žáčˇ EK, and Babu° Rek, J. 2004. Ubendian basement and its late Mesoproterozoic and early Neoproterozoic structural and metamorphic overprint in northeastern Zambia. Journal of African Earth Sciences **38**, 1–21.

Westerhof, A. B. P., Lehtonen, M. I., Mäkitie, H., Manninen, T., Pekkala, Y., Gustafsson, B., and Tahon, A., 2008a. The Tete-Chipata belt : A new multiple terrane element from Western Mozambique and Southern Zambia. Geological Survey of Finland, Special Paper 48,145-166.

Westerhof, A. B. P., Tahon, A., Koistinen, T., Lehto, T., and Åkerman, C., 2008b. Igneous And Tectonic Setting Of The Allochthonous Tete Gabbro-Anorthosite. Geological Survey Of Finland, Special Paper 48, 191-210.

Wilford, J.R., Bierwirth, P.N., Craig M.A., 1997. Application of airborne gamma-ray spectrometry in soil/regolith mapping and applied geomorphology AGSO J. Aust. Geol. Geophys., 17 (2) (1997), pp. 201-216.

CHAPTER 4

Geochemistry, Geochronology and Metamorphic History of the Manondo - Choma Gold Prospect, Kirk Range, Southern Malawi

A presentation of the prepared research paper

This manuscript is in preparation for submission to the *Journal of African Earth Sciences*. I am the first author and Dr Bjorn von der Heyden is the co-author. The manuscript reports on the metamorphic history, zircon U–Pb dating, fluid inclusion and $\delta^{18}O$ stable isotope data for the Manondo – Choma gold prospect, southern Malawi. It also discusses the sources of the fluids and gold as well as the possible mechanisms of gold precipitation. The study contributes to a better understanding of the genetic aspects of the Manondo-Choma gold prospect and helps in characterizing its genesis and provides important insights into further exploration and mineralisation potential of the area. We have applied a combination of techniques towards fully characterising the gold occurrence and contextualising the host rocks with respect to new knowledge about the regional geology in which mineralisation is hosted. Geochronological evidence indicates that biotite schist unit that host gold mineralization experienced only Pan African metamorphism and therefore mineralization is interpreted to be at least Pan African in age. In our previous chapter we interpreted mineralization to be tentatively Irumide based on the structural orientation of the lineaments, however new evidence derived from geochronology data has allowed us to update this earlier conclusion. Our knowledge and understanding of the area has thus grown with the availability of more, novel data. Understanding of primary gold mineralisation in the Kirk Range discussed in chapter 3 is continued in this chapter. This chapter looks at the geochemistry side and how mineralisation

came into being and why it is difficult to find economic gold deposits in the Kirk Range. I was responsible for the writing of this manuscript as well as the creation of all the figures. Field data collection was mainly done by me and all the subsequent data analyses were conducted by me under the supervision of Dr Bjorn von der Heyden. The finalised manuscript will list Dr Matthew Mayne as co-author for his involvement and advice with the metamorphic geology section.

Geochemistry, Geochronology and Metamorphic History of the Manondo - Choma Gold Prospect, Kirk Range, Southern Malawi.

Joshua Chisambi[1,2] Bjorn von der Heyden[1] and Matthew Mayne[1]

[1] Department of Earth Sciences, Stellenbosch University, South Africa.

[2] Department of Mining Engineering, University of Malawi, the Polytechnic

Corresponding author jjchisambi@gmail.com

Abstract

The Manondo-Choma gold prospect is located in the southern Malawi within the Kirk Range. It is mainly hosted in gneisses and schists and is structurally controlled by the NE-SW ductile shear zones. In this study we report metamorphic history, zircon U–Pb dating of host rocks, as well as fluid inclusion and $\delta^{18}O$ stable isotope data of mineralised quartz veins for the Manondo – Choma gold prospect in order to understand the metamorphic conditions of the host rocks, origin and evolution of the hydrothermal fluids responsible for gold mineralisation and help to improve our understanding of the processes that resulted in the formation of the Manondo-Choma gold prospect. We used petrography and mineral chemistry, geochronology, PT estimates by pseudosection modelling, and microthermometry. U–Pb ages for gold bearing-schists and proximal gneisses document two distinct events: an Irumide-age period of metamorphism and a Pan African period of metamorphism. The gneisses experienced both the Irumide and Pan African events while the biotite schist experienced only the Pan African deformation. Irumide metamorphism occurred at around 1066-991 Ma and Pan African metamorphism overprinted the Irumide and occurred at around 700-485 Ma. Based on a loose PT constraint, the rocks experienced peak metamorphic conditions of around 500-600ºC and 10-15 kbars. The gold mineralisation is associated with quartz carbonate veins. Mineralization occurred in the early stages of Pan African event before peak metamorphism likely under greenschist facies conditions. Later deformation to amphibolite facies conditions of metamorphism during the prolonged Pan African event led to the transposition of the original mineralization. Gold mineralisation occurred at temperature of around 222-300°C and pressure of around 2.0–2.8 kbar. Minerals of economic interest were likely deposited by fluid immiscibility and fluid rock interaction. Oxygen isotope data indicate that ore-forming fluids at the Manondo-Choma gold prospect probably had a metamorphic source.

Keywords: *Hydrothermal fluids, gold mineralisation, Kirk Range, Manondo-Choma, Malawi*

1.0 Introduction

The Manondo-Choma gold prospect located in the Kirk Range area, southern Malawi has potential to be an important gold producing region. Placer gold is currently being mined by small-scale artisanal miners along the rivers. Gold occurs in hydrothermal quartz veins cutting through biotite schist rocks. Little geological research has been conducted in the area since the discovery of gold occurrences in the 1900s. The area was subjected to a regional geological survey (1934-1935; reported in Bloomfield and Garson, 1965) and other geochemical stream sediment sampling campaigns (Malunga, 1992; Hori and Tomita, 1997). The most recent study in the area was done by Chisambi and von der Heyden (2019) and Chisambi et al. (2020), and has shown that gold is mainly hosted in schistose metamorphic rocks. Their study further details that gold mineralisation is preferentially associated with SE dipping lithologies that have experienced multiple generations of folding and shearing. Gold mineralisation is specifically located in ductile shear structures trending in a NE-SW direction (Chisambi and von der Heyden, 2019). The Manondo-Choma thrust is proposed to be the controlling structure for gold mineralisation (British Geological Survey, 2009). These previous studies mainly focused on the geology and the controls of the primary gold mineralisation. The mechanisms of gold precipitation have not been constrained until now, largely due to a lack of detailed geochemical data for the deposit. Here we report on the metamorphic history, zircon U–Pb dating, fluid inclusion and $\delta^{18}O$ stable isotope data for the Manondo – Choma gold prospect, Kirk Range, southern Malawi. We also discuss the sources of the fluids and metals of economic interest and suggest possible ore-forming mechanisms. Our study contributes to a better understanding of the genetic aspects of the Manondo-Choma gold prospect and helps in characterizing the ore genesis, thus providing important insights into further exploration and mineralisation potential of the area.

2.0 Regional geological outline

The geology of the Kirk Range, and indeed the whole of Malawi, has not been well constrained, with the existing geological map dating back to 1965 (Bloomfield & Garson, 1965). The geology of Malawi is underlain by Precambrian to lower Paleozoic high-grade metamorphic para- and orthogneisses and schists commonly referred to as the Malawi basement complex rocks (Cater & Bennet, 1973). These rocks have undergone high-grade metamorphism and polyphase deformation (Achille & Andreoli, 2001; Cater & Bennet, 1973, Dill, 2007; Dulanya, 2017; Dulanya, Morales-simfors, & Sivertun, 2010; Hori & Tomita, 1997) and a prolonged structural and metamorphic history. They are associated with three major orogenic events (Ubendian, Irumide, and Mozambiquean) (Ring & Kronner, 2002; Sommer et al., 2003) .

The Ubendian orogeny represents the amalgamation of eastern Africa and Archean cratonic blocks/nuclei (Boniface, Schenk, & Appel, 2014; McConnell, 1950), and has resulted in NW-SE trending structures confined predominantly to the northern regions in Malawi (Ring, Kröner, & Toulkeridis, 1997). A subsequent tectono-metamorphic event (the Irumide orogeny) gave rise to the Irumide belt, which stretches from Zambia through central and southern Malawi to the north of Mozambique (Ackermann, 1950; Ackermann & Forster, 1960; De Waele, Liegeois, Nemchin, & Tembo, 2006). The main structural trend of the Irumide belt is NE-SW and is related to extensive crustal shortening during the main stage of the Irumide orogeny (Figure 1) (Boyd et al., 2010; De Waele, Fitzsimons, Tembo, & Mapani, 2009; Macey, Miller, et al., 2010). The Pan African Orogeny (~800-500 Ma) formed the Mozambique Belt (De Waele et al., 2009; Ring et al., 1997). The Pan African Orogeny (De Waele, 2003) was the last major orogenic event that shaped the overall geology of Malawi and resulted in significant overprinting of older orogenic features from the Ubendian and Irumide orogenies (Ring et al., 1997). It resulted in the development of predominantly N-S trending structures and fabrics.

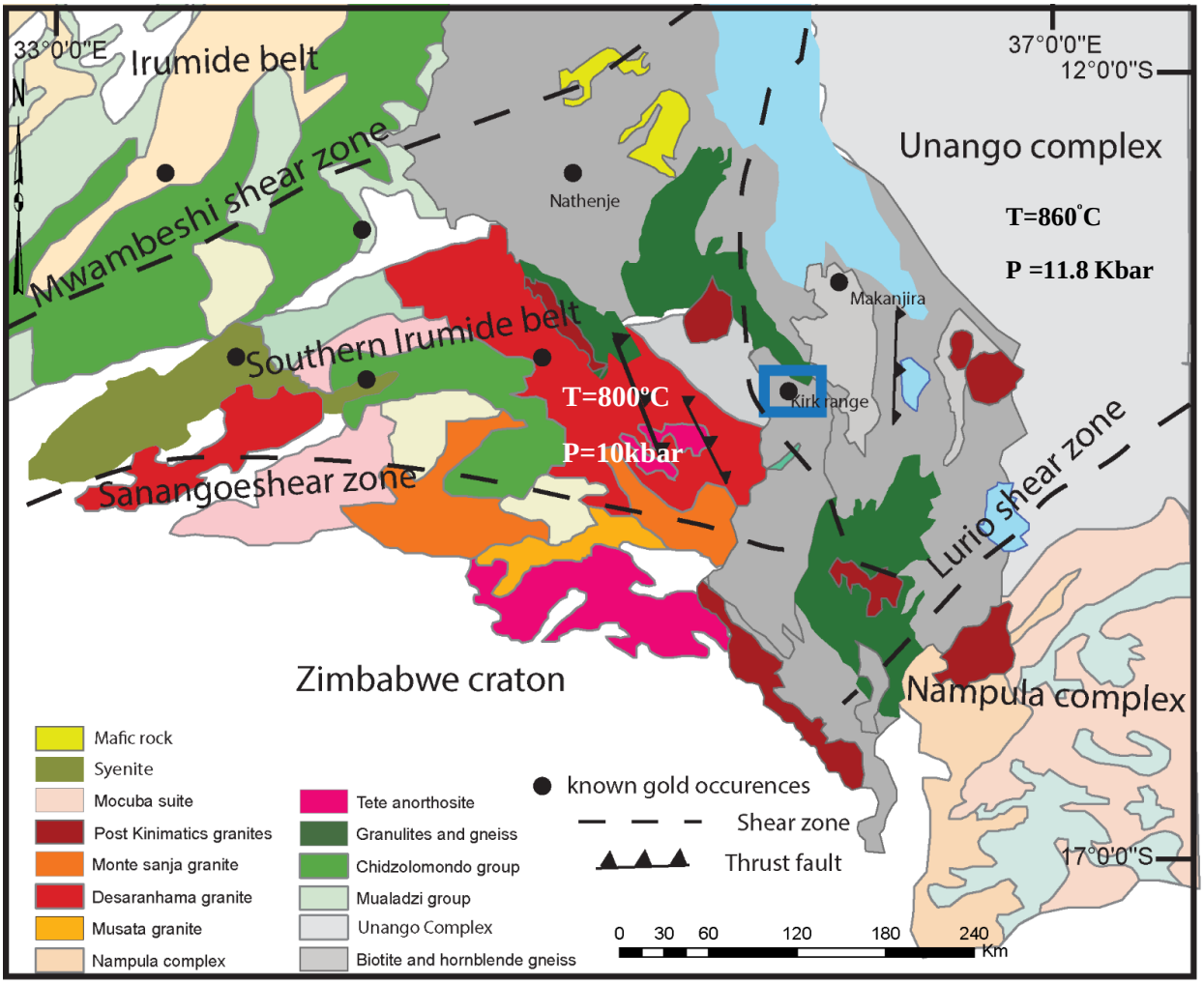

Figure 1: *Regional geology for southern Malawi and surrounding countries (after, Andreoli, 1984; Bjerkgard et al., 2009; Boyd et al., 2010; Karmakar and Schenk, 2016; Macey et al., 2010) black dots indicate the location of identified gold deposits (after, Bjerkgard et al., 2009; Westerhof et al., 2008). Our study area is indicated by the blue rectangle (modified after Chisambi and von der Heyden, 2019)*

3.0 Local Geology

The Manondo-Choma gold prospect is located in the southern part of Malawi in Balaka district Phalula area about 50 km south of Blantyre. The major lithologies in the area comprise a suite of NE trending gneissic rocks that underwent amphibolite facies metamorphism. These lithological units are characterized by polyphase deformation. The Manondo-Choma thrust fault separates a moderately steep south-easterly dipping hanging-wall, from highly deformed

and isoclinally-folded lithologies in the footwall. Biotite schists in the footwall of the Manondo-Choma thrust are the host rocks for gold mineralisation. Structurally, the Manondo-Choma gold prospect area is characterized by NE-SW trending faults and shear zones and gold mineralisation is associated with these structures (Chisambi and von der Heyden, 2019).

Mineralisation is associated with sulfide mineral assemblages dominated mainly by pyrite, pyrrhotite and chalcopyrite (Figure 2a, b) and gold is associated with pyrite. Main hydrothermal alteration assemblages are mainly associated with pyritization, sericitisation and chlorite alteration (Figure 2c, d). Pyritization is closely related to mineralisation and occurs in the sheared biotite schists (Figure 2e). Gold is present both as free Au in wall rock and in association with pyrite. (Figure 2 h, i, j).

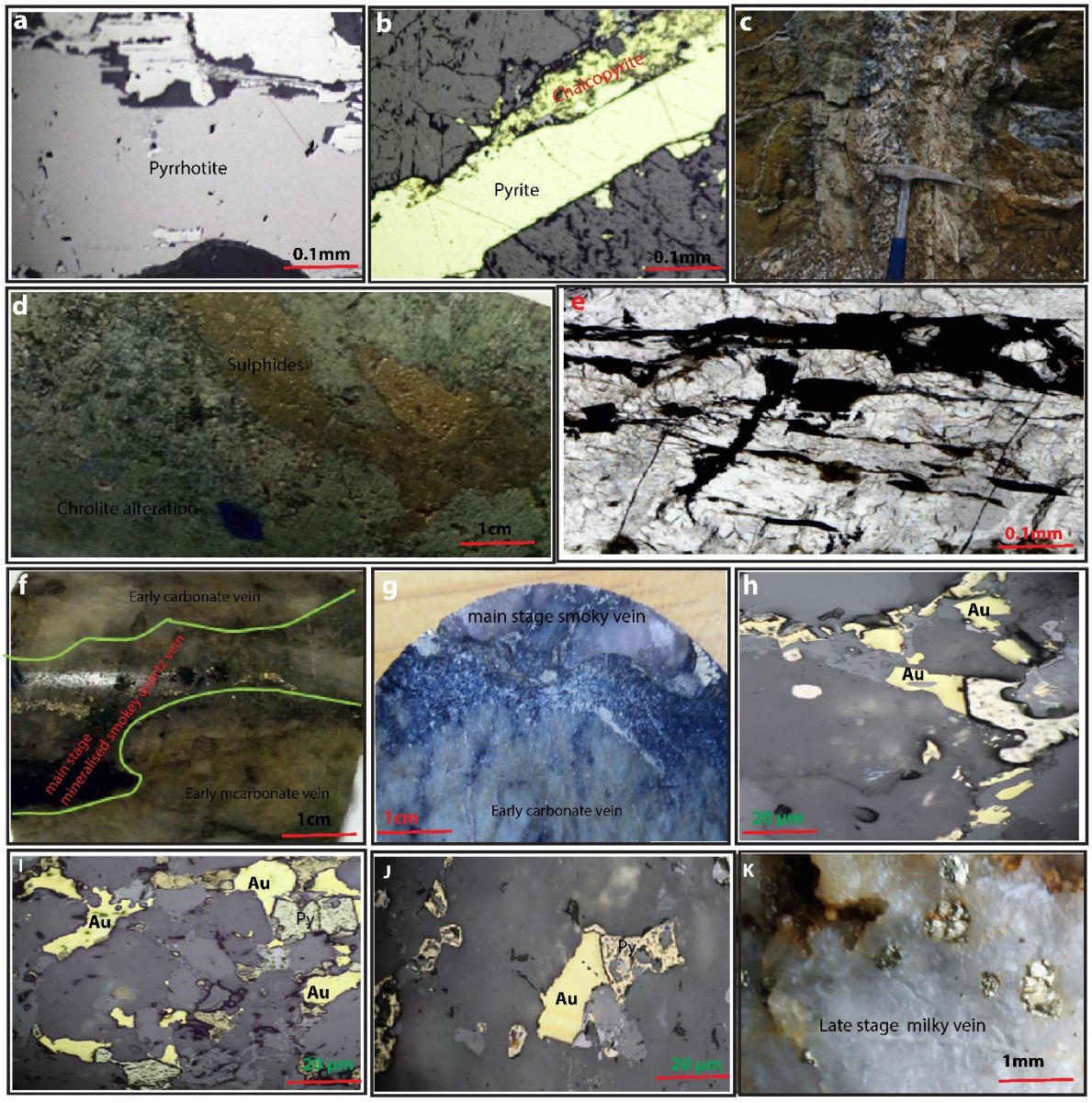

Figure 2: *(a,b) Ore minerals that were identified from Manondo – Choma gold prospect composed of pyrite, chalcopyrite, pyrrhotite and sphalerite. (c) Hydrothermal alteration consisting of sericite and muscovite. (d) Host rock with pyrite-sericite-chlorite alteration. (e) ore minerals (dark) within high strain zones, and shear bands of mineralized quartz veins. (f,g) carbonate early stage quartz vein cross cut by main stage mineralised smoky vein (h,i,j) Gold grains identified in the main stage veins. (k) Late stage milky veins*

4.0 Materials and Methods

To understand metamorphic history and gold petrogenesis we used petrography and mineral chemistry, zircon geochronology, PT estimates, fluid inclusion and stable isotope studies. Representative samples for P-T estimates and geochronology (samples (Chis 52 (biotite schist, coordinates 15.28887°S, 34.85111°E), Chis 69 (granitic gneiss, coordinates 15.29166°S, 34.86194°E) and Chis 62 (biotite gneiss, coordinates 15.28663°S, 34.85131°E)) were taken from the study area during the geological field mapping campaign. Samples that were used for P-T estimates are the same used for geochronology and are shown in Appendix 2. We selected fresh samples with minimal alteration and localities where these samples were taken are shown in Figure 3. Additionally, core segments sampled from 45-mm diameter drill cores (JJ-01: 100.20–100.50 m depth; JJ-02: 60-63 m depth) extracted from the Breeze's and Phalula mine areas (coordinates 15.31721°S, 34.83958°E and 15.30666°S, 34.84301°E), which were obtained from the Geological Survey Department of Malawi, were used for fluid inclusion and stable isotope studies. The final depths for JJ-01 and JJ-02 were 252.98 m and 288.64 m respectively, and the sampled intersections were selected based on the presence of mineralised quartz veining. Quartz veins that were sampled for fluid inclusion and stable isotope analyses are shown in Appendix 3. The drill hole localities where these samples were taken are shown in Figure 3.

4.1 Petrography, Mineral Chemistry and PT estimates

Samples for petrography and mineral chemistry were taken from the study area to understand metamorphic conditions affected by these rocks. We collected fresh samples (Chis 52 (biotite schist), Chis 69 (granitic gneiss) and Chis 62 (biotite gneiss)) containing mineral assemblages and textures suitable for characterizing metamorphic grade. From each lithology, polished thin sections were prepared at the University of Cape Town (South Africa) for petrographic and mineral chemistry studies. Petrographic studies were carried out using Nikon Eclipse E 200 polarizing microscope and mineral chemical analyses were carried out using Zeiss Evo MA 15 Scanning Electron Microscope (SEM) equipped with microprobe analyser at the Central Analytical Facility of Stellenbosch University in South Africa, under conditions of 15 kV accelerating voltage and 10 nA sample current for all minerals. The mineral chemical data are provided in Tables A1 to A5 (Appendix 1).

Furthermore in order to estimate the P–T conditions of rocks during metamorphism, we used pseudo section modelling using R crust computer modelling software developed by Mayne et al. (2016) based on bulk rock composition of major element XRF analysis for sample CHIS 52 analysed at the Central Analytical Facility, Stellenbosch University (Table 1). We used internally consistent thermodynamic dataset of Holland & Powell, (1998). The calculations were run in the NCKFMASH-TO system. H_2O values were based on loss on ignition (LOI) from XRF data.

4.2. Zircon U-Pb dating

Samples preparation and imaging

Zircons were separated from lithological units' samples Chis 52 (biotite schist), Chis 62 (biotite gneiss) and Chis 69 (granitic gneiss) from Manondo-Choma gold prospect. Zircons from each of the samples were isolated by mineral separation techniques at the Central Analytical Facilities, Stellenbosch University, making use of standard crushing, milling, panning, Frantz magnetic separation and dense liquid separation. Zircon samples were mounted in 25 mm epoxy resin discs and polished to expose the interior of the mineral grains. All zircons were cathodoluminescence (CL)-imaged prior to Laser ablation U-Pb work using a Zeiss Merlin scanning electron microscope (SEM) equipped with a CL detector at the Central Analytical Facilities, Stellenbosch University.

U-(Th)-Pb Geochronology Method

Laser ablation U-Pb data were collected at the Central Analytical Facility (Stellenbosch University) using a 193 nm wavelength ASI Resolution laser ablation system coupled to a Thermo Scientific Element 2 single collector magnetic sector field inductively coupled plasma mass spectrometer (SC-SF-ICP-MS).

At the start of each analytical session the mass spectrometer was tuned by ablating a line scan on the NIST610 glass. The torch position, lenses and gas flows were tuned while measuring ^{206}Pb, ^{238}U and $^{238}U^{16}O$ to get stable signals and high intensity on ^{206}Pb and ^{238}U, as well as low oxide rates ($^{238}U^{16}O/^{238}U < 0.3\%$). The ablated zircon material was transported from the laser cell into the ICP-MS using a continuous flow of 0.35 l/min of He gas. Signals of m/z 202, 204, 206, 207, 208, 232, 235 and 238 were acquired in electrostatic scan mode. The laser and ICP-MS software packages were synchronized in order to allow automated execution of the analysis. Each analytical session included up to ~40 measurements.

The laser sampling protocol employed a 25 µm static spot and a fluence of 2.0 J/cm^2. Before the gas blank measurement, each spot was pre-ablated by firing two laser shots to remove common Pb from the surface that may have been introduced during the sample preparation.

During each analytical session the zircon reference materials GJ-1 (Jackson et al., 2004), (Sláma et al., 2008) Plešovice and 91500 (Wiedenbeck et al., 1995) were measured between groups of 12 unknowns. Zircon GJ-1 was used as a matrix-matched primary reference material to correct for mass discrimination on measured isotope ratios in unknown samples and simultaneous correction for instrumental drift. The values used for normalization are based on ratios determined by ID-TIMS reported in Horstwood et al., (2016). Plešovice and 91500 were used as secondary reference materials to validate the results and assess the quality of the data for each analytical session.

Data reduction was performed with the software package Iolite v.3.5 (Paton et al., 2011), combined with VizualAge (Petrus & Kamber, 2012). An exponential model of laser-induced elemental fractionation (LIEF) obtained by combining the isotopic ratios of the primary reference material from the entire session is used to correct for time-dependent down-hole elemental fractionation in the unknowns, under the assumption of same fractionation behaviour in the reference material and the unknowns. After correction for LIEF and drift and normalization to the main reference material (performed in Iolite), uncertainty components for systematic errors are propagated by quadratic addition according to the recommendations of Horstwood et al. (2016).

4.3 Fluid inclusion analysis

Doubly polished sections for fluid inclusion study (about 250-300 µm thick) were made from the mineralized quartz vein samples and observed using a Nikon Eclipse E 200 petrographic microscope. Fluid inclusions were carefully observed to identify their genetic and composition

types, vapor-liquid ratios and spatial clustering. Fluid inclusion assemblages were selected based on the criteria and recommendations of Roedder (1984) and Goldstein (2003). The fluid inclusion microthermometry was conducted at the Fluid Inclusion Laboratory, University of Stellenbosch using Linkam THMSG 600 heating-freezing stage with a temperature range of -196°C to 600°C. Microthermometric measurements were carried out by initially cooling down the stage to -150°C before subsequent heating to observe phase changes. Heating rate was 10–30°C/min during the initial stages of each heating run and reduced to 0.5–1°C/min close to the phase change points.

Final ice melting temperature (*T*m-ice), melting temperature of clathrate (*T*m-cla), melting temperature of solid CO_2 (*T*m-CO_2), homogenization temperature of CO_2 liquid and vapour (*T*h-CO_2), and total homogenization temperature (*T*h), were the phase transformation parameters that were observed during microthermometry, depending on the types of FIs. Salinities (wt.% NaCl equivalents) were calculated using the equations of Bodnar, 1993 for aqueous fluid inclusions and for aqueous-carbonic fluid inclusions. Salinities were calculated from the last ice melting temperatures and clathrate (Tm-cla) using the program Aqso5e (Bakker, 2003). Densities and pressures were estimated according to microthermometric data for CO_2-H_2O-NaCl system (Bodnar, 1993).

4.4 Oxygen isotope analysis

Twelve quartz samples from the mineralized veins were selected for oxygen isotope analyses. The sample were crushed to 40–60 mesh. After crushing, quartz grains were handpicked under a binocular microscope. Analysis was done at the stable isotope laboratory, University of Cape Town, South Africa, using a Finnigan MAT 253 mass spectrometer. Oxygen was extracted from quartz by the BrF_5 method (Clayton & Mayeda, 1963). The results were normalized and reported relative to Vienna standard mean ocean water (V-SMOW) and the analytical

precisions were ±0.2‰. The oxygen isotope values of water were calculated using the fractionation formula 1000 ln αquartz–H_2O = 3.38 × 106T^{-2} − 3.40 reported by Clayton et al., (1972) where T is the mean value of the homogenization temperature of fluid inclusions from the same quartz samples.

5.0 Results

5.1 Petrography and mineral chemistry

We summarize petrographic description of the studied rock samples from the Kirk Range area southern Malawi. The mineral chemical data are given in Tables A1-A5 (Appendix 1). Most of the samples were fresh with only minor alteration.

Sample CHIS 52 Biotite schist

Sample Chis 52 was collected from isoclinally folded foot wall unit biotite schist rock (Figure 3, Appendix 2). It contains poikiloblastic garnet which contains minute inclusions of biotite, plagioclase, K-feldspar, and ilmenite within its matrix. Garnet generally shows evidence of breakdown and is replaced by feldspar and biotite which are possible retrograde minerals (Figure 4a,b). It shows the mineral assemblage garnet (Grt) – plagioclase (Pl)– biotite (Bt) – Clinopyroxene (Cpx)- quartz (Qtz) – K-feldspar (Kfs)-Chlorite (Chl)-Muscovite (Mu).

For this sample electron microprobe analyses were done on garnet (Grt), biotite (Bt), plagioclase (Pl) and Kfeldspar (Kfs). Garnets have almandine content (where X_{alm} = Fe/(Fe+Mn+Mg+Ca)) between 0.52 and 0.55, grossular content (where X_{grs} = Ca/(Fe+Mn+Mg+Ca)) from 0.38 to 0.34, pyrope content (where X_{Prp} = Mg/(Fe+Mn+Mg+Ca)) between 0.061and 0.075 and spessartine content (where Xsps = Mn/(Fe+Mn+Mg+Ca)) from 0.016 to 0.042 (Table A1). Biotite varies in X_{Mg} between ~0.77 and ~0.80, its TiO_2 varies

between 3.04 and 3.02 wt.%, respectively. K-feldspar has X_{Kfs} of 0.92 and is classified as orthoclase. Plagioclase is An28 Ab71.

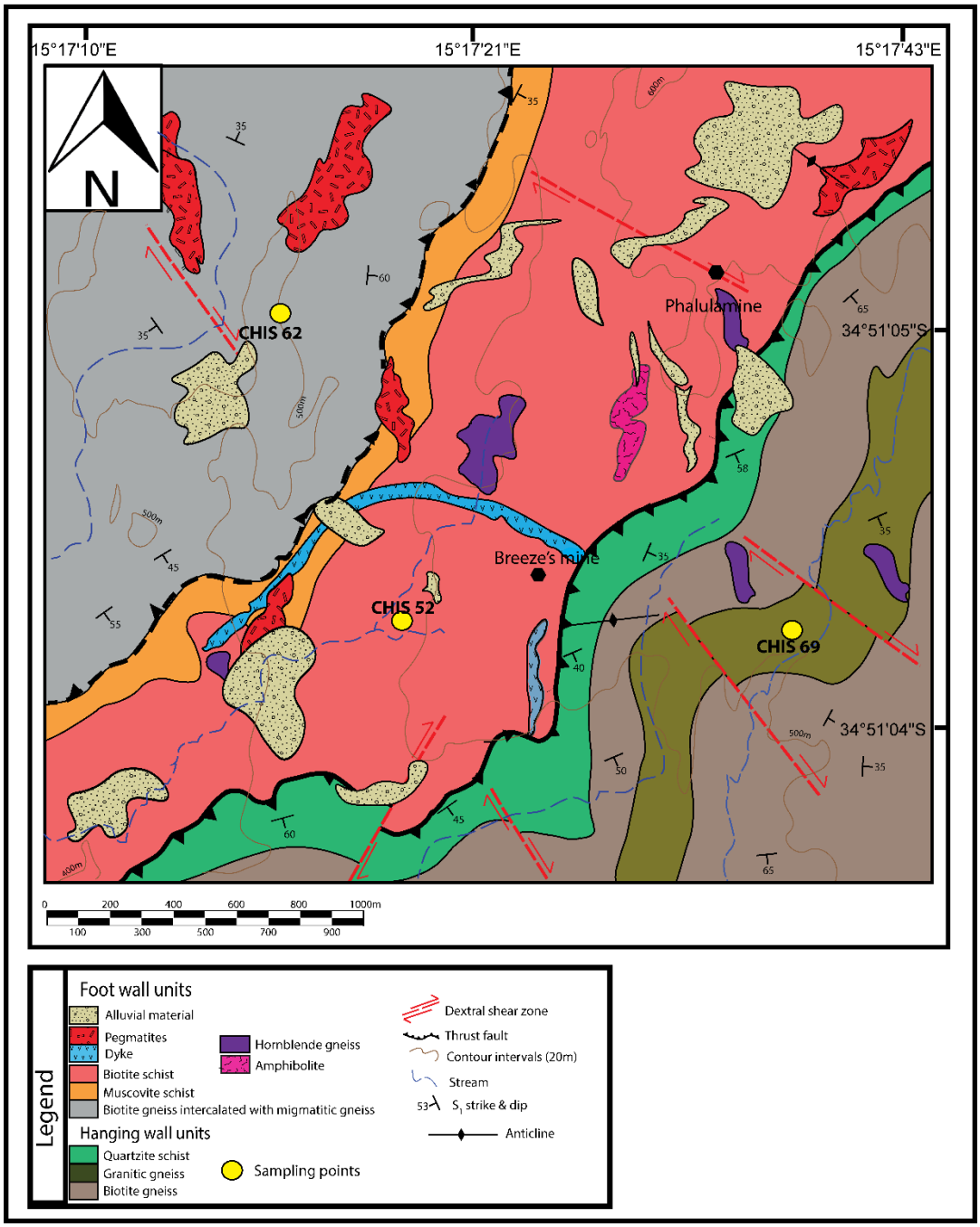

Figure 3: *Geological map of the study area, yellow dots are lithologies where samples for PT estimates and geochronology were taken black dots indicate where drilling was done. The second thrust contact is inferred based on differences in fabric, age, and rock type with footwall, and corresponding similarities with the observed hanging wall in the SE of the study area. The thrust tectonic contact was not clearly identified in the field due to the presence of overburden.*

CHIS 62 Biotite gneiss

The Sample Chis 62 was taken from biotite gneiss rock (Figure 3, Appendix 2) and it comprises of garnet (Grt), clinopyroxene (Cpx), orthopyroxene (Opx), plagioclase (Pl), amphibole (Am), biotite (Bt), K-feldspar (Kfs) and quartz (Qtz). Accessory minerals are magnetite (Mag), hematite (Hem), ilmenite (Ilm) and rutile (Rt). Garnet is euhedral and has been partially pseudomorphed by clinopyroxene + amphibole indicating retrograde metamorphic reaction (Figure 4c,d).

Electron microprobe analysis on this sample was done on garnet (Grt), clinopyroxene (Cpx), orthopyroxene (Opx), plagioclase (Pl), K-feldspar (Kfs), and amphibole (Am). Garnet show zonation from core to rim which we interpret to be retrograde exchange reactions within the analyzed garnets. X_{Mg} varies between ~0.13 (core) and ~0.10 (rim), X_{Alm} between ~0.51 (core) and ~0.56 (rim), X_{Prp} is in the range of ~0.08 (core) to ~0.07 (rim), X_{Grs} ranges between ~0.4 (core) and ~0.3(rim). X_{Sps} vary between 1.88 to 3.24 (Table A1). Orthopyroxene chemistry is $En_{48}Fs_{49}$, and clinopyroxene $En_{35}Fs_{19}$ with Mg no. 0.4. Plagioclase chemistry is $An_{28}Ab_{70}$.and

shows no systematic zoning. Biotite shows Ti up to 0.39 apfu and Mg no. ranging 0.50 -0.7. Amphibole shows Ti-content of 0.11−0.12 a.p.f.u. (Table A5).

Figure 4: *Photomicrographs of characteristic metamorphic textures from the Kirk Range. Images taken in plane polarized light. (a,b) Replacement of garnet by plagioclase and biotite, sample from biotite schist Chis 52. (c,d) Garnet is surrounded by coronas of amphibole and clinopyroxene sample from Biotite gneiss Chis 62. (e,f) Garnet is being replaced by plagioclase and amphibole/ clinopyroxene (symplectite) which indicates a decrease in pressure. This indicates that garnet was no longer stable under lower pressure and temperature, sample from granitic gneiss Chis 69*

Granitic gneiss

Sample Chis 69 was taken from hanging wall granitic gneiss rock (Figure 3, appendix 2) on the south eastern side of the study area. It is made up of garnet (Grt), clinopyroxene (Cpx), amphibole (Am), plagioclase (Pl), K-feldspar (Kfs), biotite (Bt), and quartz (Qtz), accessory minerals are ilmenite, magnetite, hematite and rutile. Garnet is being replaced by plagioclase and amphibole/clinopyroxene (symplectite) which indicates a decrease in pressure during granulite facies metamorphism (Figure 4e,f). This indicates that garnet was no longer stable under lower pressure and temperature conditions and it reacted to produce symplectite of amphibole and partly plagioclase.

We analysed garnet, clinopyroxene, plagioclase, K feldspar, amphibole and biotite in this sample for mineral chemical composition. Garnet chemical composition X_{Mg} ranges between ~0.31 (core) and ~0.11 (rim), X_{Alm} varies between ~0.58 (rim) and ~0.67 (core), X_{Prp} varies between ~0.29 (core) and ~0.07 (rim), whereas X_{Grs} varies between ~0.02 and ~0.31. The X_{Sps} ratio is very low at ~0.99 (Appendix 1, Table A1). Clinopyroxene (Cpx) has X_{Mg} of~0.03 and is $X_{En}37$, $X_{fs}16$. Plagioclase is very homogeneous, and X_{An} ranges between ~0.28 and ~0.29 (Table A4). K-feldspar is pure orthoclase, K_{fs} ranges between 0.94 and 0.95. Biotite shows X_{Mg} values of ~0.49. The TiO2 varies between 3.35 and 3.27 wt.% (Table A2). X_{Mg} in amphibole varies between ~0.57 and ~0.58 and does not show any systematic core-rim relationship (Table A5).

Table 1**:** Major XRF data for sample CHIS 52

Element	%
Al2O3	12.96
CaO	6.47
Cr2O3	0.04
Fe2O3	6.91
K2O	8.02
MgO	7.98
MnO	0.09
Na2O	0.48
P2O5	1.83
SiO2	51.60
TiO2	1.21
L.O.I.	1.45
Sum	99.04

5.2 Pressure temperature estimates

Geothermobarometric studies on the above high-grade rocks from the study area were undertaken in order to estimate the P–T conditions of rocks during metamorphism. We used pseudosection modelling for PT estimates using R crust computer modelling software (Mayne et al., 2016), based on bulk rock composition of major element XRF analysis for sample Chis 52 (Table 1).

The calculated pseudo section for sample Chis 52 with mineral assemblage garnet (Grt) – plagioclase (Pl)– biotite (Bt) – Clinopyroxene (Cpx)- quartz (Qtz) – K-feldspar (Kfs)-Chlorite (Chl)-Muscovite (Mu) is shown in figure 5 and is characterized by stability of clinopyroxene, H_2O and ilmenite over the whole investigated *P-T* range (4–15 kbar, 500–975°C). Phase boundaries of the calculated pseudo section are steep after 600°C, suggesting that reactions in this zone are generally sensitive to temperature. Garnet is introduced and becomes stable above 10 kbars. From 500°C, and pressure below 10 kbars, as temperature increases, sphene is consumed, biotite becomes stable. Between approximately 620°C and 690°C, epidote is consumed, and plagioclase is introduced while biotite and Kfs and quartz become stable. With

increasing temperature, the rock reaches the solidus and melts between 720°C and 875°C. Garnet is introduced and becomes stable at high pressures (above 10 kbar) and temperatures between 500°C and 600°C. At lower pressures, there is no mica and at high temperatures there is no garnet. The peak PT conditions are constrained using the mineral stability field in the pseudosection diagram (Figure 5) which matches our observed mineral assemblage. Peak P-T conditions are constrained to be around 500-600°C at 10-15 kbar (orange field in Figure 5).

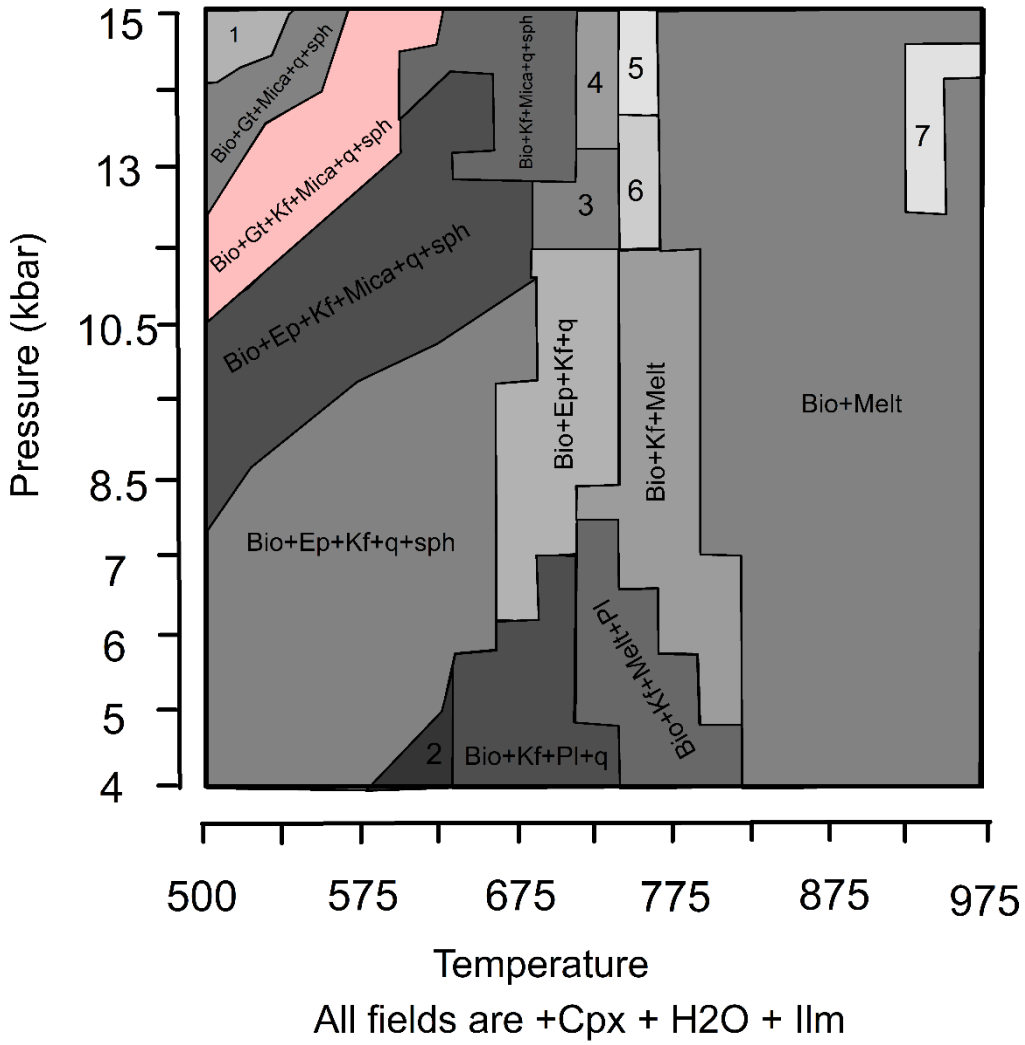

Figure 5: *Results of pseudo section modelling for sample CHIS 52 1= Gt+Mica+q+sph, 2 = Bio+Kf+Pl+q+sph 3 = Bio+Ep+Kf+Mica+q 4 = Bio+Kf+Mica+q 5 = Bio+Kf+Melt+Mica 6 = Bio+Ep+Kf+Melt 7= Bio+Bio_1+Melt.*

5.3 Zircon U–Pb geochronology

Zircon grains from foot wall sample Chis 52 (biotite schist) are translucent, colourless to light brownish prismatic and elongated in shape and have slight rounding at their terminations that we ascribe to metamorphic 'corrosion', i.e. partial zircon dissolution and recrystallization during amphibolite-facies metamorphism (Hoppe, 1966; Kröner et al., 1994; Silver, 1969). They have grain lengths of 50-200 μm. The zircon grains have moderate CL response and preserve banded zoning. CL images of representative grains are shown in Figure 6a, together with analysed spots and U–Pb ages. A total of 41 measurements were taken on this sample, and the results of zircon U–Pb concordia diagram is given in Figure 7a. Zircons from this biotite schist sample range in age from 742 ± 43 Ma to 567 ±41 Ma. Th/U ratios range from 0.09 to 1.29. All zircon spots have Th/U ratios < 1. Twenty-five analyses are concordant with a 207Pb/206Pb and have a weighted average age of 599±31 (MSWD=0.025). These zircons yielded an upper intercept age of 620±8 Ma and a lower intercept age of 520±22 Ma with (MSWD 0.66) which we consider to be the age of Pan African event.

The second sample Chis 69 is a hanging wall granitic gneiss. Zircon extracted from this sample are rounded and slightly prismatic (Figure 6c). The colour ranges from dark grey brown to light brown. The rounding may be due to dissolution and recrystallization (Hoskin & Black, 2000), probably caused by high-temperature metamorphism, a feature found for zircon in many high-grade terranes (Kröner et al., 1997). CL images reveal a well-developed oscillatory zoning, and there are grains with a core and a metamorphic rim. Thus, these zircons are typical of magmatic growth with subsequent metamorphic overgrowth. Forty-one measurements were taken on this sample. CL images of representative grains are shown in Figure 6c, together with analysed spots and U–Pb ages. Zircons from this granitic gneiss sample range in age from 1129 ± 24 Ma to 556 ±63 Ma. Th/U ratios range from 0.02 to 4.96. All analysed spots have Th/U ratios >1. Twelve analyses are concordant with a 207Pb/206Pb and have a weighted average age of

1004±84 (MSWD=2.0. The results of zircon U–Pb concordia diagram is given in Figure 7b, and yielded an upper intercept age of 1085 ± 28 Ma which we interpret to approximate the time of emplacement of the magma that formed the igneous precursor of the granitic gneiss and a lower intercept age of 485 ± 53 Ma (MSWD 3.2) which we consider to be the age of the Pan African metamorphic over-printing event.

The third sample is a biotite–gneiss (Chis 62) collected in the north-west part of the study area (Figure 3). Zircons extracted from this sample are rounded near-spherical grains that are clearly of metamorphic origin. Zircon crystals show a core–rim structure with a thick metamorphic rim. CL images of representative grains are shown in Figure 6b, together with analysed spots and U–Pb ages. A total of 36 measurements were taken on this sample. Zircons from biotite gneiss sample range in age from 1118 ± 26 Ma to 548 ±26 Ma. Th/U ratios range from 0.00 to 1.51. They have Th/U ratios <1. Seven analyses are concordant with a 207Pb/206Pb and have a weighted average age of 595±96 Ma (MSWD=1.7). Zircon U–Pb concordia diagram is given in Figure 7c and yielded an upper intercept age of 1103 ± 45 Ma which we interpret to approximate the time of emplacement of the magma that formed the protolith of the biotite gneiss and lower intercept age of 513 ± 22 Ma which we consider to be the age of the Pan African metamorphic event.

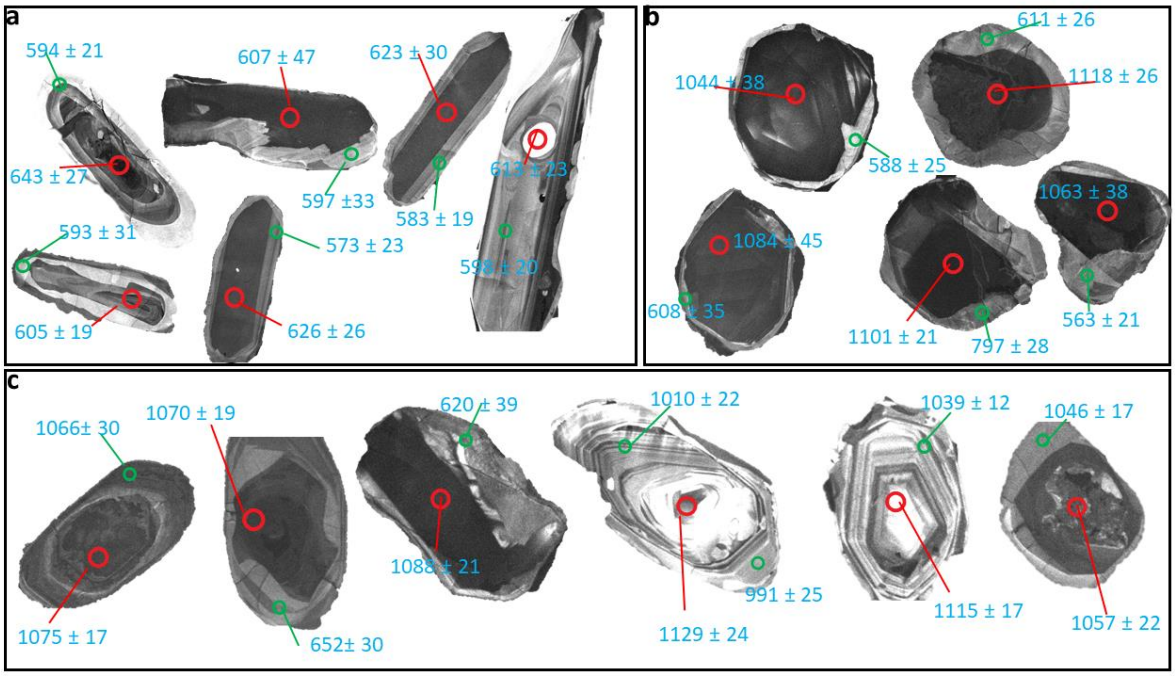

Figure 6: *CL images of representative zircon grains with analysed spots and U–Pb ages from Manondo-choma gold prospect. (a) zircon grains from sample Chis 52 (biotite schist) (b) zircon grains from sample Chis 62(biotite gneiss) and (c) zircon grains from sample Chis 69(granitic gneiss)*

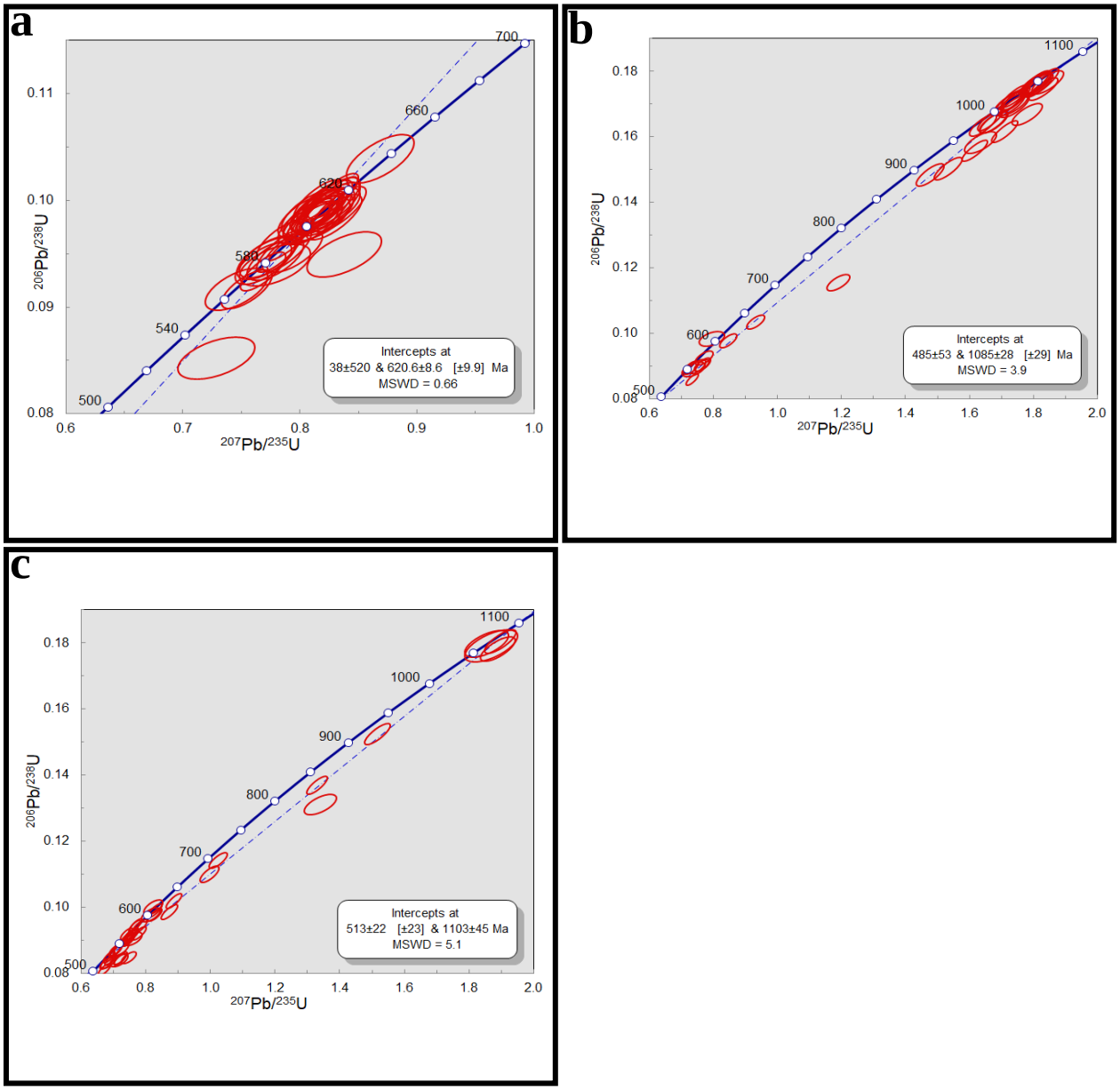

Figure 7: *Concordia diagrams for analysed zircon ages from Manondo-choma gold prospect(a) Concordia diagram for sample Chis 52 (biotite schist) (b) Concordia diagram for sample Chis 69 (granitic gneiss) (c) Concordia diagram for sample chis 62 (biotite gneiss)*

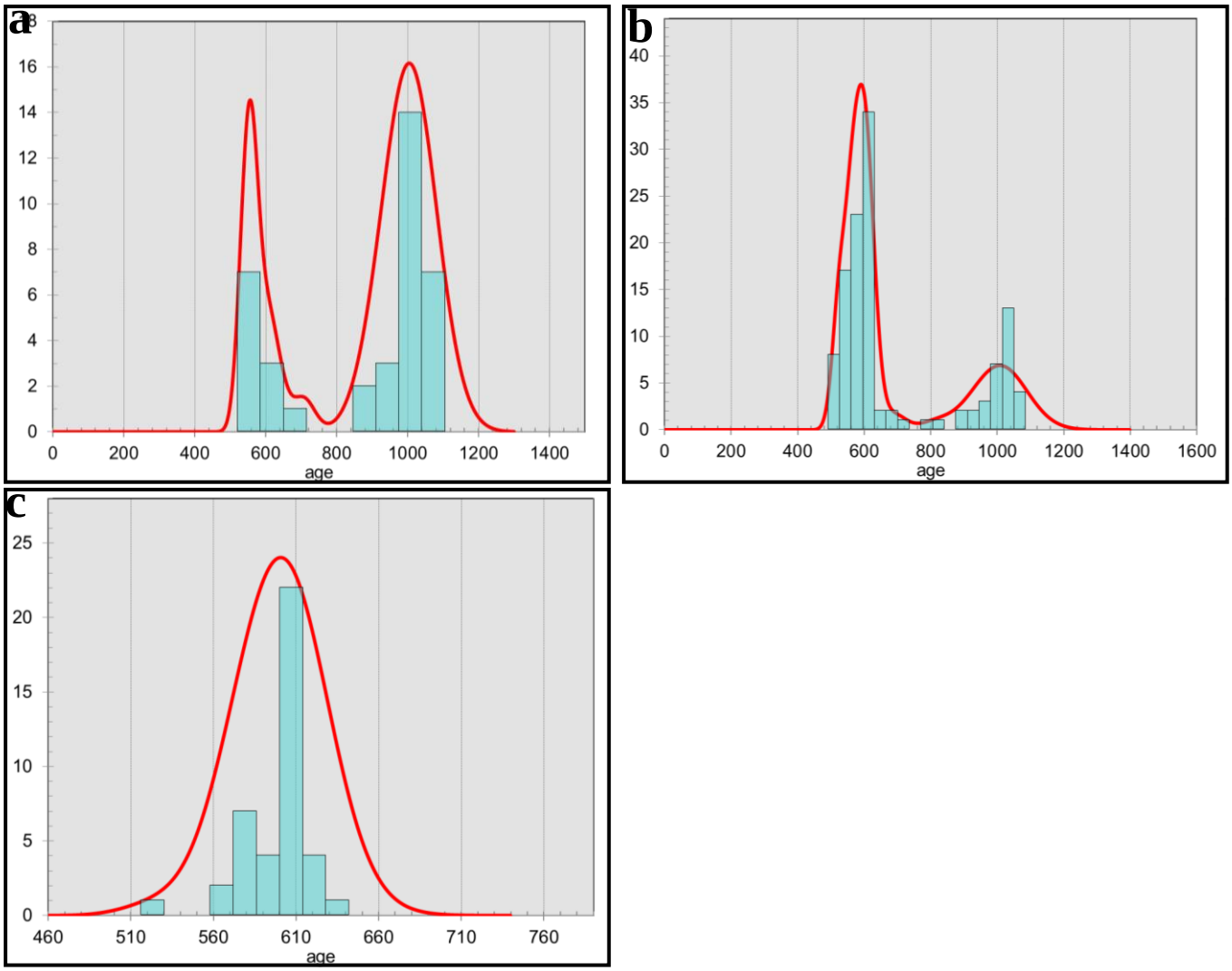

***Figure 8**: Probability density plots for (a) Granitic gneiss (Chis 69) (b) Biotite gneiss (Chis 62) and (c) biotite schist (Chis 52).*

5.4 Fluid inclusion petrography

Fluid inclusion (FI) petrography involved careful observation of the shapes, characteristics of spatial distribution, genetic and composition types, and vapor/liquid ratios. Based on fluid inclusion components and phase behaviour at room temperature (25°C), three types of inclusions were recognized, and these are liquid-rich aqueous inclusions, (H_2O-NaCl), aqueous carbonic (CO_2–H_2O) inclusions and pure carbonic (CO_2) inclusions.

Liquid-rich aqueous inclusions

These inclusions are one-phase (LH_2O) or two-phase (VH_2O + LH_2O) liquid-rich aqueous inclusions (Figure 9 a, b, c, d). The two-phase inclusions are more common with vapor volume occupying 10–40% of the total cavity volume. These inclusions vary in size from 10 to 20 μm and they have a variety of shapes ranging from irregular to elliptical and negative shapes. These inclusions form numerous planes, mostly crosscutting one another and are observed as arrays or trails along healed fractures. They also occur in isolation. They are interpreted to be secondary in origin.

Aqueous carbonic inclusions

These fluid inclusions are composed of H_2O and CO_2 phases with 5–90 vol.% carbonic phase (Figure 9e, f,g,h). They can be further divided into two subtypes, containing two-phase (VCO_2 +LH_2O) and three-phase (VCO_2+LCO_2+LH_2O) inclusions at room temperature. The volumetric proportions of CO_2 range from 5% to 90%. They generally occur in isolation or in clusters. Sometimes they appear as trails along healed fractures which do not cut across the crystal boundaries of quartz. These features suggest that they are primary or pseudosecondary. These inclusions vary in size ranging from 10-30 μm.

Pure carbonic inclusions

These FIs are generally dark with sub rounded to negative crystal shapes. They consist of almost pure carbonic phase lacking any visible H_2O at room temperatures, including monophase CO_2 (vapor or liquid). They are usually dark with oval crystal morphology (Figure 9 I,J,K). They occur either in isolation or in linear array. They range from 2- 15 μm in diameter. A few of these inclusions have a thin rim of aqueous solution filling up to 10% of the inclusion volume. The typically isolated and scattered nature of these inclusions indicates that they are primary inclusions.

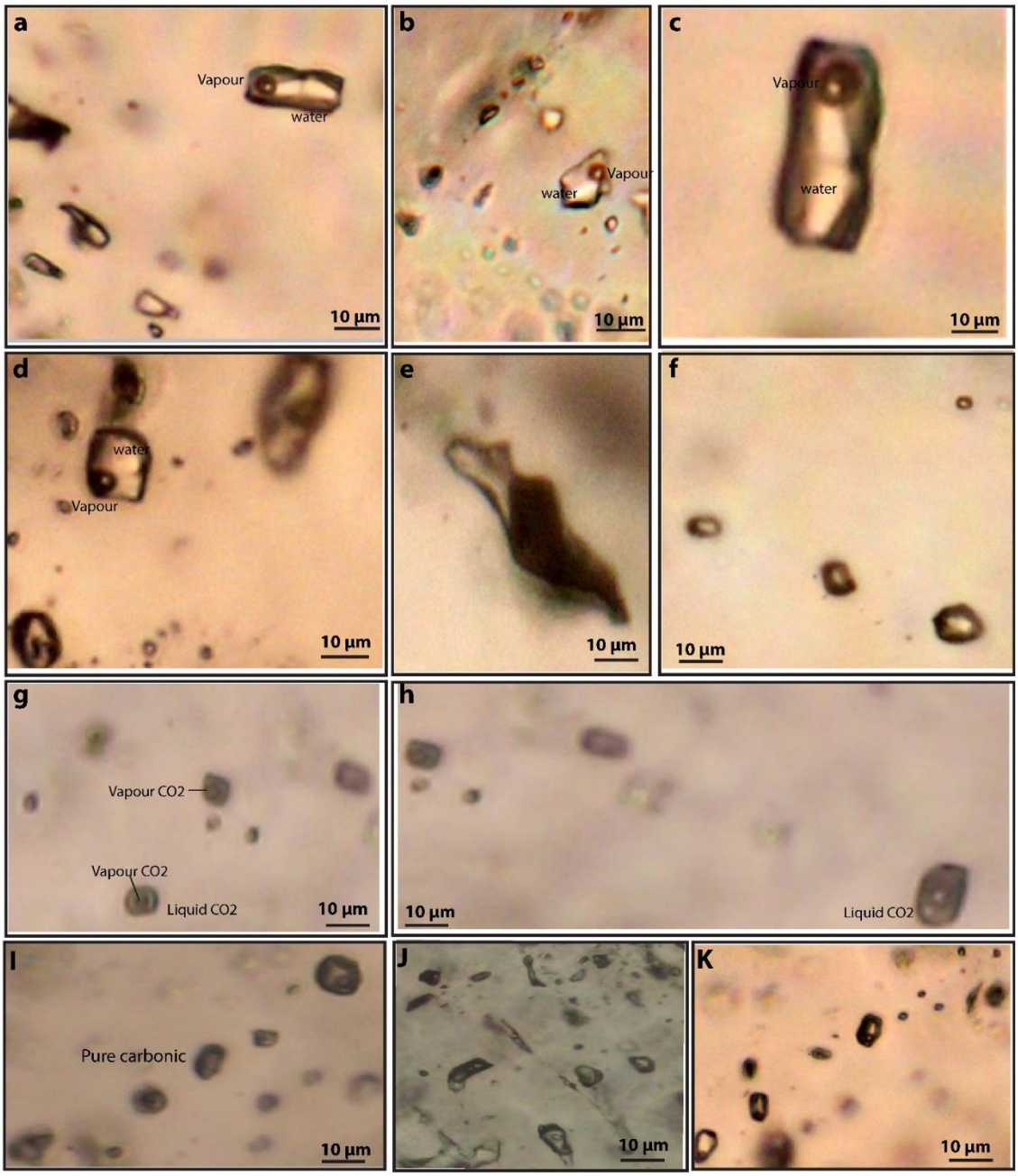

Figure 9: *types of fluid inclusions recognized at Manondo-Choma gold prospect from mineralized quartz veins, liquid-rich aqueous inclusions, (H_2O-NaCl), aqueous carbonic (CO_2–H_2O) inclusions and pure carbonic (CO_2) inclusions.*

5.5 Fluid inclusion microthermometry

Based on petrographic observation, and cross-cutting relationships, there were three stages of fluid flow: (early, middle and late). Early stage fluid flow is represented by the development of quartz carbonate veins with no gold mineralisation. The middle/main stage is characterized by quartz sulphide veins that crosscut the early carbonate veins and represents the main gold mineralisation stage. Quartz in this stage is fine grained, smoky and contains sulphides (Figure 2f,g). Majority gold is found in smoky quartz veins (Figure 2 h,i,j). The late stage fluid flow is characterized by milky vein, with trace pyrite and no gold, commonly occurring as veinlets along and crosscutting the foliation of altered wall rocks (Figure 2k). Microthermometric analyses were conducted on the veins. We describe the fluid properties of all the stages of fluid flow, specific emphasis is placed on the second stage fluid flow, because this is associated with mineralization. It is associated with the major sulphide mineralisation, and these sulphides are associated with free gold.

The number of different types of fluid inclusions within the quartz veins differs depending on the stage of fluid flow. The early stage contains liquid rich aqueous and aqueous carbonic fluid inclusion. The main stage contains all the three types of fluid inclusions. The late stage is dominated by liquid rich aqueous inclusions. Detailed microthermometric analysis was conducted on the fluid inclusions and the microthemometric data is summarized in Table 2 and Figures 10 - 12.

Table 2: Summary of the microthermometry data from fluid inclusion from the three fluid flow stages of the Manondo-Choma gold prospect. FI Type: fluid inclusion type, T_m CO_2: melting temperature of solid CO_2, T_m cla: temperature of CO_2 clathrate dissociation; T_hCO_2: homogenization temperature of CO_2: T_m ice,ice melting temperature, T_h; total homogenization temperature

Stage	FI Type	T_m CO_2 °C	T_mCla °C	T_h CO_2 °C	T_m ice °C	Th°C	Salinity	Density g/cm^3
Early	Carbonic	-60.8 to -56.8	5.3 to 6.6	24.to 31.2		300 to 349	6.06 to 8.68	0.23 to 0.63
	Aqueous				-9.1 to -1.3	303 to 390	2.23 to 12.95	0.62 to 0.78
Main	Carbonic	-60.1 to -56.7	3.7 to 9.8	17.2 to 32		285 to 350	0.038 to 7.67	0.15 to 0.80
	Pure Carbonic	-59.8 to -56.8		25.6 to 31.3		288 to 365		0.24 to 0.35
	Aqueous				-9.1 to -0.1	222 to 301	0.18 to 13. 1	0.70 to 0.90
Late	Aqueous				-9.8 to -0.8	148 to 220	1.39 to 13.72	0.87 to 0.99

The early fluid flow contain aqueous carbonic-type and liquid rich aqueous-type fluid inclusions. During freezing and heating, the aqueous carbonic-type fluid inclusions have solid CO_2 melting temperatures (Tm CO_2) of -60.8 °C to -56.8 °C, (Table 2, Figure 10d) suggesting that the carbonic phase contains CH_4 or N_2 and have CO_2 clathrate melting temperatures (Tclath,CO_2) of 5.3 to 6.6 °C, yielding salinities of 6.06–8.68 wt.% NaCl equivalent. The carbonic phases homogenize to a liquid phase at temperatures (Th,CO_2) from 24.0 °C to 31.2 °C, yielding carbonic phase densities of 0.23–0.63 g/cm^3. These FIs homogenize at temperatures (Th,TOT) of 300–349 °C and the majority homogenize into the liquid phase (Table 2, Figure 10a).

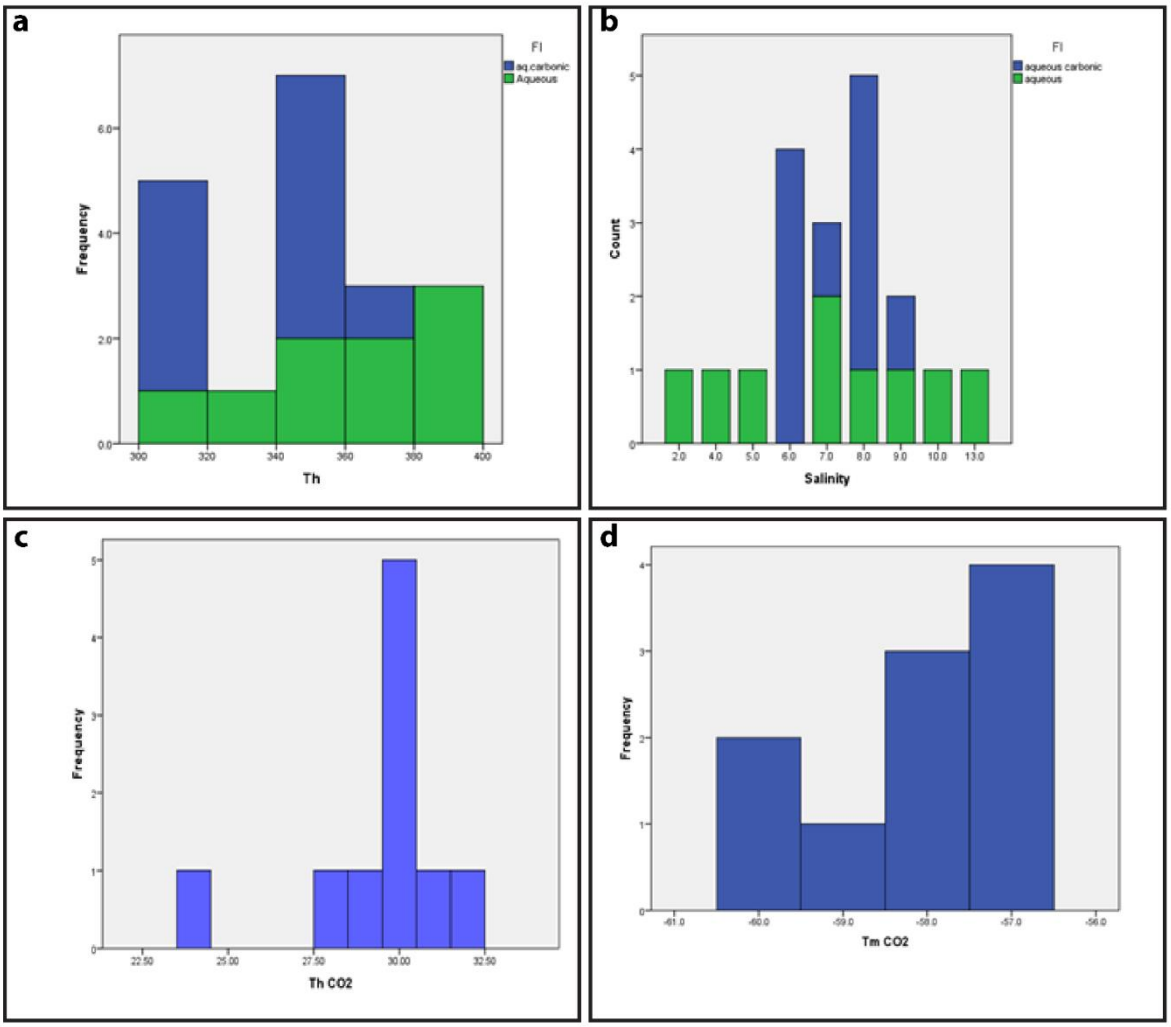

Figure 10: *Histograms of ore bearing fluid inclusions in the early stage. (a) total homogenization temperatures for aqueous carbonic and liquid rich aqueous fluids (b) salinity for aqueous carbonic and liquid rich aqueous fluids (c) homogenization temperature of CO_2 (d)melting temperature of solid carbon dioxide.*

The aqueous liquid rich-type fluid inclusions have final ice melting temperatures (Tm,ice) of -9.1 ºC to -1.3 °C, yielding salinities of 2.23 – 12.95 wt.% NaCl equivalent. These FIs homogenize at temperatures (Th,TOT) of 303–390 °C and the majority homogenize into the liquid phase, corresponding to densities of 0.62–0.78 g/cm^3 (Table 2, Figure 10a).

The main mineralisation stage (fluid flow) is associated with Aqueous Carbonic-type, Liquid rich aqueous type, and Pure Carbonic type Fluid inclusions. The aqueous Carbonic-type and

Pure Carbonic-type Fluid inclusions have Tm,CO_2 values from -60.1to -56.7 ºC, close to the CO_2 triple point (-56.6 °C), suggesting that the carbonic phase contains minor quantities of other volatiles, and have Tclath, CO_2 values from 3.7 °C to 9.8 °C, yielding salinities of 0.038 –7.67 wt.% NaCl equivalent. The carbonic phases homogenize to liquid at temperatures between 17.2 °C to 32°C, yielding carbonic phase densities of 0.15–0.80 g/cm^3. Several Pure Carbonic-type FIs homogenized into the vapor phase at temperatures of 285–350 °C. The Liquid rich aqueous -type FIs have Tm,ice values of -9.1 °C to -0.3 °C, yielding salinities of 0.18–13.1 wt.% NaCl equivalent. These FIs homogenize at temperatures (Th,TOT) of 222 °C to 301 °C, corresponding to densities of 0.70–0.90 g/cm^3 (Table 2, Figure 11).

In the late stage, only liquid-rich aqueous-type FIs were observed. Their freezing points range from -9.8 °C to -0.8°C, corresponding to salinities of 1.39 – 13.72 wt.% NaCl equivalent and they homogenize into the liquid phase at temperatures (Th,TOT) of 148 °C to 220 °C, yielding densities of 0.87–0.99 g/cm^3 (Table 2, Figure 12).

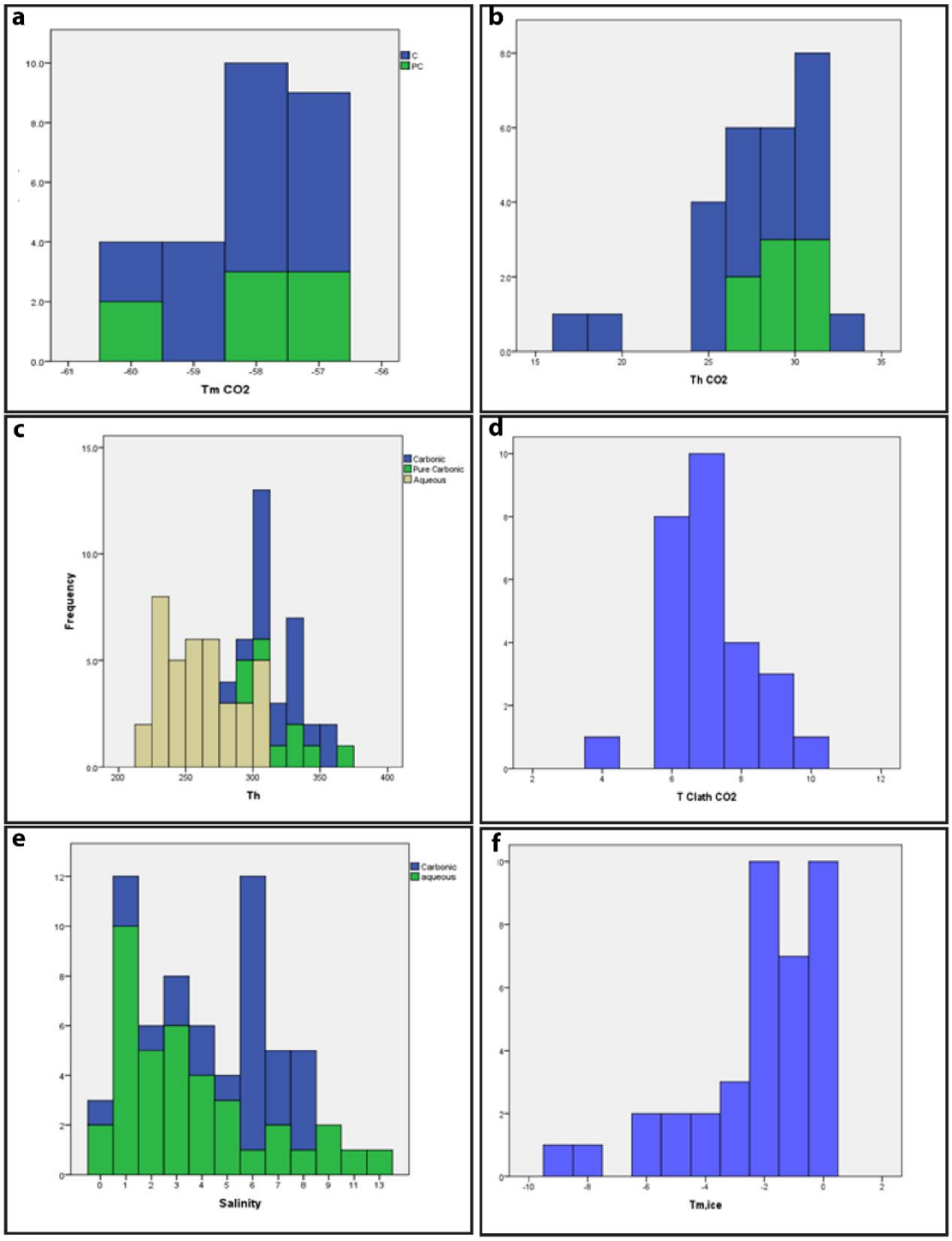

Figure 11: *Histograms of ore bearing fluid inclusions in the main stage. (a)melting temperature of solid carbon dioxide (b) homogenization temperature of CO2 liquid and vapour (c)total homogenization temperatures for aqueous carbonic,pure carbonic and liquid rich aqueous fluids (d) melting temperature of clathrate (e) salinity for aqueous carbonic and liquid rich aqueous fluids* (f) *final melting temperature of ice.*

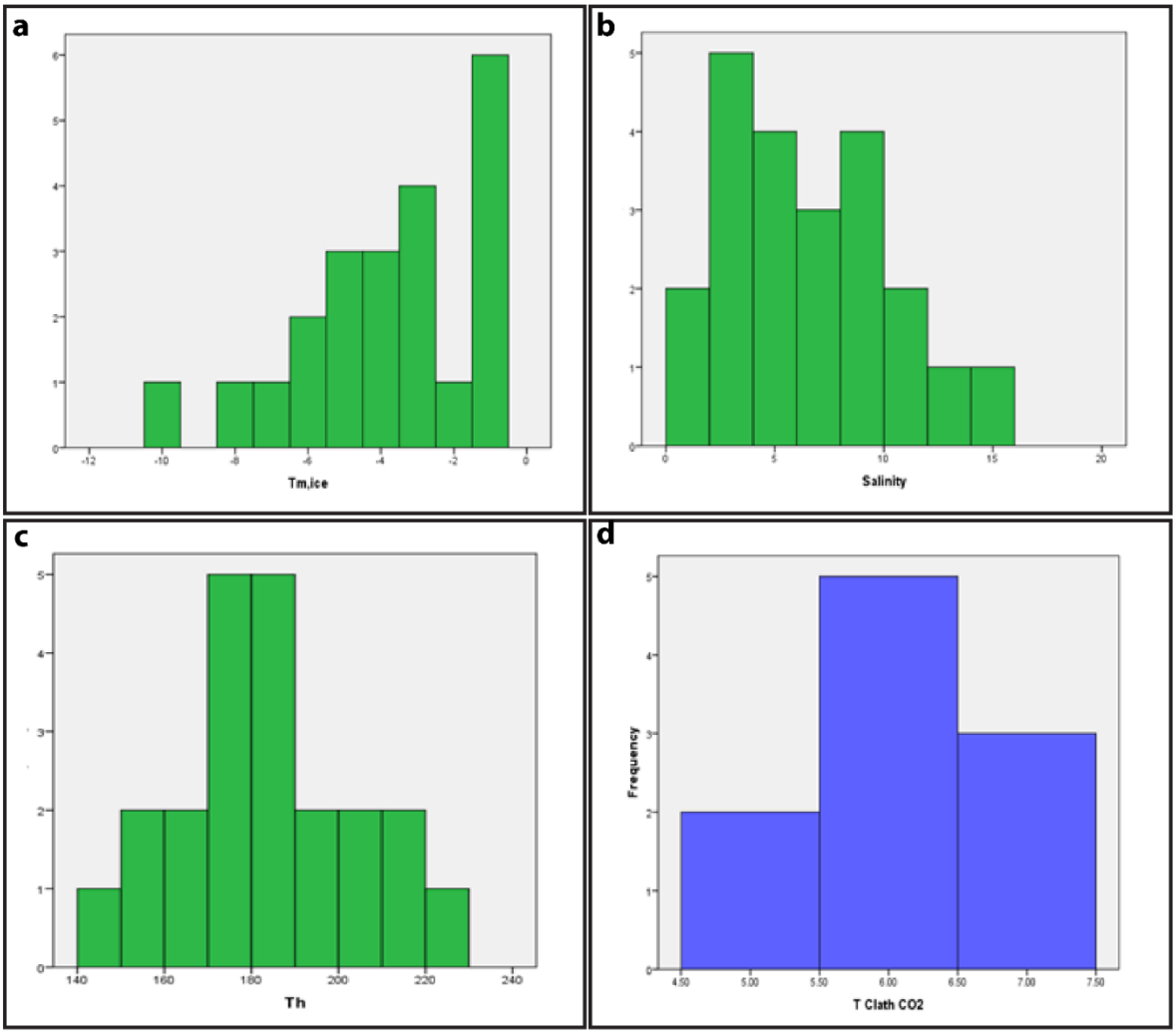

Figure 12: *Histograms of ore bearing fluid inclusions in the late stage. (a) final melting temperature of ice (b) salinity for liquid rich aqueous fluids (c) total homogenization temperature (d) melting temperature of clathrate.*

5.6 Oxygen stable isotopes

The oxygen stable isotopic data is presented in Table 3. The oxygen isotopic compositions of hydrothermal fluids were calculated by the fractionation formula $1000\ln \alpha$ Q-H_2O = $3.38x(10^6/T^{-2})-3.40$ (Clayton et al., 1972) and we used homogenization temperatures T of the fluid inclusions of the same samples. The analyzed $\delta^{18}O$ quartz values range from 7.0- 12.6 ‰, yielding calculated $\delta^{18}O_{H2O}$ values between 4.3 and 6.9‰ and δD values are in the range of −65 to −44‰.

Table* 3:** *Oxygen isotope composition from Manondo-Choma gold prospect.* ***$\delta^{18}O_m$ measured $\delta^{18}O$ *value of quartz;* ***$\delta^{18}O_w$*** *value of ore forming fluids in equilibrium with quartz calculated according to the equation $1000ln\alpha Q\text{-}H_2O = 3.38x(10^6/T^{-2})-3.40$ reported by Clayton et al., 1972. The temperatures used in calculation are the homogenization temperatures values of the fluid inclusion quartz samples.*

Sample	$\delta^{18}O_m$	$\delta^{18}O_W$	δ D	T_h
JJ01-1	12.6	4.3	-44	390
JJ01-2	10.1	4.3	-44	388
JJ01-3	11.4	4.4	-45	385
JJ01-4	11.1	4.9	-49	364
JJ01-5	9.2	5	-50	360
JJ01-6	12.7	5.3	-52	351
JJ02-1	10.6	5.3	-52	350
JJ02-2	8.7	5.7	-56	337
JJ02-3	7.1	6.8	-64	303
JJ02-4	7	6.9	-65	301
JJ02-5	8.7	6.9	-65	300

6.0 Discussion

6.1 Regional metamorphic history and geochronology

Two distinctly different U-Pb age patterns are recorded by the lithological units from the Kirk Range. Granitic gneiss and biotite gneiss lithologies samples Chis 69 and Chis 62 respectively show amphibolite - granulite facies mineral assemblages, and their concordia diagrams have upper intercept ages of ca. 1085 ± 28 Ma and 1103± 45 Ma. From zircon textures, we interpret this as representing a magmatic age i.e., the age of crystallisation of the protoliths of these rocks. Several magmatic suites have been recognized within this time interval in NE Mozambique (Bingen et al., 2009). Amphibolite to granulite-facies foliated orthogneisses rocks in Unango Complex described in Bingen et al., (2009) are associated with this magmatic event. Thus, from zircon U-Pb rim dates, these rocks were then metamorphosed during the Irumide period. This is evidenced by U–Pb data on zircon rims revealing ages between 1066±30 and 991±25 Ma (Figure 7). This metamorphism was overprinted at ca. 700 - 500 Ma during Pan- African deformation which reached amphibolite facies grade.

These lithologies in the study area therefore preserve a record of Mesoproterozoic and Neoproterozoic activities. Thus, from U-Pb zircon data, we suggest that after initial igneous activity at ca. 1103-1085 Ma the study area was subjected to at least two distinct metamorphic events that caused the growth of these zircon rims, an Irumide-age period of metamorphism and a Pan African period of metamorphism. Irumidian metamorphism has also been found by Johnson et al. (2005, 2006) and De Waele et al. (2009, 2006) in NE Mozambique and Zambia, and was interpreted to represent accretion of continental arcs to the margin of the Congo-Tanzania Craton at around 1020 Ma.

The lower intercept ages date at 513±22Ma (second population in probability density plots Figure 8) and zircon rims are interpreted to provide the estimates on the age of amphibolite-facies metamorphism during the Pan African Orogeny. This event overprinted the Mesoproterozoic Irumide orogenic event. Pan African metamorphism was prolonged and recorded zircon ages range from 700±2 to 500±17 Ma. According to our pseudosection modelling, the Kirk Range experienced metamorphic conditions of around 500°C to 600°C at roughly 10 to 15 kbar during Pan African event. During this event the Kirk Range and the whole of southern Malawi was metamorphosed under amphibolite to possibly granulite-facies conditions which was then followed by retrogression (Kröner, 2001). The retrogression P-T path is interpreted from symplectite corona textures around coarse garnet porphyroblasts. Small rims of plagioclase and amphibole grew around and replaced garnet (Figure 4e), indicating retrogression. Furthermore, corona textural growth replacement of garnet to amphibole and locally clinopyroxene (Figure 4c) denotes decompression at elevated temperatures (Gilotti et al., 2004).

The lack of older zircon ages in the biotite schist (sample Chis 52) signifies that their protoliths were probably of juvenile Pan African origin and were metamorphosed under amphibolite-facies conditions as a consequence of crustal thickening consistent with a subduction-collisional environment during Pan African (Bingen et al., 2009).

Lithologies in the Kirk Range therefore underwent polyphase metamorphic imprints at different times, i.e, during the Mesoproterozoic and Neoproterozoic events. Kro¨ner et al., (2001) also found out that the gneissic rocks of southern Malawi were affected by Mesoproterozoic Irumide and Neoproterozoic Pan African orogenies. Similar ages and P-T conditions have also been found by other researchers in NE Mozambique, Zambia and Malawi that are close to the Kirk Range (e.g., Engvik & Bingen, 2016; Jonson et al., 2006; Kröner,

2001; Manda et al., 2019; Bingen et al., 2009) an indication that the Kirk Range experienced high grade metamorphism during the Irumide and Pan African events.

6.2 Ore fluid physico-chemistry

6.2.1 Nature of ore-forming fluids, P-T conditions of ore deposition Metallogenic Depth and Source of the ore-forming fluids.

The fluid inclusion microthermometry data show that homogenization temperatures of the fluid inclusions in the main fluid flow vary around 222–301 °C and that pure carbonic-type, liquid rich aqueous type and aqueous carbonic type fluid inclusions coexist indicating that the ore-forming fluids were in a heterogeneous thermal condition when these fluid inclusions were trapped (Shepherd et al., 1991) and the initial homogeneous ore-forming fluids undergone fluid immiscibility. The original NaCl-H_2O-CO_2 fluids of Manondo-Choma gold prospect separated into CO_2-rich fluids and H_2O-rich fluids, resulting in capture of low-salinity CO_2-bearing inclusions and aqueous inclusions. During phase separation, escape of CO_2, led to huge changes in fluid composition and physical and chemical conditions, leading to decrease of Au solubility in the hydrothermal fluids and the rapid precipitation of gold. This suggests that gold at the Manondo-Choma prospect was precipitated from immiscible fluids.

PT conditions during mineralisation were estimated from the FI assemblages. The estimated pressures of the FIs at the Manondo – Choma gold prospect are shown in Figure 13 based on the CO_2–H_2O–NaCl system. Representative density isochores that were used to constrain the trapping pressures were calculated using Hokieflincs H_2O-NaCl (Steele-Macinnis, Lecumberri-sanchez, & Bodnar, 2012) and an algorithm for calculating H_2O-$NaCl_2$-CO_2 fluids developed by MacInnis et al., (2018). Intersections of isochores of FIs with the minimum and

maximum densities and homogenization temperatures range are used to constrain the minimum trapping pressure range (Zheng et al., 2012; Zhong et al., 2013). The minimum trapping pressures of the Manondo-Choma gold prospect range from 2.0–2.8 kbar in the main fluid flow event. Applying ground pressure gradient of 0.26 kbar/km (mean density of upper crust), the calculated trapping depth for the gold at Manondo-Choma corresponds to a depth of 7.6 to 10.7 km. This shows that the ore deposition occurred at mesothermal depth ranges at temperatures of 222–301°C, pressures of 2.0-2.80 kbar and at depths of 7.6 to 10.7 km (i.e., greenschist facies conditions). Ore forming fluids at the Manondo-Choma gold prospect are therefore low- to medium-temperature, low salinity fluids, and likely of metamorphic origin.

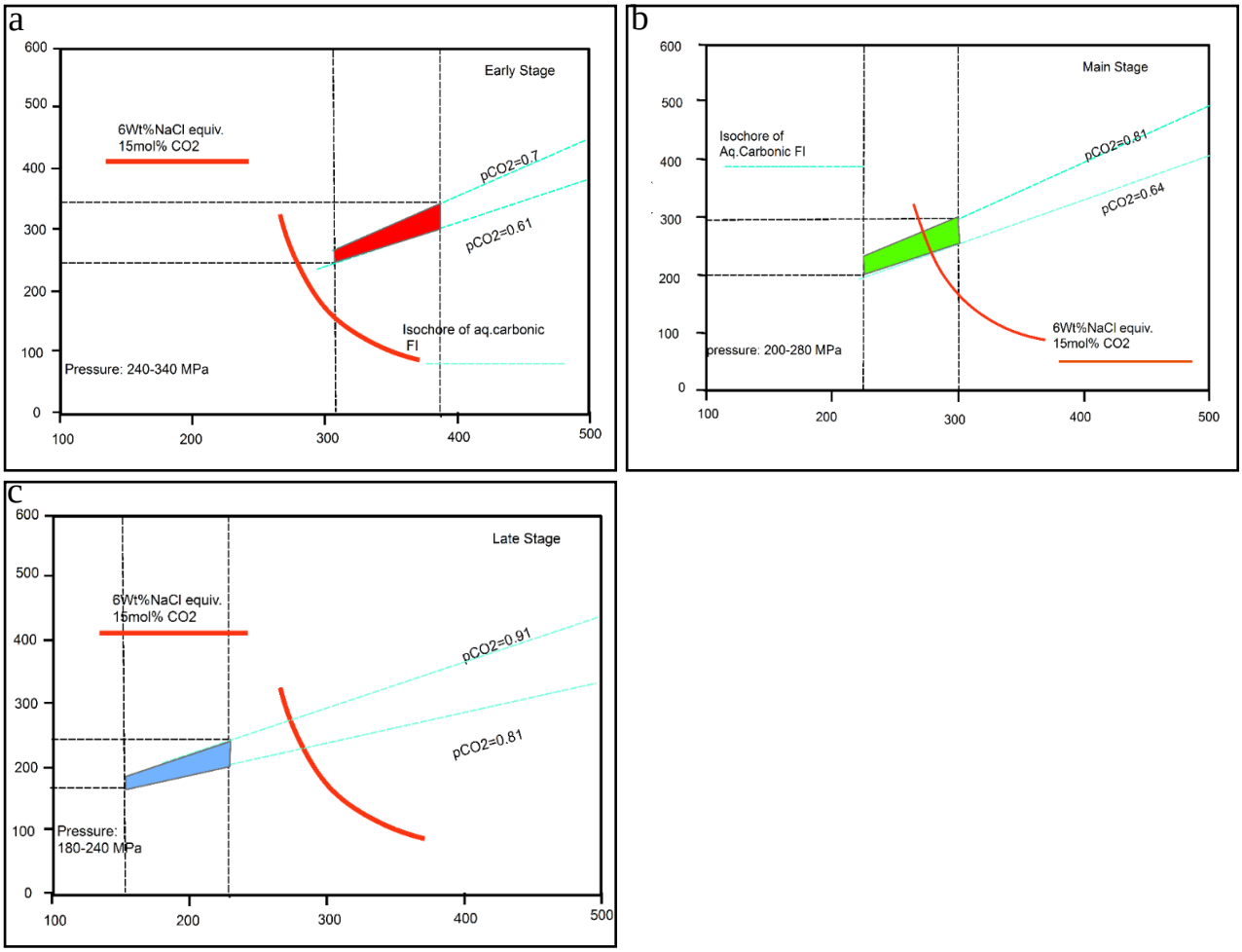

Figure 13: *Representative isochores for minimum and maximum CO_2 densities for H_2O-Nacl-CO_2 inclusions and solvus for H_2O-Nacl-CO_2 fluids containing 6 wt% equivalent NaCl and 15 mol% CO2 (after Bowers and Helgeson 1983). (a) The estimated trapping pressure-*

temperature diagram of the early stage mineralisation, (b) the estimated trapping pressure - temperature diagram of main mineralisation stage (c) the estimated trapping pressure-temperature diagram of the late stage mineralisation stage. The isochores were constructed using the program LonerAP (Bakker, 2003).

Further evidence for a metamorphic origin for the fluids is evidenced by the analytical data on oxygen isotopes of quartz veins and calculated $\delta^{18}O$ water values of ore-fluids (listed in Table 3). Oxygen isotope data fall in the metamorphic water field (Figure 14). The composition of the fluids (low-salinity and H_2O–CO_2–N_2–CH_4 in composition) is indicative of a metamorphic origin and are typical of the majority of orogenic gold deposits worldwide (Goldfarb & Groves, 2015). This is further substantiated on the salinity versus homogenization diagram (Figure 14b), fluid inclusion data from the Manondo-Choma gold prospect plot in the orogenic gold field.

In hydrothermal fluids, gold is predominantly transported as gold chloride ($AuCl_2^{-}$) and gold bisulfide complexes ($Au(HS)_2^{-}$). Commonly, the $AuCl_2^-$ complexes are prevalent in near-neutral to weakly alkaline, high salinity fluids, whereas for near-neutral to weakly acidic pH in sulfur-bearing solutions and at relatively low temperatures (<400°C), the $Au(HS)_2^-$ complexes play a more important role to transport gold. Taking into consideration that the ore-forming fluids at Manondo-Choma gold prospect were rich in CO_2 and relatively low temperatures, we infer that the gold was probably transported as $Au(HS)_2^-$ complexes in the ore-forming fluids, which is also consistent with the fact that gold is usually accompanied with sulfides (especially pyrite, Figure 3). Thus, gold deposition at Manondo-Choma prospect probably is related to the breakdown of gold bisulfide complexes ($Au(HS)_2^-$), which may have been caused by the fluid immiscibility (Naden & Shepherd, 1989; Cox, 1995) evidenced by the different FI assemblages observed in these samples.

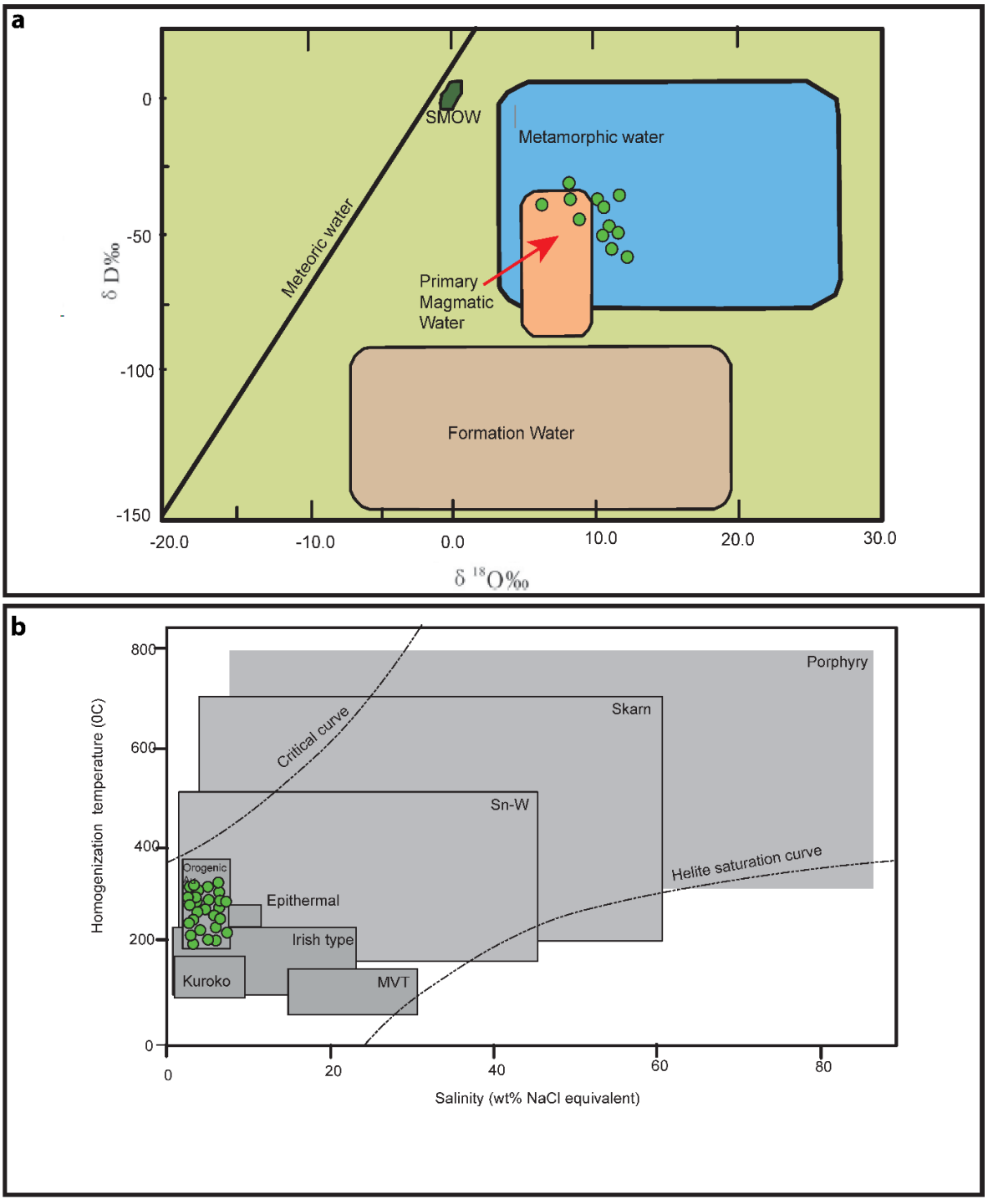

Figure 14: *δD vs $\delta^{18}O$ plot of the ore-forming fluids at the Manondo-Choma gold prospect, they plot in the metamorphic and primary magmatic water fields.* ***(b)*** *Summary homogenization temperature-salinity diagram indicating that fluid inclusion composition plot in the orogenic gold field (modified after* Wilkinson, 2001)

6.3 Timing of gold mineralisation

Gold mineralization is hosted in the foot-wall biotite schist unit. Geochronological evidence indicates that this unit is juvenile and it only experienced Pan African metamorphism and therefore mineralization is interpreted to be Pan African. Chisambi and von der Heyden (2019) tentatively interpreted mineralization to be related to Irumide metamorphism, based on the structural orientation of the lineaments, however new evidence derived from geochronology data has allowed us to update this earlier conclusion. Global models for orogenic gold mineralisation suggest Au mobilisation and ultimate mineralisation occurs preferentially under greenschist facies metamorphism (e.g. Goldfarb and Groves, 2015). Our fluid inclusion analyses reflect these conditions yet the surrounding host rocks reveal much higher PT conditions. This apparent discrepancy is explained by a model in which gold mobilises early in the protracted and polyphase Pan African metamorphic cycle (Collins & Pisarevsky, 2005) during lower metamorphic grade conditions. We suggest that the maximum PT conditions experienced by the host rocks (i.e., 500-600ºC and 10-15 kbar) occurred during later stages of Pan African metamorphism and once the rocks had already experienced the gold mineralisation event. This model in which early orogenic gold mineralisation is transposed by subsequent deformation would explain the apparent discrepancy, the stretched microscale gold textures described in Chisambi and von der Heyden (2019), and the extensive and relatively low Au grades in the region. This model is similar to Mt. York District, Pilbara Block, Western Australia gold deposit, described by Neumayr et al., (1993) where gold mineralisation is also hosted in high grade metamorphic rocks of amphibolite – granulite facies and mineralisation occurred before peak metamorphism.

Earlier work (British Geological Survey, 2009) proposed the Manondo-Choma thrust to be the controlling structure for gold mineralisation. However according to this study, the thrust is not related to mineralization, as it occurred late in the Pan African event. The thrust sheet actually

covered the original low-grade gold mineralization, and due to this covering, it will make exploration difficult, and limited to the geological 'vensters' which expose the biotite schist lithology. This model suggest that it is therefore unlikely to find primary economic gold mineralization in the Kirk Range. However, erosion through this thrust sheet has liberated the transposed gold into placer concentrations. This is evidenced by the abundance of artisanal gold diggings along the drainage systems that cut the foot-wall biotite schist. The erosional windows can therefore still be a target for placer gold exploration.

7.0. Conclusions

The Kirk Range experienced metamorphism and orogenesis during both the Irumide Orogeny and the later Pan African orogeny. In the present study area, the Irumide orogenic event occurred at around 1066-991 Ma and Pan African orogeny occurred at around 700-485 Ma. Our results suggest that the mineralization occurred in the early stages of protracted Pan African event before peak metamorphism under greenschist facies conditions. Later deformation to amphibolite facies conditions of metamorphism during the prolonged Pan African event led to the transposition of the original mineralization. The initial ore-forming fluids were metamorphic derived from metamorphic devolatilisation. The Au was likely transported by bisulphide complex that then destabilized. The Manondo-Choma gold prospect and its fluid chemistry shares many similar characteristics with those of orogenic gold deposits worldwide, and therefore we suggest that this gold prospect area belongs to orogenic type.

References

Achille, M., & Andreoli, G. (2001). Petrochemistry, Tectonic Evolution And Metasomatic Mineralisations Of Mozambique Belt Granulites From S Malawi And Tete (Mozambique). *Precambrian Research*, *25*(1984).

Ackermann, E. H. (1950). Ein neuer Faltengürtel in Nordrhodesien und seine tektonische Stellung im Afrikanischen Grundgebirge. *Geologische Rundschau*, *38*, *24–39*.

Ackermann, E. H., & Forster, A. (1960). Grundzuge der Stratigraphie und Struktur des Irumide Orogen. In: *21st International Geological Congress*, pp. 182–192.

Andreaoli, M. (1984). Petrochemistry,Tectonic Evolution and metasomatic Mineralisation of Mozambique belt Granulites from South Malawi and Tete (Mozambique). *Precambrian Research*.

Bakker, R. J. (2003). Package FLUIDS 1 . Computer programs for analysis of fluid inclusion data and for modelling bulk fluid properties. *Chemical Geology*, *194*, 3–23.

Bingen, B., Jacobs, J., Viola, G., Henderson, I. H. C., Skår, Ø., Boyd, R., … Daudi, E. X. F. (2009). Geochronology of the Precambrian crust in the Mozambique belt in NE Mozambique , and implications for Gondwana assembly. *Precambrian Research*, *170*, 231–255. https://doi.org/10.1016/j.precamres.2009.01.005

Bjerkgard, T., Stein, H. J., Bingen, B., Henderson, I. H. C., Sandstad, J. S., & Moniz, A. (2009). The Niassa Gold Belt , northern Mozambique – A segment of a continental-scale Pan-African gold-bearing structure ? *Journal of African Earth Sciences*, *53*(1–2), 45–58. https://doi.org/10.1016/j.jafrearsci.2008.09.003

Bloomfield.K, & Garson.M.S. (1965). The Geology of the Kirk Range-Lisungwe Valley Area.

Ministry of Natural Resources. Geological Survey Department. Bulletin No.17. *The Government Printer, Zomba. Malawi*.

Bodnar, R. J. (1993). Synthetic fluid inclusions : XII . The system H20-NaCI . Experimental determination of the halite liquidus and isochores for a 40 wt % NaCl solution *. *Geochimica et Cosmochimica Acta*, *58*(3), 1053–1063.

Boniface, N., Schenk, V., & Appel, P. (2014). Mesoproterozoic high-grade metamorphism in pelitic rocks of the northwestern Ubendian Belt : Implication for the extension of the Kibaran intra-continental basins to Tanzania. *Precambrian Research*, *249*, 215–228. https://doi.org/10.1016/j.precamres.2014.05.010

Boyd, R., Nordgulen, Ø., Thomas, R. J., Bingen, B., Bjerkgård, T., Grenne, T., … Jamal, D. (2010). The Geology And Geochemistry Of The East African Orogen In Northeastern Mozambique. *Geological Society of South Africa*, *113*, 87–129. https://doi.org/10.2113/gssajg.113.1.87

British Geological Survey. (2009). *Mineral Potential of Malawi*.

Cater, G. ., & Bennet, J. . (1973). *The Geology and Mineral Resources of Malawi*. Zomba: Government print, Zomba, Malawi.

Chisambi, J, & von der Heyden, B. (2019). Primary gold mineralization in the Lisungwe Valley area, Kirk Range, southern Malawi. *South African Journal of Geology*, *122*(4). https://doi.org/https://doi.org/10.25131/sajg.122.0039

Chisambi, Joshua, Heyden, B. Von Der, Tshibalanganda, M., & Stephan, L. R. (2020). Gold Exploration in Two and Three Dimensions: Improved and Correlative Insights from Microscopy and X-Ray Computed Tomography. *Minerals*, 1–20. https://doi.org/doi:10.3390/min10050476

Clayton et al. (1972). Oxygen isotope exchange between quartz and water. *Journal of Geophysical Research*, *77*, 3057–3067.

Clayton, R., & Mayeda, T. K. (1963). The use of bromine pentafluoride in the extraction of oxygen from oxides and silicates for isotopic analysis *. *Geochimica et Cosmochimica Acta*, (1953).

Collins, A. ., & Pisarevsky, S. . (2005). Amalgamating eastern Gondwana: the evolution of the Circum-Indian Orogens. *Earth Science Reviews*, *71*, 229–70.

Cox, F. (1995). Faulting processes at high fluid pressures: An example of fault valve behavior from the Wattle Gully Fault, Victoria, Australia. *Journal of Geophysical Research*, *100*.

De Waele. (2003). Untying the Kibaran knot : A reassessment of Mesoproterozoic correlations in southern Africa based on SHRIMP U-Pb data from the Irumide belt. *Geological Society Of America*, (6), 509–512.

De Waele, B., Fitzsimons, I. C. W., Tembo, F., & Mapani, B. (2009). The geochronological framework of the Irumide Belt : A prolonged crustal history along the margin of the Bangweulu Craton. *American Journal of Science*, (February). https://doi.org/10.2475/02.2009.03

De Waele, B., Liegeois, J., Nemchin, A. A., & Tembo, F. (2006). Isotopic and geochemical evidence of proterozoic episodic crustal reworking within the irumide belt of south-central Africa , the southern metacratonic boundary of an Archaean Bangweulu Craton. *Precambrian Research*, *148*, 225–256. https://doi.org/10.1016/j.precamres.2006.05.006

Dill, H. G. (2007). A review of mineral resources in Malawi : With special reference to aluminium variation in mineral deposits. *Journal of African Earth Sciences*, *47*, 153–173. https://doi.org/10.1016/j.jafrearsci.2006.12.006

Dulanya, Z. (2017). A review of the geomorphotectonic evolution of the south Malawi rift. *Journal of African Earth Sciences*.

Dulanya, Z., Morales-simfors, N., & Sivertun, Å. (2010). Journal of African Earth Sciences Comparative study of the silica and cation geothermometry of the Malawi hot springs : Potential alternative energy source. *Journal of African Earth Sciences*, *57*(4), 321–327. https://doi.org/10.1016/j.jafrearsci.2009.11.001

Engvik, A. K., & Bingen, B. (2016). Granulite-facies metamorphism of the Palaeoproterozoic – early Palaeozoic gneiss domains of NE Mozambique , East African Orogen. *Geological Magazine*. https://doi.org/10.1017/S0016756816000145

Gilotti et al. (2004). Devonian to Carboniferous collision in the Greenland Caledonides : U-Pb zircon and Sm-Nd ages of high-pressure and ultrahigh-pressure metamorphism. *Contributions to Mineralogy and Petrology*, *148*, 216–235. https://doi.org/10.1007/s00410-004-0600-4

Goldfarb, R. J., & Groves, D. I. (2015). Orogenic gold : Common or evolving fl uid and metal sources through time. *Lithos*, *233*, 2–26. https://doi.org/10.1016/j.lithos.2015.07.011

Goldstein, R. H. (2003). Petrographic analysis of fluid inclusions. In: Samson, I., Anderson, A., Marshall, D. (Eds.), Fluid Inclusions: Analysis and Interpretation. *Mineralogical Association of Canada Short Course*, *32*, 9–53.

Holland, T. J. B., & Powell, R. (1998). An internally consistent thermodynamic dataset for phases of petrological interest. *Journal of Metamorphic Geology*, *16*, 309–343.

Hoppe, G. (1966). Zirkone aus Granuliten. *Ber. Deutsch. Ges. Geol. Wiss. B, Miner. Lagerstättenforsch.*, 47–81.

Hori, T., & Tomita, K. (1997). Regional Geochemical Reconnaissance of Kirk Range-

Lisungwe, Malawi. *Kagoshima University*.

Horstwood et al. (2016). Community-Derived Standards for LA-ICP-MS U- (Th-) Pb Geochronology – Uncertainty Propagation , Age Interpretation and Data Reporting. *Geostandards and Geoanalytical Research*, *40*, 311–332. https://doi.org/10.1111/j.1751-908X.2016.00379.x

Hoskin, P., & Black, L. . (2000). Metamorphic zircon formation by solid-state recrystallization of protolith igneous zircon. *Jounal of Metamorphic Geology*, *18*(1992), 423–439.

Jackson, S. E., Pearson, N. J., Griffin, W. L., & Belousova, E. A. (2004). The application of laser ablation-inductively coupled plasma-mass spectrometry to in situ U – Pb zircon geochronology. *Chemical Geology*, *211*, 47–69. https://doi.org/10.1016/j.chemgeo.2004.06.017

Johnson et al. (2005). A review of the Mesoproterozoic to early Palaeozoic magmatic and tectonothermal history of south – central Africa : implications for Rodinia and Gondwana. *Journal of Geological Society of London*, *162*, 433–450.

Johnson et al. (2006). U-Pb sensitive high-resolution ion microprobe (SHRIMP) zircon geochronology of granitoid rocks in eastern Zambia : Terrane subdivision of the Mesoproterozoic Southern Irumide Belt. *Tectonics*, *25*. https://doi.org/10.1029/2006TC001977

Karmakar, S., & Schenk, V. (2016). Mesoproterozoic UHT metamorphism in the Southern Irumide Belt , Chipata , Zambia : Petrology and in-situ monazite dating Mesoproterozoic UHT metamorphism in the Southern Irumide Belt , Chipata , Zambia : Petrology and in situ monazite dating. *Precambrian Research*, *275*(January), 332–356. https://doi.org/10.1016/j.precamres.2016.01.018

Kro¨ner et al. (2001). Single zircon ages , PT evolution and Nd isotopic systematics of high-grade gneisses in southern Malawi and their bearing on the evolution of the Mozambique belt in southeastern Africa. *Precambrian Research*, *109*, 257–291.

Kröner et al. (1994). Pb-loss patterns in zircons from a high-grade metamorphic terrain as revealed by different dating methods : U - P b and Pb- Pb ages for igneous and metamorphic zircons from northern Sri Lanka. *Precambrian Research*, *66*, 151–181.

Kröner et al. (1997). Kibaran magmatism and Pan-African granulk metamwphism in northern Mozambique : siqle zircon ages and -regional implications. *Journal of African Earth Sciences*, *25*(3).

Macey, P. H., Miller, J. A., Rowe, C. D., Grantham, G. H., Siegfried, P., Armstrong, R. A., … Bacalau, J. (2010). Geology of the Monapo Klippe , NE Mozambique and its significance for assembly of central Gondwana. *Precambrian Research*, *233*, 259–281. https://doi.org/10.1016/j.precamres.2013.03.012

Macey, P. H., Thomas, R. J., Grantham, G. H., Ingram, B. A., Jacobs, J., Armstrong, R. A., … Manhic, V. (2010). *Mesoproterozoic geology of the Nampula Block , northern Mozambique : Tracing fragments of Mesoproterozoic crust in the heart of Gondwana*. *182*, 124–148. https://doi.org/10.1016/j.precamres.2010.07.005

MacInnis et al. (2018). H2O–NaCl, Fluid inclusions, Microthermometry, PVTX, Isochores. *Computers & Geosciences*.

Malunga, G. (1992). *Geochemical Exploration of Gold in the Likudzi Block, Geological Survey of Malawi, unpublished report*. Geological Survey of Malawi, unpublished report.

Manda, B. W. C., Cawood, P. A., Spencer, C. J., Prave, T., Robinson, R., & Roberts, N. M. W. (2019). Evolution of the Mozambique Belt in Malawi constrained by granitoid U-Pb , Sm-

Nd and Lu-Hf isotopic data. *Gondwana Research*, *68*, 93–107. https://doi.org/10.1016/j.gr.2018.11.004

Mayne, M. J., Moyen, J., Stevens, G., & Kaislaniemi, L. (2016). Rcrust : a tool for calculating path-dependent open system processes and application to melt loss. *Jounal of Metamorphic Geology*, 663–682. https://doi.org/10.1111/jmg.12199

McConnell, R. B. (1950). *Outline of the geology of Ufipa and Ubende. Bulletin of Geological Survey of Tanganyika*.

Naden, J., & Shepherd. (1989). Role of Methane and carbon dioxide in gold deposition. *Nature*.

Neumayr et al. (1993). The mineralogical distribution of gold and relative timing of gold mineralization in two Archean settings of high metamorphic grade in Australia. *The Canadian Mineralogist, 31, 711–72.*

Paton et al. (2011). Iolite: Freeware for the visualisation and processing of mass spectrometric data. *J.Anal.At.Specrom*, *26*(2508), 2508–2518. https://doi.org/10.1039/c1ja10172b

Petrus, J. A., & Kamber, B. S. (2012). VizualAge : A Novel Approach to Laser Ablation ICP-MS U-Pb Geochronology Data Reduction. *Geostandards and Geoanalytical Research*, *36*, 247–270. https://doi.org/10.1111/j.1751-908X.2012.00158.x

Ring, U., Kröner, A., & Toulkeridis, T. (1997). Palaeoproterozoic granulite-facies meta-morphism and granitoid intrusions in the Ubendian-Usagaran Orogen ofnorthern Malawi, east-central Africa. *Precambrian Reserch., 85, 27–51.*

Ring, U., & Kronner, A. (2002). Shear-zone patterns and eclogite-facies metamorphism in the Mozambique belt of northern Malawi , east-central Africa : implications for the assembly of Gondwana. *Precambrian Research*, *116*, 19–56.

Roedder, E. (1984). Fluid Inclusions. Reviews in Mineralogy. *Mineralogical Society of*

America, *12*, 644.

Shepherd et al. (1991). Fluid inclusion volatiles as an exploration guide to black shale-hosted gold deposits , Dolgellau gold belt , North Wales , UK. *Journal of Chemical Exploration*, *42*, 5–24.

Silver, L. T. (1969). *A geochronological investigation of the anorthosite complex, Adirondack Mountains, New York. In: Isachsen, Y.W. (Ed.), Origin of anorthosite and related rocks. New York Museum and Science Service, Mem. 18, pp. 57–82.*

Sláma et al. (2008). Ple š ovice zircon — A new natural reference material for U – Pb and Hf isotopic microanalysis. *Chemical Geology*, *249*, 1–35. https://doi.org/10.1016/j.chemgeo.2007.11.005

Sommer et al. (2003). Metamorphic petrology and zircon geochronology of high-grade rocks from the central Mozambique Belt of Tanzania : crustal recycling of Archean and Palaeoproterozoic material during the Pan-African orogeny. *Journal of Metamorphic Geology*, 915–934. https://doi.org/10.1046/j.1525-1314.2003.00491.x

Steele-Macinnis, M., Lecumberri-sanchez, P., & Bodnar, R. J. (2012). HOKIEFLINCS_H2O-NACL: A Microsoft Excel spreadsheet for interpreting microthermometric data from fluid inclusions based on the PVTX properties of H 2 O – NaCl. *Computers and Geosciences*, *49*, 334–337.https://doi.org/10.1016/j.cageo.2012.01.022

Westerhof, A. B. P., Lehtonen, M. I., Mäkitie, H., Manninen, T., Pekkala, Y., Gustafsson, B., & Tahon, A. (2008). The Tete-chipata belt : A new multiple terrane element from Western. *Geological Survey of Finland, Special Paper 48, 145–166, 2008*, (March 2015).

Wiedenbeck et al. (1995). Further Characterisation of the 91500 Zircon Crystal. *Geostandards and Geoanalytical Research*, *28*, 9–39.

Wilkinson, J. J. (2001). *Fluid inclusions in hydrothermal ore deposits*.

Zheng, Y., Zhang, L., Chen, Y., Qin, Y., & Liu, C. (2012). Geology , fl uid inclusion geochemistry , and 40 Ar / 39 Ar geochronology of the Wulasigou Cu deposit , and their implications for ore genesis , Altay , Xinjiang , China. *Ore Geology Reviews*, *49*, 128–140. https://doi.org/10.1016/j.oregeorev.2012.09.005

Zhong, R., Li, W., Chen, Y., Yue, D., & Yang, Y. (2013). P-T-X conditions , origin , and evolution of Cu-bearing fl uids of the shear zone-hosted Huogeqi Cu – (Pb – Zn – Fe) deposit , northern China. *Ore Geology Reviews*, *50*, 83–97. https://doi.org/10.1016/j.oregeorev.2012.10.003

CHAPTER 5

Conclusions and Genetic Model for Gold Mineralisation at Manondo-Choma Area

Prior to this work, not much was known about the characterisation and properties of primary gold mineralisation in the Manondo Choma gold district. I have applied a combination of techniques towards fully characterising the deposit and contextualising the host rocks with respect to new knowledge about the regional geology in which mineralisation is hosted. The use of multiple techniques has been effective in better understanding the genetic aspects of the Manondo-Choma gold prospect and has helped in characterizing the ore genesis, thus providing important insights into further exploration and mineralisation potential of the area. This has been demonstrated in Chapter 2 where we highlight the advantages of combining two-dimensional chemical and mineralogical data with three-dimensional structural/positional data for understanding the spatial distribution of gold and associated structures and micro-structures in 3D space, and in Chapter 4 where we applied regional geochronology and metamorphic modelling in concert with local fluid inclusion microanalysis to disentangle the relative timing of the mineralisation.

5.1. Summary of research techniques applied to the Manondo-Choma gold prospect

5.1.1. Regional geophysics

The regional geophysics data used in this study included magnetic anomaly measurements and gamma-ray spectrometric measurements of the potassium (K), thorium (Th) and uranium (U) signals (Sander Geophysics, 2013). Regional geophysics enabled us to delineate the regional

scale structures that were interpreted as part of the Irumide and Pan African structures based on the regional geological work that was done before.

5.1.2. Field mapping

Field mapping enabled us to identify lithologies and sampling of these lithological units for subsequent work. It also enabled us to understand the structural geology of the study area and to develop a regional and local understanding of the characteristics of gold mineralisation.

5.1.3. Microscopies

Microscopy work enabled us to understand mineral textures and parageneses as well as spatial information on microstructures associated with gold mineralisation in 2D space. The technique provided detailed 2D textural, chemical and mineralogical information regarding gold mineralisation.

5.1.4 X-ray Computed Tomography (XCT)

XCT enabled us to further characterise gold mineralisation and understand its distribution in 3D space. Whereas petrographic approaches only provided mineralogical and spatial information in two dimensions, X-ray computed tomography (XCT) enabled detailed spatial resolution of mineralogical information in three dimensions.

5.1.5 Fluid Inclusion

Fluid inclusion enabled us to understand the geochemistry /fluid characteristic and physical-chemical conditions that led to gold precipitation. We were able to recognise the types of inclusions present at our study area, understand the microthermometric behaviour of the fluids i.e., phase changes when heating and cooling which led to an understanding of the fluids chemistry, composition and physical chemical conditions that led to gold precipitation.

5.1.6. $\delta^{18}O$ isotopes of vein quartz

This technique enabled us to understand the source of the mineralising hydrothermal fluids. Using this technique, we were able to know that the fluids at Manondo-Choma gold deposit had a metamorphic source.

5.1.7 Zircon geochronology

This technique enabled us to understand the metamorphic history, ages and the geology of the study area and put in context of regional geology perspective. This technique made us know that the lithologies in the study area had been affected by the Irumide and Pan Africanorogenies.

5.2. Genetic model for gold mineralisation at Manondo-Choma gold prospect

Based on a combination of the techniques described in 5.1., a holistic understanding of the gold mineralisation at the Manondo-Choma prospect has been developed and we describe it in a context of an improved understanding of the regional geological history of the area.

This study has shown that the major lithologies in the area comprise a suite of NE trending gneissic rocks that are characterized by polyphase deformation. The area is dominated by Manondo-Choma thrust fault that separates a moderately steep south-easterly dipping crystalline hanging-wall, from highly deformed and isoclinally-folded schistose lithologies in the footwall (Figure 2, Chapter 3). Gold mineralisation is hosted exclusively in the biotite schist foot wall unit. This biotite schist unit represents an erosional window into the footwall of the Manondo-Choma thrust. Metamorphic conditions and ages (Irumide and Pan African) correspond to a ‘normal’ hanging wall-footwall geometry and would indicate that older rocks were thrust onto autochthonous or parautochthonous Pan-African rocks.

Metamorphism of the protolith to the biotite schist rocks (and underlying units) in the foot wall, led to the release of metamorphic fluids to form primary orogenic-style Au mineralization. Hydrothermal fluids were released during devolatilization as the rocks were being metamorphosed (Figure 1c). These fluids might have carried gold along with them as they were migrating upwards along shear zones or hydraulic fracture zones. Gold mineralisation therefore must have occurred by influx of gold-bearing hydrothermal fluid from the biotite schist rocks under greenschist facies conditions early in the extended Pan-African tectonic history before peak metamorphism.

Taking into consideration that the ore-forming fluids at Manondo-Choma gold prospect were rich in CO_2 and relatively low temperatures, we infer that the gold was transported as $Au(HS)_2^-$ complexes in the ore-forming fluids. Thus, gold deposition at Manondo-Choma prospect is related to the destabilisation of gold bisulfide complexes ($Au(HS)_2^-$). The two mechanisms proposed for this destabilisation reaction (which are not mutually exclusive) include redox shifts related to interaction between hydrothermal fluids and the Fe-bearing biotite schist host rock, and fluid immiscibility as evidenced by the co-occurring fluid inclusion assemblages.

However, the Kirk Range comprises low-grade Au mineralisation mainly because mineralisation has been transposed and dismembered (Figure 1d). The later Pan African tectonism during the protracted pan African event transposed the original mineralisation as metamorphism proceeded to higher grades. Given the intensities of strains and transposition in the footwall, this definitely renders exploration for primary mineralization a challenge. Also, the formation of the Manondo-Choma thrust covered the original mineralisation (Figure 1e). This further complicates exploration for primary gold mineralization in the Kirk Range. This explains why different exploration activities in the area were not a success. But the terrain/windows can still provide a source for placer gold. Erosion through the thrust sheet liberates the transposed gold into placer concentrations below the thrust (Figure 1f). This is

evidenced by dispersed mineralization which is confined and concentrated in this erosional window. Artisanal workings are also confined in streams along this unit, which indicates that there is a connection between footwall schist and artisanal diggings. Similar placer gold deposits which share same characteristics as Manondo-Choma have also been found elsewhere, e.g. Klondike and Nome in Alaska where placer gold is washed from parent high grade metamorphic rocks and concentrated in the beds of the streams brought by erosion and dissection of older primary mineralisation (Goldfarb, Snee and Pickthorn, 1993). Erosion concentrates gold into secondary mineralisation. Therefore, exploration in the Kirk Range should focus on these erosion windows for placer gold, as primary mineralization will be hard to find.

The study area polyphase deformation share characteristics of orogenic gold deposits. The Manondo-Choma gold prospect formed in a typical orogenic setting and is located in ductile shear zones and faults, which is similar to the orogenic-type deposits. We conclude that the Manondo-Choma gold deposit is an orogenic-type gold occurrence which has experienced subsequent deformation.

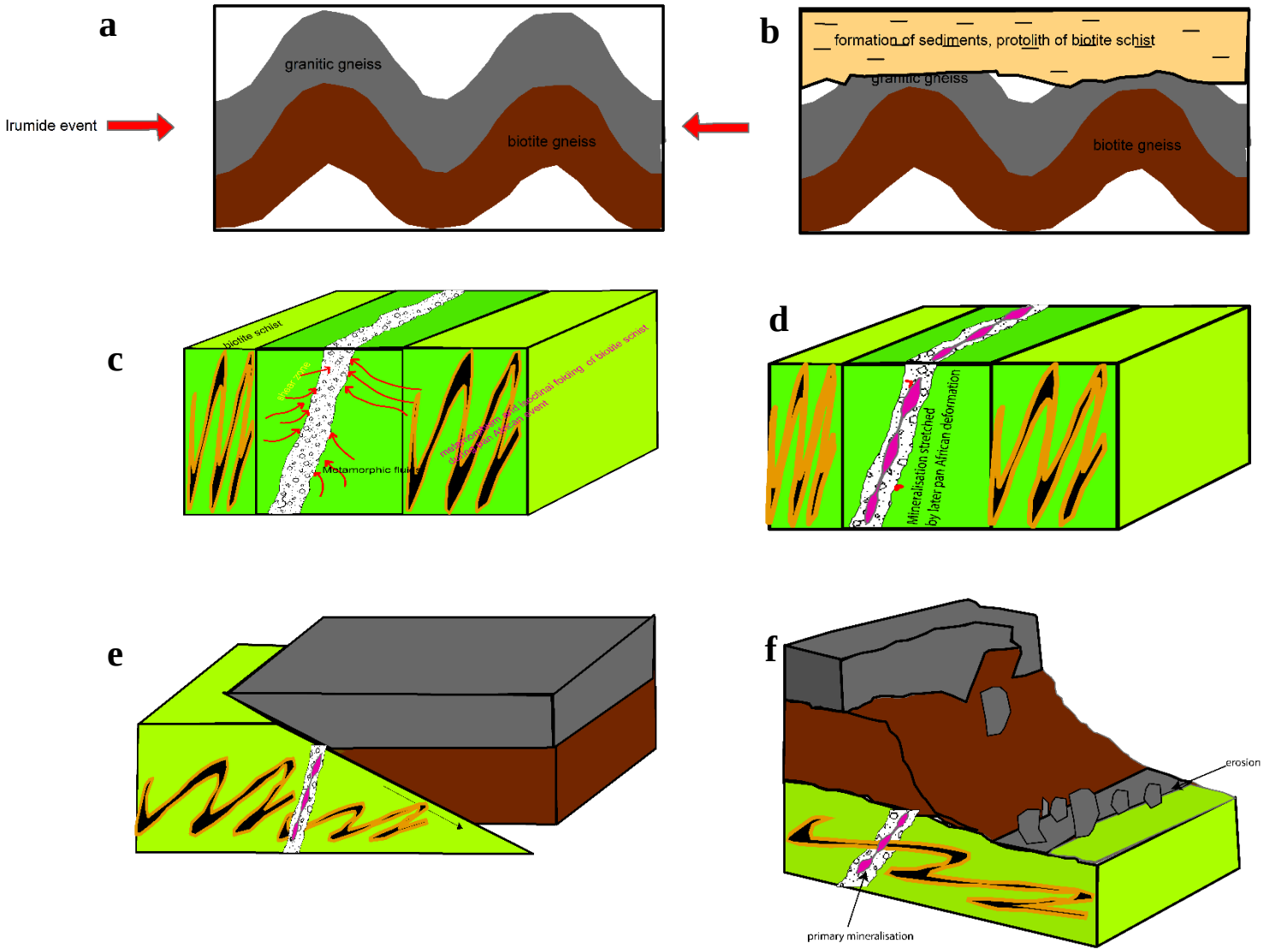

Figure 1: *Genetic model for the Manondo-Choma gold prospect (a) deformation of granite gneiss and biotite gneiss at Irumide time. (b) erosion of granitic gneiss and formation of basin with pelagic sediments prior to Pan African deformation. (c) devolatilization and orogenic gold mineralisation forming in these pelagic sediment layers as they metamorphose to greenshcist facies at early Pan African, (d) orogenic gold being transposed as metamorphism reaches amphibolite facies during later pan African deformation, (e) granite gneiss and biotite gneiss thrusting over the biotite schist, (f) erosion through the thrust sheet liberate the transposed gold into placer concentration.*

5.3. Outstanding gaps and further work

5.3.1. Further work at Manondo Choma

This study relied on a limited number of core intersections, detailed drilling in the area will be required to better constrain the extent of mineralisation and to more clearly understand the structures that contain the gold.

Further work to investigate the linkage between Carbonititic magma and gold mineralisation at Manondo-Choma area: There is a nearby carbonatitic intrusion near the study area, Kangankunde carbonatite intrusion. This study did not tackle if this intrusion acted as a heat source or had any influence on gold mineralisation. We therefore recommend that more studies should be done to determine if this intrusion has any relationship with gold mineralisation in the area.

Fluid inclusion study using LA-ICPMS technique: Although it was interpreted that gold was sourced from metamorphic fluid and carried by bisulphide complex in metamorphic fluids, there was no absolute evidence to prove this theory. The ore fluids at Manondo-Choma were made up of two types of fluids (i.e., metamorphic and magmatic fluids), and LA-ICPMS analysis of trace elements and ore metals (e.g., Au, Ag, Pb, Zn, Cu, W) will directly constrain the source of metals and type of ore fluids carrying ore metals.

5.3.2. Further work in the broader Malawian context

Geological mapping: The geology of Malawi has not been mapped; it was last mapped in the 1960s this is very outdated. The regional geology in chapter 3 was largely derived from adjacent neighbouring countries geology. We recommend that Geological mapping must be done to enhance future exploration. Adequate and up to date geological information is crucial for mineral exploration. So far, the available geological data is inadequate. It is therefore recommended that updated detailed geological mapping must be done.

Further study of the other gold occurrences (Prospects) in Malawi. This study only concentrated on the Kirk Range area, we highly recommend that the other gold occurrence sites (Dwangwa, Nathenje, Makanjira) in Malawi where there are artisanal mining activities warrant further detailed studies. Detailed research in these other areas could delineate the other mineralised structures and will improve understanding of the ore deposit setting in Malawi.

Reference

Goldfarb, J., Snee, L.W, & Pickthorn, J. (1993). Orogenesis, high -T- thermal events, and gold vein formation within metamorphic rocks of the Alaskan cordillera. *mineralogic magazine*.

Appendix 1

Table A1 Garnet mineral chemistry

	Gr Gneiss core	Gr Gneiss (rim)	B gneiss core	B gneiss (rim	B schist core	B schist (rim)
SiO2	38.52	37.57	38.48	38.53	38.47	37.92
TiO2	0	0.00	0.00	0.00	0.00	0.00
Al2O3	21.89	21.12	20.57	21.27	20.68	21.07
Cr2O3	0	0.00	0.00	0.00	0.00	0.00
FeO	30.91	26.73	24.47	25.81	24.72	25.50
MnO	0.45	1.44	0.86	1.75	0.76	1.94
MgO	7.63	1.84	1.96	1.68	1.96	1.60
CaO	10.72	11.48	14.04	12.05	13.81	12.45
Na2O	0.04	0.00	0.00	0.00	0.00	0.00
K2O	0	0.00	0.00	0.00	0.00	0.00
TOTAL	100.56	100.18	100.37	101.09	100.40	100.47
oxygen	12.00	12.00	12.00	12.00	12.00	12.00
Si	2.99	2.98	3.02	3.02	3.02	3.00
Al(vi)	2.00	1.98	1.90	1.96	1.91	1.96
Fe(iii)	0.00	0.00	0.00	0.00	0.00	0.00
Ti	0.00	0.00	0.00	0.00	0.00	0.00
Cr	0.00	0.000	0.00	0.001	0.00	0.002
Fe(ii)	2.01	1.78	1.56	1.69	1.58	1.69
Mn	0.03	0.10	0.06	0.12	0.05	0.13
Mg	0.88	0.22	0.23	0.20	0.23	0.19
Ca	0.06	0.98	1.18	1.01	1.16	1.05
Na	0.00	0.00	0.00	0.00	0.00	0.00
K	0.00	0.00	0.00	0.00	0.00	0.00
Mg/(Fe+Mg)	0.31	0.11	0.13	0.10	0.13	0.10
Alm (mol. %)	67.36	57.90	51.45	56.74	52.28	55.12
Prp (mol. %)	29.64	7.09	7.58	7.28	7.59	6.16
Grs (mol. %)	2.01	31.85	39.09	32.73	38.47	34.47
Sps (mol. %)	0.99	3.15	1.88	3.24	1.67	4.24

Representative electron microprobe analyses of garnet (O=12)

Table A2 Biotite mineral chemistry

	Gr Gneiss core	Gr Gneiss rim	B gneiss core	B gneiss rim	B schist core	B schist rim
SiO2	35.73	36.59	36.32	35.79	36.34	35.46
TiO2	3.35	3.27	3.27	3.52	3.04	3.02
Al2O3	15.82	16.53	16.23	15.62	15.80	15.57
Cr2O3	0.00	0.00	0.00	0.00	0.00	0.00
FeO	21.57	20.48	20.51	21.16	21.40	21.70
MnO	0.52	0.28	0.36	0.40	0.28	0.35
MgO	8.66	9.23	8.93	8.81	8.80	8.81
CaO	0.00	0.00	0.00	0.00	0.00	0.00
Na2O	0.17	0.00	0.00	0.17	0.00	0.21
K2O	9.82	9.73	9.84	9.75	9.93	9.66
TOTAL	95.64	96.11	95.45	95.23	95.60	94.78
oxygen	22.00	22.00	22.00	22.00	22.00	22.00
Si	5.26	5.31	5.32	5.29	5.34	5.26
Al(iv)	2.74	2.69	2.68	2.71	2.66	2.72
Al(vi)	0.01	0.13	0.13	0.01	0.07	0.00
Fe(iii)	2.10	2.05	1.99	2.04	2.06	2.20
Ti	0.37	0.36	0.36	0.39	0.34	0.34
Cr	0.00	0.00	0.00	0.00	0.00	0.00
Fe(ii)	0.56	0.43	0.53	0.57	0.57	0.49
Mn	0.06	0.03	0.04	0.05	0.04	0.04
Mg	1.90	2.00	1.95	1.94	1.93	1.95
Ca	0.00	0.00	0.00	0.00	0.00	0.00
Na	0.05	0.00	0.00	0.05	0.00	0.06
K	1.84	1.80	1.84	1.84	1.86	1.83
Mg/(Fe+Mg)	0.48	0.49	0.50	0.77	0.77	0.80

Table A 3 CPX-OPX mineral chemistry

Lithology	**Gr Gneiss**	**B gneiss**	**B gneiss**
	CPX	CPX	OPX
SiO2	52.52	49.18	50.71
TiO2	0.18	0.42	0.07
Al2O3	1.58	4.98	1.23
Cr2O3	0	0.00	0.02
FeO	10.15	11.68	29.43
MnO	0.11	0.26	1.94
MgO	12.83	11.55	16.28
CaO	21.85	20.68	0.71
Na2O	0.35	0.9	0.04
K2O	0	0	0
TOTAL	99.57	99.65	100.43
oxygen	6	6	6
Si	0.294	1.847	1.958
Al(iv)	0.010	0.220	0.056
Al(vi)	0.010	0.220	0.056
Fe(iii)	3.404	0.126	0.026
Ti	0.001	0.012	0.002
Cr	0.000	0.000	0.001
Fe(ii)	0.012	0.241	0.924
Mn	0.037	0.008	0.063
Mg	0.107	0.647	0.937
Ca	0.131	0.832	0.029
Na	0.004	0.066	0.003
K	0.000	0.000	0.000
Mg/(Fe+Mg)	0.031	0.362	0.504
XWo = Ca/Ca+Mg+FeT	45.880	45.086	1.532
XEn = Mg/Ca+Mg+FeT	37.484	35.037	48.889
XFs = FeT/Ca+Mg+FeT	16.636	19.876	49.579

Table A 4 Feldspar mineral chemistry

Mineral Name	Plagioclase				K-feldspar			
	Gr gneiss Matrix	Gr gneiss In Grt	B gneiss Lamella	B schist Matrix	Gr gneiss Matrix	Gr gneiss In Grt	B gneiss Host	B schist Matrix
SiO2	60.84	60.84	60.98	60.96	65.60	65.14	63.68	64.19
Al2O3	24.70	24.71	24.19	24.23	18.38	18.53	18.81	18.66
TiO2	0.00	0.00	0.00	0.00	0.00	0.00	0.00	0.00
Cr2O3	0.00	0.00	0.00	0.00	0.00	0.00	0.00	0.00
FeO	0.14	0.00	0.00	0.00	0.00	0.00	0.17	0.00
MnO	0.00	0.00	0.00	0.00	0.00	0.00	0.00	0.00
MgO	0.00	0.00	0.00	0.00	0.00	0.00	0.00	0.00
CaO	6.12	6.25	6.00	5.92	0.00	0.00	0.20	0.00
Na2O	8.20	8.26	8.34	8.39	0.68	0.59	0.80	0.89
K2O	0.14	0.26	0.24	0.18	15.78	16.02	15.05	14.97
Total	100.14	100.32	99.74	99.67	100.44	100.29	98.70	98.72
Si	2.70	2.69	2.72	2.72	3.01	3.00	2.97	2.99
Al	1.29	1.29	1.27	1.27	0.99	1.01	1.03	1.02
Ti	0.00	0.00	0.00	0.00	0.00	0.00	0.00	0.00
Cr	0.00	0.00	0.00	0.00	0.00	0.00	0.00	0.00
Fe	0.00	0.00	0.00	0.00	0.00	0.00	0.01	0.00
Mn	0.00	0.00	0.00	0.00	0.00	0.00	0.00	0.00
Mg	0.00	0.00	0.00	0.00	0.00	0.00	0.000	0.00
Ca	0.29	6.25	0.29	0.28	0.00	0.00	0.000	0.00
Na	0.71	8.26	0.72	0.73	0.06	0.05	0.07	0.08
K	0.01	0.26	0.01	0.01	0.92	0.94	0.90	0.89
Total	4.99	18.75	5.01	5.01	4.99	5.00	4.98	4.98
An (mol.%)	28.97	29.07	28.08	27.77	0.00	0.00	1.02	0.00
Ab (mol.%)	70.24	69.48	70.61	71.21	6.15	5.34	7.38	8.32
Kfs (mol.%)	0.79	1.45	1.31	1.02	93.85	94.66	91.59	91.68

Table A5 Amphibole mineral chemistry

	Gr Gneiss core	Gr Gneiss (rim)	B gneiss core	B gneiss (rim
SiO2	43.91	42.40	44.08	43.54
TiO2	1.07	1.02	0.97	1.07
Al2O3	13.16	13.40	12.22	12.98
Cr2O3	0.00	0.00	0.00	0.00
FeO	16.18	15.91	15.77	15.77
MnO	0.24	0.17	0.25	0.35
MgO	9.70	9.26	10.16	9.83
CaO	11.69	11.34	11.62	11.53
Na2O	1.43	1.18	1.16	1.37
K2O	0.55	0.57	0.42	0.57
TOTAL	97.93	95.25	96.66	97.01
oxygen	23.00	23.00	23.00	23.00
Si	6.46	6.39	6.53	6.45
Al(vi)	0.74	0.77	0.66	0.71
Fe(iii)	0.38	0.48	0.49	0.44
Ti	0.12	0.12	0.11	0.12
Cr	0.00	0.000	0.00	0.00
Fe(ii)	1.61	1.52	1.46	1.51
Mn	0.03	0.02	0.03	0.04
Mg	2.13	2.08	2.24	2.17
Ca	1.84	1.83	1.84	1.83
Na	0.41	0.35	0.33	0.39
K	0.10	0.11	0.08	0.11
Mg/(Fe+Mg)	0.57	0.58	0.61	0.59

Appendix 2

Lithological units that were sampled for PT estimates and geochronology. All lithologies contain garnets an indication that they have been subjected to high pressure conditions. (a) biotite gneiss (Chis 62), (b) granitic gneiss (Chis 69) and (c) biotite schist (chis 52).

Appendix 3

Quartz veins samples that were used for fluid inclusion and stable isotope

Appendix 4

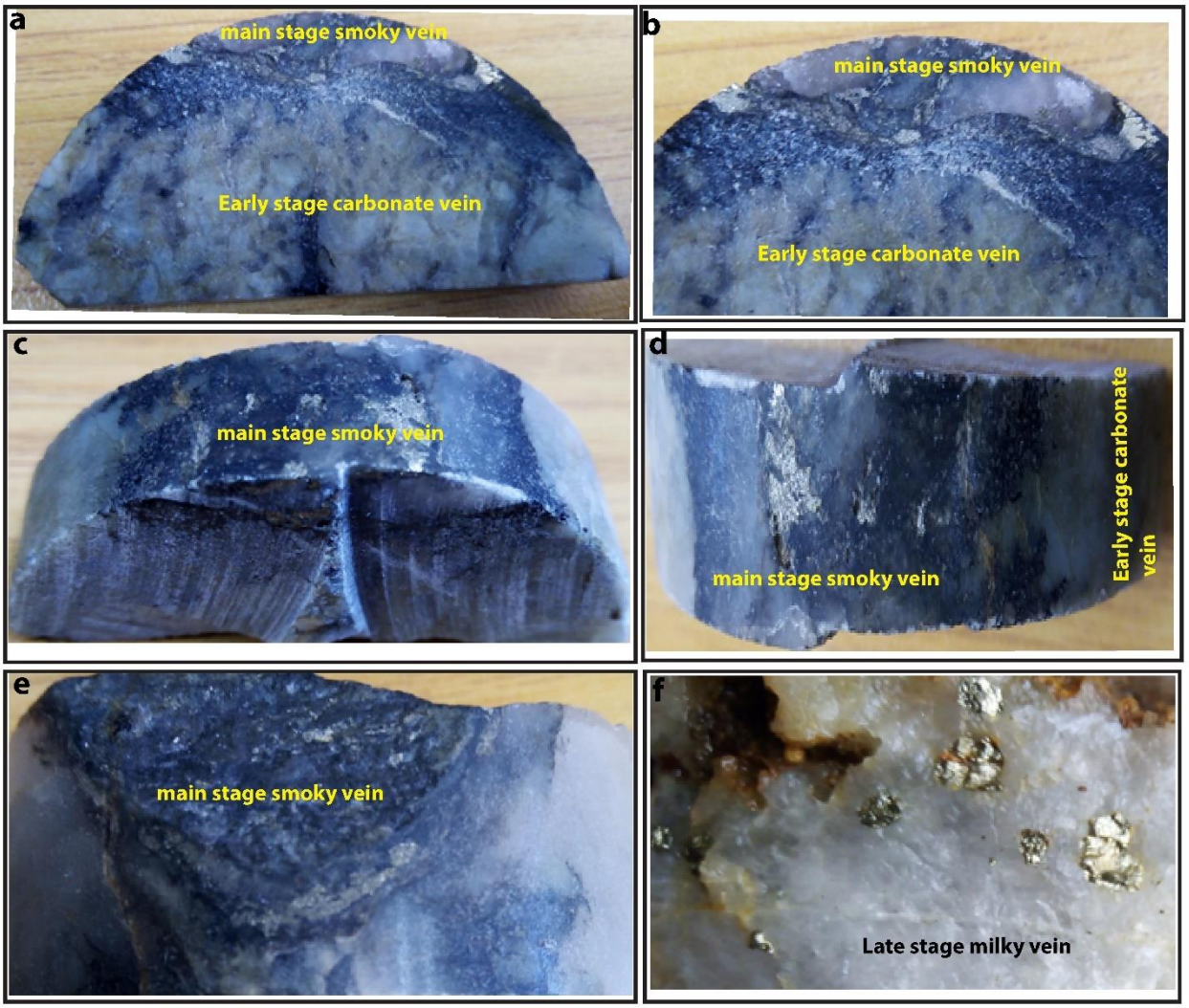

Quartz veins indicating stages of mineralisation based on cross cutting relationship. Milky veins were the first veining stage and was later crosscut by smoky mineralised veins in the main stage of mineralisation.